Numerical analysis of carotid artery flow

NUMERICAL ANALYSIS OF CAROTID ARTERY FLOW

F.N. VAN DE VOSSE

NUMERICAL ANALYSIS OF CAROTID ARTERY FLOW

Het verschijnen van dit proefschrift werd mede mogelijk gemaakt door de steun van de Nederlandse Hartstichting.

Financial support by the Netherlands Heart Foundation for publication of this thesis is gratefully acknowledged.

NUMERICAL ANALYSIS OF CAROTID ARTERY FLOW

PROEFSCHRIFT

TER VERKRIJGING VAN DE GRAAD VAN DOCTOR AAN DE TECHNISCHE UNIVERSITEIT EINDHOVEN, OP GEZAG VAN DE RECTOR MAGNIFICUS, PROF.DR. F.N. HOOGE, VOOR EEN COMMISSIE AANGEWEZEN DOOR HET COLLEGE VAN DEKANEN IN HET OPENBAAR TE VERDEDIGEN OP VRIJDAG 27 FEBRUARI 1987 TE 16.00 UUR

DOOR

FRANCISCUS NICOLAAS VAN DE VOSSE

GEBOREN TE MAASTRICHT

Druk: Dissertatiedrukkerij Wibro, Helmond.

Dit proefschrift is goedgekeurd door de promotoren:

Prof.dr.ir. J.D. Janssen
en
Prof.dr.ir. P. Wesseling

Co-promotor:
Dr.ir. A.A. van Steenhoven.

voor: Claire, Anouk, Thomas en mijn ouders.

CONTENTS

Abstract.

In addition to in-vivo and in-vitro experiments, numerical analyses of blood flow patterns in the carotid artery (bifurcation) play an important role in studies on both the detectability and the genesis of atherosclerotic disease. To obtain more insight into these flow patterns, numerical analyses, limited to Newtonian incompressible flows in rigid-wall geometries, have been carried out. First, a Galerkin finite element approximation of the unsteady Navier-Stokes equations is formulated and tested for a two-dimensional oscillating flow problem between two flat plates and the vortex shedding phenomenon downstream a circular cylinder. Next, the steady and unsteady (physiological) flow over a square step in a two-dimensional channel has been analysed with special emphasis on the optimization of the calculation procedure. In this two-dimensional stenosis model, the formation and shape of the reversed flow regions downstream the step are used to characterize the flow. After that, the unsteady flow in two-dimensional carotid bifurcation models for both normal and stenosed geometries has been analysed with special attention to the distribution of the reversed flow regions and wall shear stresses. For both the square-step stenosis model and the bifurcation model the calculated velocity distribution has been validated by laser-Doppler measurements in experimental models. Finally, as a first step to a three-dimensional analysis of the flow in the carotid bifurcation, the steady flow development of the primary and secondary velocity fields in a curved tube has been analysed numerically and compared with experiments.

In conclusion the numerical analyses appear to give accurate and detailed descriptions of the flow field in simplified models of the carotid artery bifurcation. For a complete three-dimensional analysis, however, improved computer capacity and more efficient solution procedures are needed.

List of symbols.

conventions :

A	matrix
A_{ij}	element of matrix A
$\underline{\underline{a}}$	tensor
a_{ij}	components of tensor $\underline{\underline{a}}$
$H^1(\Omega)$	Sobolev space : $\{v \mid v \in L^2(\Omega), \frac{\partial v}{\partial x_i} \in L^2(\Omega), i=1,\ldots\}$
$L^2(\Omega)$	Hilbert space : $\{v \mid \int v^2 d\Omega < \infty\}$
$(a,b)_V$	inner product of a and b in space V
$\|\|v\|\|_V$	norm of v in space V
$\|\alpha\|$	absolute value of scalar α
V^h	finite dimensional subspace of V
$\underline{v}$	column matrix usually a composition $[\underline{v}_1^T, \underline{v}_2^T, \ldots]$
$\vec{v}$	vector
v_i	the i-th component of a vector $\vec{v}$ or a column matrix $\underline{v}$
$(\vec{a} \cdot \vec{b})$	inner product of vectors $\vec{a}$ and $\vec{b}$
Γ	boundary of space Ω
Ω	space in $\mathbb{R}^n$

symbols :

D	diameter common carotid artery, charcteristic length measure
$J(\underline{u})$	Jacobian of $N(\underline{u})\underline{u}$
L	divergence matrix
M	mass matrix
M_p	projection matrix in penalty formulation
$N(\underline{u})$	convection matrix
Q	flow
Q_o	temporal mean flow
R	curvature radius of curved tube
Re	Reynolds number $U_o D/\nu$
Re_h	Reynolds number based on the step height $(U_o h/\nu)$
S	diffusion matrix
St	Strouhal number fD/U_o

T	periodic time
U_o	temporal and cross-sectional mean of the velocity, characteristic velocity measure
W	cross-sectional mean of the axial velocity in curved tube
a	internal radius of curved tube
$\underline{b}$	column matrix containing boundary stress values
c	amplification factor
f	frequency
$\vec{f}$	body force vector
$\underline{f}$	column matrix containing the body force parameters
$\underline{g}^n$	$\underline{g}(t=t^n)$
$\underline{g}^\theta$	$\theta\underline{g}^{n+1} + (1-\theta)\underline{g}^n$
h	1 : step height 2 : discretisation parameter (characteristec dimension of a finite element
$\vec{n}$	outer normal vector on boundary Γ
$\vec{t}$	tangential vector on boundary Γ
p	pressure
$\underline{p}$	column matrix containing the prssure parameters
p^h	approximated pressure
p_o	characteristic pressure ϱU_o^2
p_x	x-derivative of p
q	test function for the continuity equation
t	time
$\vec{u}$	velocity vector in IR^n
$\vec{u}^h$	approximated velocity
$\underline{u}$	column matrix containing the velocity parameters
$\dot{\underline{u}}$	time derivative of $\underline{u}$
$\vec{v}$	test function for the momentum equation
$\vec{x}$	position vector in IR^n
$\vec{x}_c$	position vector of centroid of an element
Δp_x	error in p_x
Δt	timestep
Δu	error in u
θ	curvature angle of curved tube
α	frequency parameter $R\sqrt{(\omega/\nu)}$
δ	curvature ratio (a/R)
δ_{ij}	Cronecker delta

ε	penalty parameter
η	dynamic viscosity
θ	parameter in θ-method time integration
κ	Dean number Re/δ
λ_i	1 : barycentric coordinate
	2 : eigenvalue
ν	kinematic viscosity
ν_m	iteration step in Newton iteration
ξ_c	mean axial vorticity
ξ_c'	$(\xi_c a/W)\delta^{3/2}$
ϱ	density
$\underline{\underline{\sigma}}$	Cauchy stress tensor
σ_n	normal stress
σ_t	tangential stress
τ	characteristic time (D/U_o)
τ_o	characteristic wall shear stress $(6\nu U_o/D)$
τ_w	wall shear stress
φ_{in}	basis functions for the i-th velocity component
ψ_m	basis functions for the pressure
ω	angualar frequency $2\pi f$

CHAPTER 1: GENERAL INTRODUCTION.

1.1. Carotid artery flow and atherosclerosis.

Atherosclerosis is an arterial disease resulting in localized stiffening and thickening of the arterial wall, associated with among other things, smooth-muscle cell proliferation and lipid (cholesterol) deposition. Atherosclerotic lesions may lead to narrowing (stenoses) or even occlusion of the artery affected. A survey dealing with the pathogenesis and manifestations of this disease has been reported by Ross and Glomset (1976). The frequency distribution of the occurrence of atherosclerotic lesions is not uniform, but especially arterial bifurcations and bends are found to be sites of preference (Noon, 1977 and Nerem and Cornhill, 1980). Besides coronary, femoral and iliac artery bifurcations, the carotid artery bifurcation too, is often involved in the atherosclerotic process, and forms a major cause of cerebral vascular disease.

Besides biochemical and cytological aspects, hemodynamical aspects play an important role in the genesis of atherosclerosis (Caro and Nerem, 1973, Caro, 1977, Roach, 1977, Young, 1979 and Nerem and Cornhill, 1980). Different hypotheses have been proposed to relate hemodynamical forces to the location of atherosclerotic lesions (Fry, 1976 and Caro et al., 1969, 1971 and 1973). In both hypotheses the arterial wall shear stress plays an important role. According to Fry, early atherosclerotic lesions are to be expected in regions with high wall shear stresses, which were found to induce an increasing endothelial surface permeability. According to Caro and co-workers early lesions can develop in regions with low wall shear stresses due to the shear dependent mass transport mechanism for atherogenesis. Without taking a stand in these apparently conflicting hypotheses, it is clear that local wall shear stress distributions, and thus local velocity distributions, are of importance. Also in the hypothesis for atherogenesis, based on oscillatory shear stress and increased partial residence times, reported by Ku (1983), local velocity and shear stress distributions are of importance. Moreover,

the recent developments in non-invasive ultrasonic techniques to measure local instantaneous blood flow velocities in-vivo (Peronneau, 1977, Greene and Histand, 1979 , Hoeks et al., 1981 and Van Merode, 1986) offer the possibility to detect reliably atherosclerosis at an early stage of the disease, and to relate atherogenesis to the local flow patterns in arteries in man. Since no detailed information about these patterns can be obtained with ultrasound techniques, presently available, important information has to be determined from model studies. To obtain better insight into the local flow patterns, the numerical analysis of carotid artery flow in models and its experimental validation are dealt with in the present thesis.

1.2. Hemodynamical and geometrical properties and restrictions of the models employed.

Several general characteristics, including rheological properties of blood, distensibility and geometry of the arterial wall and the unsteady pulsatile properties of the flow, play an important role in the modelling of the carotid artery flow.

Blood is a suspension of particles (blood cells, platelets etc.) in a fluid called plasma and exhibits a non-Newtonian behaviour at low shear rates. At higher shear rates, as generally found in the carotid artery, blood is assumed to behave like an incompressible Newtonian fluid with a density slightly higher than water and a kinematic viscosity in the range from 3 to 4.5 10^{-6} m^2/s (Young, 1979 and Pedley, 1980). Also in the models presented here, Newtonian fluid behaviour is assumed, although the validity of this assumption is debatable especially for flow regions with low shear rates.

The arterial wall is anisotropic and viscoelastic (Roach, 1977). Incorporation of these properties in numerical flow models is rather complex and thought to be only meaningful if the modelling in rigid three-dimensional geometries can be proved to be valid. So, the arterial walls in the models employed in the present study are assumed to be rigid.

The geometry of the human carotid artery bifurcation shows a rather large interindividual variation. The geometries used in this study are based upon geometry parameters given by Bharadvaj et al.

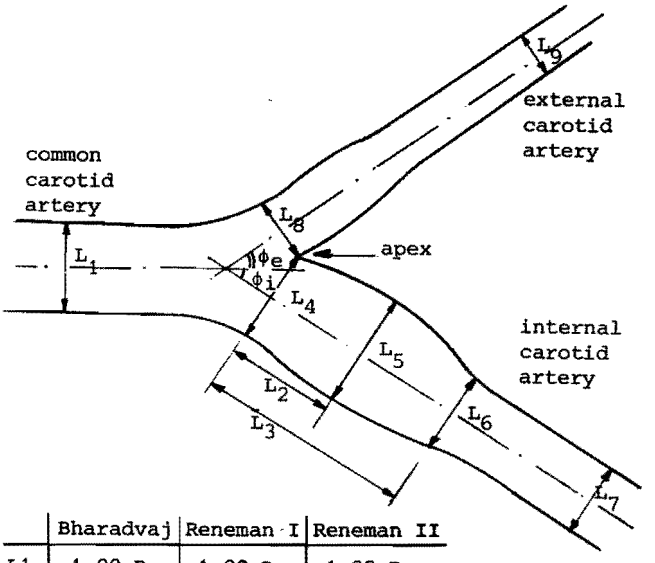

	Bharadvaj	Reneman I	Reneman II
L1	1.00 D	1.00 D	1.00 D
L2	0.91 D	-	-
L3	2.14 D	-	-
L4	1.04 D	1.00 D	1.08 D
L5	1.11 D	1.03 D	1.11 D
L6	0.72 D	-	-
L7	0.69 D	0.87 D	0.97 D
L8	0.69 D	-	-
L9	0.58 D	-	-
φi	25.4°	10.8°	12.6°
φe	25.1°	-	-

Fig. 1.1 : Typical geometry of the human carotid artery bifurcation (Bharadvaj et al., 1982).
Table 1.1 : Geometry parameters as given by Bharadvaj et al. (1982) and Reneman et al. (1985).

(1982), Ku (1983) and Reneman et al. (1985). Bharadvaj and co-workers obtained their geometry parameters by means of a large number of angiograms of both healthy (with respect to carotid vascular disease) and diseased subjects, and derived a 'mean' geometry as given in Fig. 1.1 . Reneman et al. reported less detailed geometry parameters (Table 1.1), but obtained information from two groups (11 younger and 9 older) healthy volunteers by means of a multigate, pulsed Doppler system coupled to a B mode imager.

The carotid artery bifurcation consists of a main branch, the common carotid artery, which divides into two branches, the internal carotid artery, responsible for the blood supply of the brain, and the external carotid artery, responsible for the facial blood supply. The tip of the flow divider is often referred to as the apex. The internal carotid artery is characterized by a widening known as the internal carotid sinus (or bulb). The geometry parameters are based on a two-dimensional projection of a three-dimensional body, so the assumption is made that the branches lie in one plane of symmetry (in the remainder indicated as the plane of the bifurcation). Furthermore, it is assumed that the cross-sections of the branches are circular with a smooth intermediate shape.

The flow in the carotid artery bifurcation is pulsatile with an instantaneous flow rate varying during the cardiac cycle. In this study, the flow rate curve in the common carotid artery as described by Ku (1983) is used (Fig. 1.2). The flow rate consists of a systolic phase, in which the flow accelerates to a rate of about 2.5 times its mean value, followed by a deceleration after which two small flow pulses occur and gradually a steady flow develops towards the end of the diastolic phase. The flow is characterized by two dimensionless parameters:

the Reynolds number $\quad Re = DU_0/\nu \qquad (1.1)$

and the frequency parameter $\quad \alpha = R\sqrt{(\omega/\nu)} \qquad (1.2)$

(D being the diameter of the common carotid artery, U_0 the cross-sectional and temporal mean of the velocity in the common carotid artery, ν the kinematic viscosity, R=D/2 the radius of the common carotid artery and ω the angular frequency of the pulsating flow). An alternative for the frequency parameter is the Strouhal number $St=\omega D/2\pi U_0 (=2\alpha^2/\pi Re)$. The average diameter (D) of the common carotid artery amounts to about 6.2 mm (Ku, 1983 and Reneman et al., 1985) whereas the mean flow (Q_0) is found to be about 4.5 ml/s (Ku, 1983). This yields a mean velocity $U_0=4Q_0/\pi D^2 \approx 0.145$ m/s. Using the flow rate curve as given in Fig. 1.2 and assuming a kinematic viscosity of $3.5\ 10^{-6}\ m^2/s$, the mean Reynolds number amounts about to 250 and varies from about 175 to 650, so laminar flow can be assumed (cf.

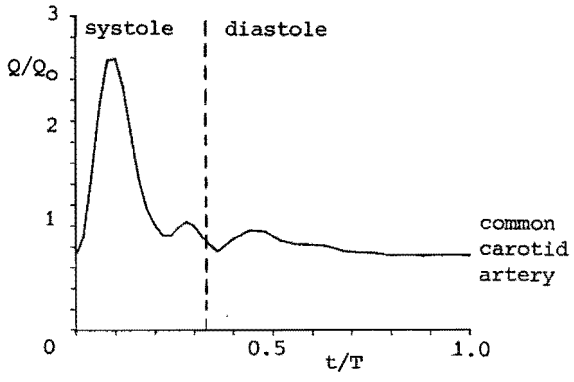

Fig. 1.2 : Flow rate in the common carotid artery as a function of time during one cardiac cycle (Ku, 1983).

Young, 1979). If furthermore a cardiac cycle time of 1s is assumed, the frequency parameter α is about 4. Finally, the flow in the common carotid artery is assumed to be fully developed at a few diameters upstream of the flow divider.

1.3. Numerical approximation of laminar incompressible Newtonian flow.

As depicted in the previous section, in first approximation the carotid artery flow is regarded as an incompressible Newtonian unsteady laminar flow. This kind of flow is mathematically described by the Navier-Stokes equations. Only for simple geometries and simple boundary conditions analytical solutions of these equations exist (Schlichting, 1979). For complex geometries like the carotid artery bifurcation, numerical approximations have to be applied. The most important numerical methods available from literature are, firstly, the finite difference (Roache, 1972 and Peyret and Taylor, 1982) and the closely related finite volume (Patankar, 1980 and Spalding, 1981) methods and secondly, finite element methods (Girault and Raviart, 1979, Thomasset, 1981 and Cuvelier et al., 1986). Until a decade ago,

finite difference and finite volume methods were most commonly applied. Besides their mathematical simplicity, an important advantage of these methods is the favourable structure of the resulting set of equations (often tri-diagonal) enabling efficient numerical solution procedures. Significant difficulties are encountered, however, in the modelling of complex geometries and the application of local grid refinements. The use of body-fitted co-ordinate systems offers some possibilities with respect to the modelling of complex geometries (Gunton et al., 1983), but the great difficulty of application of local grid refinements, required especially for an accurate approximation of the flow in regions with large velocity gradients, make these methods inattractive for the present application. Although the structure of the resulting set of equations is less favourable, but still sparse, requiring more computing time and memory capacity, the finite element method enables the modelling of complex geometries and easily incorparates local grid refinements. Moreover, the finite element model can be extended with models of wall distensibility because of its applicability to structural mechanical problems. Nevertheless, until now, finite element formulations of unsteady flow in three-dimensional geometries are still in progress. In this dissertation the finite element method is used and part of its progress and application to carotid artery flow will be dealt with.

1.4. Methodology employed.

The study presented here has been performed in several more or less distinguishable stages coinciding with the development of the numerical method, but also coinciding with some distinct flow properties occurring in the carotid artery bifurcation.

Initially, in chapter 2, the finite element solution procedure for steady and unsteady two-dimensional flow has been studied. In section 2.2 the spatial discretisation of the equations using a standard Galerkin finite element method is dealt with. After the derivation of a penalty function formulation of the equations, a short description of the finite element, as available in the finite element code used (Segal and Praagman, 1984), is given. Some remarks on the mathematical background of the method are included in appendices 1 and 2. In the next section (section 2.3), a finite difference

time integration method is presented and analysed with respect to its accuracy and stability. Then the theoretical observations made are confirmed by numerical experiments with calculations of oscillating flow between two parallel plates and the Von Karman vortex shedding past a circular cylinder.

In chapter 3, the numerical method described is applied to steady (section 3.2) and unsteady (section 3.3) flow over a square step. This flow configuration can be considered a two-dimensional stenosis model (sections 3.3.1 and 3.3.2), but is mainly used to analyse the numerical method with respect to its practical application and the influence of different kinds of boundary conditions and mesh distributions (section 3.2). Moreover, laser-Doppler measurements of both steady (section 3.2.3) and unsteady (section 3.3.4) flows over a square step have been performed and compared with the numerical results.

The analysis of pulsatile flow in two-dimensional carotid artery bifurcation models is described in chapter 4. In section 4.2, the flow in a two-dimensional geometry and an imposed flow rate as given above is described by means of its velocity and wall shear stress distribution. In section 4.3, the numerical results are compared with both two- and three-dimensional measurements and data obtained from literature. In this comparison special emphasis is given to the relevance of two-dimensional modelling of three-dimensional carotid artery flow. Furthermore, in section 4.4, the influence of a small stenosis in the internal carotid sinus on the velocity and wall shear stress distribution is analysed.

Until now calculations of fully three-dimensional carotid artery flow are strongly limited with respect to computing time and memory, unless more sophisticated (super-)computers are used. As a first step to this kind of calculations, three-dimensional steady entrance flow in a curved tube, exhibiting properties that resemble the flow in the internal carotid artery (Olson, 1971, Brech and Bellhouse, 1973 and LoGerfo, 1981), is analysed (chapter 5). Again, the results of the numerical model are validated by means of comparison with laser-Doppler measurements in an experimental model.

Final conclusions and a remark on possible progress in this study are given in chapter 6.

references.

- Bharadvaj B.K., Mabon R.F. and Giddens D.P.,'Steady flow in a model of the human carotid bifurcation. Part I: Flow visualization.', J. Biomech., 15, p 349-362 (1982).
- Bharadvaj B.K., Mabon R.F. and Giddens D.P.,'Steady flow in a model of the human carotid bifurcation. Part II: Laser-Doppler anemometer measurements.', J. Biomech., 15, p 363-378 (1982).
- Brech R. and Bellhouse B.J.,'Flow in branching vessels.', Cardiovasc. Res., 7, p 593-600 (1973).
- Caro C.G., Fitz-Gerald J.M. and Schroter R.C.,'Arterial wall shear distribution of early atheroma in man.', Nature, 223, p 1159-1161 (1969).
- Caro C.G., Fitz-Gerald J.M. and Schroter R.C.,'Atheroma and arterial wall shear. Observation, correlation and proposal of a shear dependent mass transfer mechanism for atherogenesis.', Proc. Roy. Soc. Lond. B, 177, p 109-159 (1971).
- Caro C.G. and Nerem R.M.,'Transport of C-4-cholestorol between serem and wall in the perfused dog common carotid artery.', Circ. Res., 32, p187-205 (1973)
- Caro C.G.,'Mechanical factors in atherogenesis.', In : Cardiavascular flow dynamics and measurements. ,p 473-487, Eds. Hwang N.H.C. and Normann N.A., University Park Press, Baltimore (1977).
- Cuvelier C., Segal A. and Van Steenhoven A.A.,'Finite element methods and Navier-Stokes equations.', D.Reidel Publishing comp. Dordrecht/Boston/Lancaster/Tokyo (1986).
- Fry D.L.,'Hemodynamic forces in atherogenesis.', In: Cerebrovascular Diseases, p 77-95, Ed. Scheinberg P., Raven press New York (1976).
- Girault V. and Raviart P.-A.,'Finite element approximation of the Navier-Stokes equations.', Springer-Verlag, Berlin, Heidelberg, New York (1979).
- Green E.R. and Histand M.B.,'Ultrasonic assessment of simulated atherosclerosis: in-vitro and in-vivo comparisons.', J. Biomech. Eng., 101, p 73-81 (1979).

- Gunton M.C., Malin M.R., Roston H.I., Spalding D.B. and Tatchell D.G.,'Use of body-fitted coordinate scheme in PHOENICS.', CHAM TR/97 London (1983).
- Hoeks A.P.G., Reneman R.S. and Peronneau P.A.,'A multigate pulsed Doppler system with serial data-processing.', IEEE Trans. Sonics Ultrasonics, 28, p 242-251 (1981).
- Ku D.N.,'Hemodynamics and atherogenesis at the huamn carotid bifurcation.', Ph.D. Thesis, Georgia inst.techn. (1983).
- LoGerfo F.W., Nowak M.D., Quist W.C. Crawshaw H.M. and Bharadvaj B.K.,'Flow studies in a model carotid bifurcation.', Atherosclerosis, 1, p 235-241 (1981).
- Van Merode T.,'The use of a multigate pulsed Doppler system in the evaluation of the carotid artery circulation.', Thesis, University of Limburg, The Netherlands (1986).
- Nerem R.M. and Cornhill J.F.,'The role of fluid dynamics in atherogenesis'. J. Biomech. Eng., 102, p 181-189 (1980).
- Noon G.P.,'Flow-related problems in cardiovascular surgery.', In : Cardiavascular flow dynamics and measurements. ,p 245-276, Eds. Hwang N.H.C. and Normann N.A., University Park Press, Baltimore (1977).
- Olson D.E.,'Fluid mechanics relevant to respiration: flow within curved tubes and bifurcation systems.', Ph.D. Thesis University of London (1971).
- Patankar S.V.,'Numerical heat transfer and fluid flow.', Hemisphere (1980).
- Pedley T.J.,'The fluid mechanics of large blood vessels.', Cambridge University Press (1980).
- Peronneau P.,'Flow velocity measurements in blood vessels by ultrasonic Doppler techniques.', In : Cardiovascular and pulmonary dynamics, p 105-120, Ed. Jaffrin J.F., INSERM, Paris (1977).
- Peyret R. and Taylor T.D.,'Computational methods for fluid flow.' Springer-Verlag, New York (1982).
- Reneman R.S., van Merode T., Hick P. and Hoeks A.P.G.,'Flow velocity patterns in and distensibility of the carotid artery bulb in subjects of various ages.', Circulation, 71, p 500-509 (1985).
- Roach M.R.,'Biophysical analyses of blood vessel walls and blood flow.', Ann. Rev. Physiol., 39, p 51-71 (1977).

- Roache P.J.,'Computational fluid dynamics.', Hermosa publishers Albuquerque (1972).
- Ross R. and Glomset J.A.,'The pathogenesis of atherosclerosis'. New England J. Medicin, 295, p 369-377 (1976).
- Sclichting H.,'Boundary layer theory.', 7nd ed McGraw-Hill (1979).
- Segal A. and Praagman N.,'SEPRAN user manual and programmers guide.', Ingenieurs bureau SEPRA, Leidschendam (1984).
- Spalding D.B.,'A general-purpose computer program for multi-dimensional one- and two-phase flow.', Math. Comp. Simulation, 23, p 267-276 (1981).
- Thomasset F.,'Implementation of finite element methods for Navier-Stokes equations.', Springer-Verlag, New york, Heidelberg, Berlin (1981).
- Young D.F.,'Fluid mechanics of arterial stenoses.', J. Biomech. Eng., 101, p 157-175 (1979).

CHAPTER 2: FINITE ELEMENT FORMULATION OF THE TWO-DIMENSIONAL STEADY AND UNSTEADY NAVIER-STOKES EQUATIONS.

2.1. Introduction.

In this chapter the finite element formulation, as used for the calculations of the 2-dimensional steady and unsteady Navier-Stokes equations, is evaluated and the results of some numerical tests are discussed.

In section 2.2 the spatial discretization of the unsteady Navier-Stokes equations is dealt with. After the statement of the governing equations, the spatial discretization of the equations using a standard Galerkin method is evaluated, yielding a set of non-linear ordinary differential equations. A discussion about the existence and uniqueness of the solution of the continuous and the discretized equations is given in appendix 1 and is mainly adopted from the studies of Temam (1977), Girault and Raviart (1979) and Raviart (1984). A common way to obtain a set of equations which is easier to solve, is to introduce a penalized formulation of the continuity equation (Bercovier, 1978, Hughes et al., 1979, Engelman et al., 1982, Oden et al., 1982, Reddy, 1982 , Carey and Krishnan, 1984 and Cuvelier et al., 1986). In this way the pressure can be eliminated from the momentum equations leading to a smaller set of equations. After the derivation of this penalized formulation (appendix 2), the finite element as used in the calculations is treated. A short description of the definition and accuracy of the extended quadratic conforming element as introduced by Crouzeix and Raviart (1973) and as available in the finite element code used (Segal and Praagman, 1984) will be given.

In section 2.3 a finite difference θ-method, incorporating both the Euler implicit and Cranck-Nicolson time integrations, is derived. The performances of the Euler implicit and Crank-Nicolson schemes are analysed and compared by means of a simple stability analysis of linear parabolic differential equations in general. Attention is also paid to the linearization of the convective terms in the momentum

equations. The undamped pressure oscillations as mentioned by Sani et al. (1981) occuring when the Crank-Nicolson time integration is used in combination with the penalty function approach, will be related to the general properties of this time integration. A slightly different formulation will be discusssed resulting in a scheme which is not hampered by these pressure oscillations.

In section 2.4 the theoretical observations as made in the two preceding sections are confirmed by numerical experiments with calculations of oscillating flow between two parallel plates and the Von Karman vortex shedding past a circular cylinder.

Finally in section 2.5 the results obtained are discussed and some concluding remarks are made.

2.2.Spatial discretization of the unsteady Navier-Stokes equations.

Governing equations.

The two-dimensional Navier-Stokes equations for incompressible Newtonian fluids are given by the momentum equations together with the continuity equation for a region Ω with boundary Γ. In cartesian co-ordinates these equations read (see for instance Batchelor, 1979):

$$\left| \begin{array}{l} \varrho \dfrac{\partial u_i}{\partial t} + \sum\limits_j \varrho u_j \dfrac{\partial u_i}{\partial x_j} = \varrho f_i + \sum\limits_j \dfrac{\partial \sigma_{ij}}{\partial x_j} \quad , \\ \\ \sum\limits_j \dfrac{\partial u_j}{\partial x_j} = 0 \end{array} \right. \qquad \begin{array}{l} i=1,2 \\ \\ j=1,2 \end{array} \qquad (2.1)$$

Here ϱ denotes the density, u_i the i-th component of the velocity and σ_{ij} the components of the Cauchy stress tensor $\underline{\underline{\sigma}}$:

$$\sigma_{ij} = -p\delta_{ij} + \eta\left(\frac{\partial u_i}{\partial x_j} + \frac{\partial u_j}{\partial x_i}\right) \quad , \qquad \begin{array}{l} i=1,2 \\ \\ j=1,2 \end{array} \qquad (2.2)$$

with p the pressure, δ_{ij} the Kronecker delta and η the dynamic viscosity. The corresponding boundary conditions which specify the

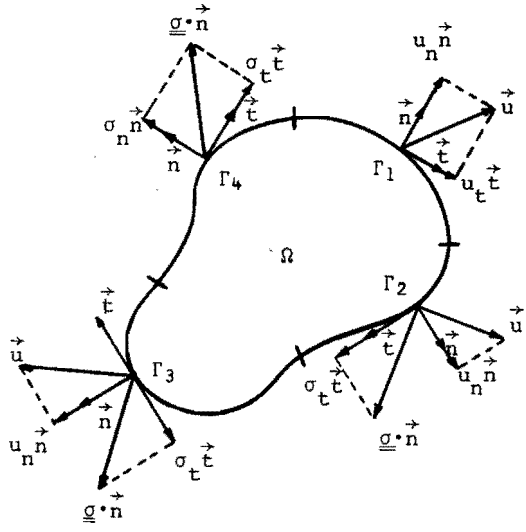

Fig. 2.1 : Region Ω with boundary Γ.

physical problem may be for example a combination of prescribed velocities and stresses in two independent directions on Γ (see Fig.2.1) :

$$
\begin{cases} \vec{u}\cdot\vec{n} = u_n \\ \vec{u}\cdot\vec{t} = u_t \end{cases} \quad \text{on } \Gamma_1
$$

$$
\begin{cases} \vec{u}\cdot\vec{n} = u_n \\ (\underline{\sigma}\cdot\vec{n})\cdot\vec{t} = \sigma_t \end{cases} \quad \text{on } \Gamma_2
$$

$$
\begin{cases} (\underline{\sigma}\cdot\vec{n})\cdot\vec{n} = \sigma_n \\ \vec{u}\cdot\vec{t} = u_t \end{cases} \quad \text{on } \Gamma_3
$$

$$
\begin{cases} (\underline{\sigma}\cdot\vec{n})\cdot\vec{n} = \sigma_n \\ (\underline{\sigma}\cdot\vec{n})\cdot\vec{t} = \sigma_t \end{cases} \quad \text{on } \Gamma_4 \qquad (2.3)
$$

With $\vec{n}$ the outer normal on Γ and $\vec{t}$ the tangential vector on Γ. Furthermore, the initial velocity in Ω must be given.

$$
u_i(t=t_0) = u_{i0} \qquad i=1,2 \qquad (2.4)
$$

For a discussion about the existence and uniqueness of the solution of these equations the reader is referred to appendix 1.

Spatial discretization.

In order to discretize (2.1) the standard Galerkin method is applied, starting from the variational problem as given in appendix 1 (A1.3). For convenience the Dirichlet boundary conditions are ignored at this stage i.e. the testfunctions $\vec{v}$ and q are chosen such that $\vec{v} \in H^1(\Omega)^2$ and $q \in L^2(\Omega)$ with $H^1(\Omega)$ the space of functions which are square integrable and have square integrable derivatives and $L^2(\Omega)$ the space of square integrable functions. This choice implies that some extra equations are added to the system of equations that will arise after the discretization. These extra equations can be skipped in the solution procedure when the Dirichlet boundary conditions are incorporated. The velocity and pressure are approximated by a linear combination of time independent basis functions φ_{in} resp. ψ_m:

$$u_i^h = \sum_n u_{in}\varphi_{in} \qquad n=1,\ldots,N \quad i=1,2 \qquad (2.5a)$$

$$p^h = \sum_m p_m\psi_m \qquad m=1,\ldots,M \qquad (2.5b)$$

After substitution of (2.5), the following set of non-linear ordinary differential equations is obtained:

$$\begin{cases} M\dot{\underline{u}} + [S + N(\underline{u})]\underline{u} + L^T\underline{p} = \underline{f} + \underline{b} \\ L\underline{u} = \underline{0} \end{cases} \qquad (2.6)$$

with $\underline{u}$ a vector of length 2N containing the velocity parameters u_{in} (i=1,2 n=1,...,N) and $\underline{p}$ a vector of length M containing the pressure parameters p_m (m=1,...,M). $\dot{\underline{u}}$ refers to differentiation of $\underline{u}$ with respect to time. Furthermore:
M is the mass matrix defined as (k=1,...,N and l=1,...,N) :

$$M = \begin{bmatrix} M^{11} & M^{12} \\ M^{21} & M^{22} \end{bmatrix} \quad \text{with } M^{ij}(k,l) = \rho\,\delta_{ij}\int_\Omega \varphi_{ik}\varphi_{jl}\,d\Omega \qquad (2.7a)$$

S is the diffusion matrix (k=1,...,N and l=1,...,N) :

$$S = \begin{bmatrix} S^{11} & S^{12} \\ S^{21} & S^{22} \end{bmatrix} \quad \text{with}$$

$$S^{ij}(k,l) = \int_{\Omega} \eta \Big[\sum_{\alpha=1}^{2} \Big(\frac{\partial \varphi_{ik}}{\partial x_\alpha} \frac{\partial \varphi_{jl}}{\partial x_\alpha} \Big) \delta_{ij} + \frac{\partial \varphi_{ik}}{\partial x_j} \frac{\partial \varphi_{jl}}{\partial x_i} \Big] d\Omega \qquad (2.7b)$$

$N(\underline{u})\underline{u}$ is the non-linear convection term (k=1,...,N , i=1,2) :

$$[N(\underline{u})\underline{u}]_{ik} = \sum_{j=1}^{2} \int_{\Omega} \varrho \Big[\sum_{n=1}^{N} u_{jn} \varphi_{jn} \sum_{l=1}^{N} u_{il} \frac{\partial \varphi_{il}}{\partial x_j} \Big] \varphi_{ik} d\Omega \qquad (2.7c)$$

L is the divergence matrix (m=1,...,M and l=1,...,N) :

$$L = [L^1 \; L^2] \quad \text{with } L^i(m,l) = -\int_{\Omega} \psi_m \frac{\partial \varphi_{il}}{\partial x_i} \, d\Omega \qquad (2.7d)$$

$\underline{f}$ is the force vector (k=1,...,N) :

$$\underline{f} = [\underline{f}^1 \; \underline{f}^2]^T \quad \text{with } \underline{f}^i(k) = \int_{\Omega} \varrho f_i \varphi_{ik} d\Omega \qquad (2.7e)$$

and $\underline{b}$ is the boundary stress vector resulting from integration by parts of the diffusive and pressure terms in the momentum equations (k=1,...,N) :

$$\underline{b} = [\underline{b}^1 \; \underline{b}^2]^T \quad \text{with } \underline{b}^i(k) = \int_{\Gamma} \sum_{j=1}^{2} \sigma_{ij} n_j \varphi_{ik} d\Omega \qquad (2.7f)$$

Penalty function approach.

The set of ordinary differential equations (2.6) can be solved using a finite difference approximation of the time-derivative $\dot{\underline{u}}$ (see section 2.3). Direct solution of the resulting set of equations is time and memory consuming owing to the fact that zero components appear on the principal diagonal of the coefficient matrix. These

zero coefficients are due to the absence of the pressure in the continuity equation and in general require a partial pivoting procedure which disturbes the band structure of the matrix. To overcome this difficulty , the penalty function method can be applied (see appendix 2) by solving instead of (2.6) :

$$\underline{M}\dot{\underline{u}}_\varepsilon + [S + N(\underline{u}_\varepsilon) + L^T M_p^{-1} L\,]\underline{u}_\varepsilon = \underline{f} + \underline{b}$$

$$p_\varepsilon = \frac{1}{\varepsilon} M_p^{-1} L \underline{u}_\varepsilon \qquad (2.8)$$

with :

$$M_p(k,l) = \int_\Omega \psi_k \psi_l \, d\Omega \qquad \begin{matrix} k=1,\ldots,M \\ l=1,\ldots,M \end{matrix} \qquad (2.9)$$

Caray and Krishnan (1984) showed that for the steady Navier-Stokes equations the solution of (2.8) converges to the solution of (2.6) with the following error bound :

$$||\vec{u}_\varepsilon^h - \vec{u}^h||_{V^h} + ||p_\varepsilon^h - p^h||_{Q^h} < C\varepsilon \qquad (2.10)$$

with C independent of ε and $V^h = V_1^h \times V_2^h$, V_i^h the space spanned by the basis functions φ_{ik} (i.e. $V_i^h = \mathrm{span}\{\varphi_{ik}; 1 \le k \le N\}$) and Q^h the space spanned by the basis functions ψ_k (i.e. $Q^h = \mathrm{span}\{\psi_k; 1 \le k \le M\}$) (see also appendix 2). These results are confirmed by numerical experiments of Reddy (1982). The main advantage of the penalty function method over the direct solution of equations (2.6) is, that the pressure is eliminated from the momentum equations resulting in a smaller set of equations that can be solved without the demand of pivoting procedures.

The extended quadratic conforming (P_2^+-P_1) element.

In order to construct a finite element approximation of the Navier-Stokes equations, the finite dimensional space which spans the approximate solution must satisfy the discrete inf-sup (or Brezzi-Babuska) condition in order to guarantee a unique solution (see

appendix 1). An overview of elements satisfying (and not satisfying) this condition can be found in the studies of Fortin (1981), Fortin and Fortin (1985), Bercovier (1977) and Raviart (1984). Among the group of elements satisfying the discrete inf-sup condition it is possible to distinguish between elements with continuous approximate pressures (Taylor-Hood-like elements, Taylor and Hood (1973)) and elements with discontinuous approximate pressures (Crouzeix and Raviart, 1973). The latter type of element has the advantage that the projection matrix M_p (see (2.9) and at the end of appendix 2) is a local matrix and can be calculated and inverted element-wise. Discontinuous pressure elements therefore are favourable for penalized formulations of the equations. The simplest discontinuous pressure element in which the velocity is approximated linearly per element and the pressure is constant per element (P_1-P_0, see Fig. 2.2a) does not satisfy the Brezzi-Babuska condition (Raviart, 1984). If the velocity field is approximated by quadratic functions and the pressure is constant per element (P_2-P_0, see Fig. 2.2b) i.e. :

$$P_2(T) = \text{span}\{\lambda_1^2, \lambda_2^2, \lambda_3^2, \lambda_1\lambda_2, \lambda_2\lambda_3, \lambda_1\lambda_3\}$$

$$P_0(T) = \text{span}\{1\} \qquad (2.11)$$

with λ_i the baricentric co-ordinate of a point $\vec{x} \in IR^2$ with respect to the vertices of the triangle T, the Brezzi-Babuska condition is satisfied and the error bound :

$$||\vec{u}^h - \vec{u}||_{V^h} + ||p^h - p||_{Q^h} \leq C_1 h \qquad (2.12)$$

can be derived for $\vec{u}$ and p smooth enough (i.e. $\vec{u} \in H^2(\Omega)$ and $p \in H^1(\Omega)$) and a triangulation of Ω with triangles whose diameters are $\leq h$ (Raviart, 1984). A family of elements with important advantages is based on the discontinuous pressure elements introduced by Crouzeix and Raviart (1973). They enriched the polynomials of degree 2 of the P_2-P_0 element with a polynomial of degree 3 that vanishes on the element boundary (see Fig 2.2c). The Brezzi-Babuska condition then can be satisfied for pressures of degree ≤ 1. With the definitions :

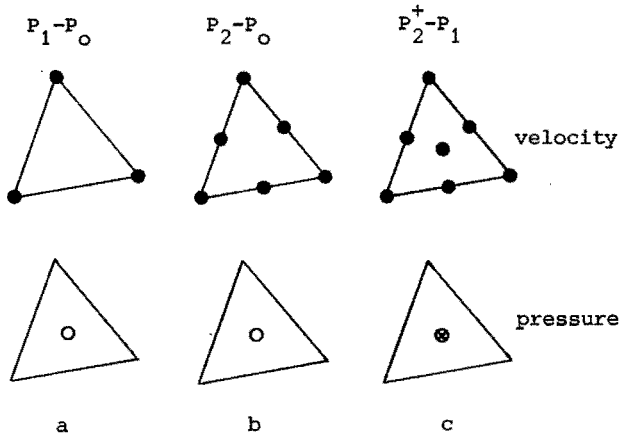

Fig. 2.2 : a) The P_1-P_0 element, b) The P_2-P_0 element, c) The extended quadratic triangular P_2^+-P_1 element (⊗: pressure and pressure derivatives).

$$P_2^+(T) = P_2(T) \oplus \lambda_1\lambda_2\lambda_3$$

$$= \text{span}\{\lambda_1^2, \lambda_2^2, \lambda_3^2, \lambda_1\lambda_2, \lambda_2\lambda_3, \lambda_1\lambda_3, \lambda_1\lambda_2\lambda_3\}$$

$$P_1(T) = \text{span}\{1, x-x_c, y-y_c\} \qquad (2.13)$$

with (x_c, y_c) the co-ordinates of the centroid of the element, an error bound :

$$||\vec{u}^h-\vec{u}||_{V^h} + ||p^h-p||_{Q^h} \leq C_2 h^2 \qquad (2.14)$$

is found if $\vec{u}$ and p are smooth enough (i.e. $\vec{u} \in H^3(\Omega)^2$ and $p \in H^2(\Omega)$) (Raviart, 1984). More specified the error bounds are (Crouzeix and Raviart, 1973) :

$$||\vec{u}^h-\vec{u}||_{L^2(\Omega)} \leq c_1 h^3$$

$$||p^h-p||_{L^2(\Omega)} \leq c_2 h^2 \qquad (2.15)$$

The advantage of defining the pressure and its first derivatives in the centroid of the element is, that, as proposed by Griffiths (1979), the P_2^+-P_1 element can be reduced to a P_2-P_0-like element for computational purposes by eliminating the velocities and pressure derivatives in the centroid (see Van de Vosse et al.,1985 or Cuvelier et al.,1896). In this way the number of unknowns per element is reduced from 17 to 13. This modified (P_2^+-P_1) element has proved to satisfy the error bounds as given in (2.15) for practical test calculations of steady problems (Segal, 1979).

2.3.Time integration of the equations.

The time derivative in the discrete Navier-Stokes equations (2.6) or (2.8) can be approximated by a finite difference θ-method. Considering the equation :

$$\dot{\underline{u}} = A\underline{u} + \underline{f} \tag{2.16}$$

this approximation is defined by :

$$\frac{\underline{u}^{n+1} - \underline{u}^n}{\Delta t} = \theta A\underline{u}^{n+1} + (1-\theta)A\underline{u}^n + \underline{f}^{n+\theta}$$

$$\text{with } \underline{f}^{n+\theta} = \theta\underline{f}^{n+1} + (1-\theta)\underline{f}^n \qquad 0 \leq \theta \leq 1 \tag{2.17}$$

For θ=0 resp. θ=1 this scheme reduces to the Euler explicit (EE), Euler implicit (EI) method respectively, both $O(\Delta t)$ accurate for linear equations. For θ=0.5 the scheme becomes the Crank-Nicolson scheme (CN) which is of $O(\Delta t^2)$ accurate for linear equations.

In order to make a proper choice for the value of θ, the time integration of a linear set of ordinary differential equations resulting from the discretisation of a parabolic differential equation is considered :

$$\begin{cases} \dot{\underline{u}} = A\underline{u} + \underline{f} \\ \underline{u}(t_0) = \underline{u}_0 \end{cases} \tag{2.18}$$

Here A is assumed to be a (NxN) matrix with real coefficients independent of time, resulting from a linear elliptic differential operator. Furthermore it is assumed that A is non-defect, i.e. has N linear independent eigenvectors. Owing to the linear independence of the N eigenvectors, a non-singular matrix B with complex coefficients exists defined by :

$$A\,B = B\,\Lambda \tag{2.19}$$

with $\Lambda=\mathrm{diag}(\lambda_1,\ldots,\lambda_N)$ and $\lambda_1,\ldots,\lambda_N$ the eigenvalues of A. The differential equation and also its discretized approximation is called stable when a finite error $\underline{\varepsilon}_0$ in the initial condition $\underline{u}_0$ results in a finite error $\underline{\varepsilon}(t)$ in $\underline{u}(t)$, for any t. To evaluate this error propagation two cases are considered :

1) $\underline{u}$ is a solution of (2.18) with $\underline{u}(t_0)=\underline{u}_0$

2) $\underline{\xi}$ is a solution of (2.18) with $\underline{u}(t_0)=\underline{u}_0+\underline{\varepsilon}_0$
   with $\underline{\varepsilon}_0$ a small perturbation of $\underline{u}_0$.

If $\underline{\varepsilon}$ is defined as $\underline{\varepsilon}=\underline{\xi}-\underline{u}$ then $\dot{\underline{\varepsilon}}=A\underline{\varepsilon}$ and $\underline{\varepsilon}(t_0)=\underline{\varepsilon}_0$ or, since B is non-singular, $\underline{\eta}=B^{-1}\underline{\varepsilon}$ can be defined and thus :

$$\dot{\underline{\eta}} = \Lambda\underline{\eta} \tag{2.20}$$

with :

$$\underline{\eta}(t_0) = B^{-1}\underline{\varepsilon}_0 \equiv \underline{\eta}_0$$

The solution of (2.20) then can be written as :

$$\eta_i = \eta_{i0}e^{\lambda_i(t-t_0)} \qquad i=,\ldots,N \tag{2.21}$$

In order that the differential equation is stable, η_i must be a non-increasing function of time, hence :

$$\mathrm{Re}[\lambda_i] \leq 0 \tag{2.22}$$

must hold for any i (i=1,...,N).

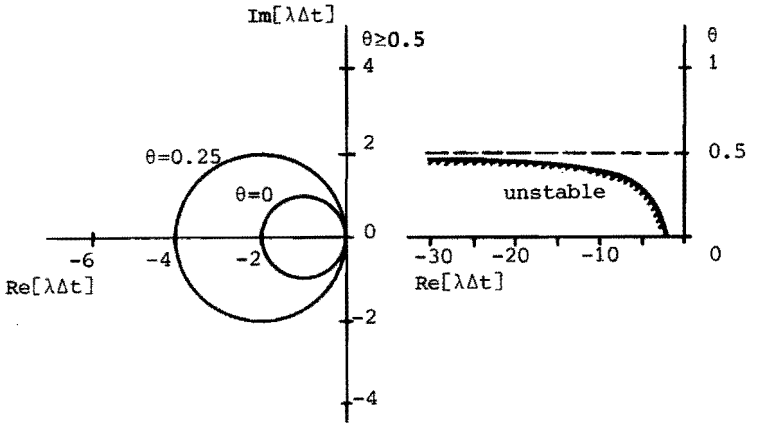

Fig. 2.3 : Stability regions of the θ-method for complex and real eigenvalues, respectively.

Numerical time integration schemes generally lead to equations for $\underline{n}$ of the form :

$$\underline{n}^{n+1} = G\underline{n}^{n} \qquad (2.23)$$

with G the so-called multiplication matrix and $\underline{n}^{n}=\underline{n}(t_n)$. For stability of the numerical scheme it is necessary that $||G|| \leq 1$ (with $||G||$ any regular vector norm). For the θ-method one easily verifies that this leads to :

$$|c_i| = \left| \frac{1+(1-\theta)\lambda_i \Delta t}{1-\theta\lambda_i \Delta t} \right| < 1 \qquad i=1,\ldots,N \qquad (2.24)$$

In Fig. 2.3 the stability regions of $\lambda_i\Delta t$ are given for the interval $0 \leq \theta \leq 1$. For $0.5 \leq \theta \leq 1$ the scheme appears to be stable for all $\lambda\Delta t$. For $0 \leq \theta \leq 0.5$ the scheme is only conditionally stable. In the case that the eigenvalues of A are large (but negative), relative small timesteps Δt have to be applied to ensure stability.

In Fig. 2.4, the amplification factor c_i is plotted as a function of Re[λΔt] for θ=1 and θ=0.5 respectively. From these figures it can be observed that for θ=0.5 (CN) the amplification tends to -1 for large negative eigenvalues, whereas for θ=1 (EI) the amplification

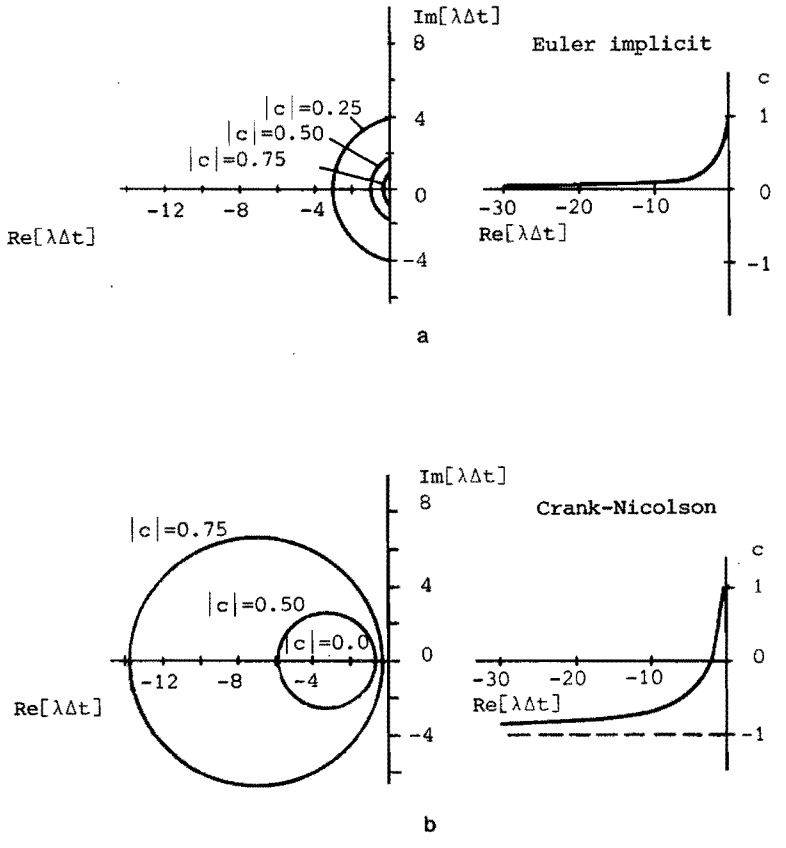

Fig. 2.4 : Amplification factor c as a function of (λΔt) for the EI (a) and the CN (b) method for complex and real eigenvalues, respectively.

tends to 0. The same holds for complex eigenvalues with a dominating large negative real part. For an increasing imaginary part of the eigenvalues, the amplification factor of the Crank-Nicolson method increases whereas the Euler-implicit method gives rise to a decrease of this factor, resulting in a damping of oscillations related with these eigenvalues.

Linearization of the convective terms.

Application of the θ-method of time-integration to (2.8) gives:

$$\underline{\underline{M}}\frac{\underline{u}^{n+1}+\underline{u}^{n}}{\Delta t} + \theta[S+N(\underline{u}^{n+1}) + \frac{1}{\varepsilon}L^{T}M_{p}^{-1}L]\underline{u}^{n+1} = \underline{f}^{n+\theta}+\underline{b}^{n+\theta} +$$

$$(1-\theta)[S + N(\underline{u}^{n}) + L^{T}M_{p}^{-1}L]\underline{u}^{n}$$

$$\underline{p}^{n+1} = \frac{1}{\varepsilon}M_{p}^{-1}L\underline{u}^{n+1} \qquad (2.25)$$

(note that the subscript ε has been skipped).
This set of non-linear equations can be solved by one step of a Newton-Raphson iteration leading to :

$$(M + \theta\Delta t[S + J(\underline{u}^{n}) + \frac{1}{\varepsilon}L^{T}M_{p}^{-1}L])\underline{u}^{n+1} = \underline{f}^{n+\theta}+\underline{b}^{n+\theta}+$$

$$(M - (1-\theta)\Delta t[S + \frac{1}{\varepsilon}L^{T}M_{p}^{-1}L])\underline{u}^{n} - (1-2\theta)\Delta t N(\underline{u}^{n})\underline{u}^{n}$$

$$\underline{p}^{n+1} = \frac{1}{\varepsilon}M_{p}^{-1}L\underline{u}^{n+1} \qquad (2.26)$$

with $J(\underline{u}^{n})$ the Jacobian of $N(\underline{u}^{n})\underline{u}^{n}$ defined by :

$$J(\underline{u}^{n})^{ij}(k,l) = \frac{\partial}{\partial u_{jl}^{n}}[N(\underline{u}^{n})\underline{u}^{n}]_{ik}$$

$$= \sum_{q} u_{iq}^{n} \int_{\Omega} \rho\varphi_{jl}\frac{\partial\varphi_{iq}}{\partial x_{j}}\varphi_{ik}d\Omega +$$

$$\delta_{ij}\sum_{m}\sum_{q} u_{mq} \int_{\Omega} \rho\varphi_{mq}\frac{\partial\varphi_{il}}{\partial x_{m}}\varphi_{ik}d\Omega$$

$$i,j,m=1,2\ ,\ q,k,l=1,\ldots,N \qquad (2.27)$$

It can readily be proved that the Newton step (2.26) is equivalent to

the linearization :

$$N(\underline{u}^{n+1})\underline{u}^{n+1} = N(\underline{u}^{n})\underline{u}^{n+1} + N(\underline{u}^{n+1})\underline{u}^{n} - N(\underline{u}^{n})\underline{u}^{n}$$

$$= J(\underline{u}^{n})\underline{u}^{n+1} - N(\underline{u}^{n})\underline{u}^{n} \qquad (2.28)$$

Substitution of $\underline{u}^{n+1}=\frac{1}{\theta}[\underline{u}^{n+\theta}-(1-\theta)\underline{u}^{n}]$ in (2.26) leads to an equivalent solution procedure consisting of two steps :

1: $$[\frac{1}{\theta\Delta t}M + S + J(\underline{u}^{n}) + \frac{1}{\varepsilon}L^{T}M_{p}^{-1}L]\underline{u}^{n+\theta} = \frac{1}{\theta\Delta t}M\underline{u}^{n} + \underline{f}^{n+\theta} + \underline{b}^{n+\theta}$$

$$\underline{p}^{n+\theta} = \frac{1}{\varepsilon}M_{p}^{-1}L\underline{u}^{n+\theta} \qquad (2.29a)$$

2: $$\underline{u}^{n+1} = \frac{1}{\theta}[\underline{u}^{n+\theta} - (1-\theta)\underline{u}^{n}]$$

$$\underline{p}^{n+1} = \frac{1}{\theta}[\underline{p}^{n+\theta} - (1-\theta)\underline{p}^{n}] \qquad (2.29b)$$

The first step of equations (2.29) is a Euler implicit step to the time level n+θ, which is unconditionally stable and has the properties as described in the previous section ($c_i=1/|1+\theta\Delta t\lambda_i|$). The second step of (2.29) is an extrapolation to time level n+1 which is only conditionally stable ($c_i=|1+(1-\theta)\lambda_i\Delta t|$,see Fig. 2.5). The amplification factor c after execution of both steps is equal to the amplification factor as obtained for the original θ-method. As will be elucidated in the next section, this two-step formulation has, besides a simpler way of implementation, some advantages above the formulation as used in (2.26).

Finally it is remarked that for the stationary Navier-Stokes equations the following Newton-Raphson iteration can be used :

$$[S + J(\underline{u}^{\nu}) + \frac{1}{\varepsilon}L^{T}M_{p}^{-1}L]\underline{u}^{\nu+1} = \underline{f} + \underline{b} + N(\underline{u}^{\nu})\underline{u}^{\nu} \qquad \nu=0,\ldots,\nu_m$$

$$\underline{p}^{\nu_m+1} = \frac{1}{\varepsilon}M_{p}^{-1}L\underline{u}^{\nu_m+1} \qquad (2.30)$$

The iteration can be stopped when $||\underline{u}^{\nu_m+1} - \underline{u}^{\nu_m}|| < \delta$, δ being the required accuracy.

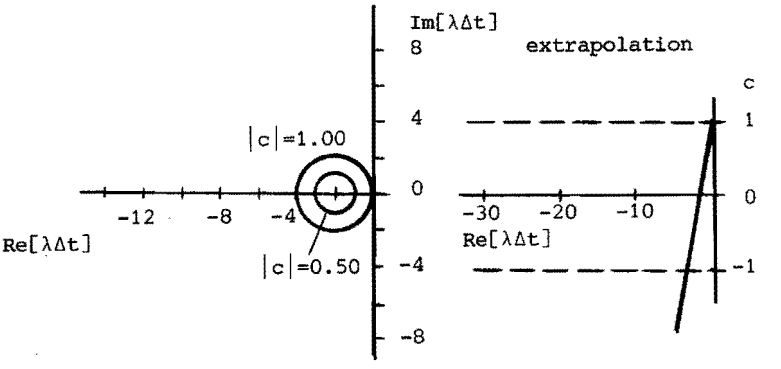

Fig. 2.5 : Amplification factor c as a function of ($\lambda\Delta t$) for the extrapolation step in the CN time integration for complex and real eigenvalues, respectively.

2.4 Numerical test of the stability and accuracy of the time integration.

To predict the behaviour of the θ-method, knowledge of the magnitude of the eigenvalues is needed. Although the eigenvalues are not known beforehand, it is obvious that, as far as the Stokes equations are concerned, large negative real eigenvalues will occur owing to the small penalty parameter in the equations (2.26). From Fig. 2.4 it follows that the Euler implicit method will damp errors related with these eigenvalues because the corresponding amplification factor tends to zero. On the other hand the Crank-Nicolson method gives rise to amplification factors tending to -1 for these eigenvalues (see Fig. 2.4). Errors therefore will be propagated in an oscillatory way and will damp relatively slowly. If these oscillations are present in the calculated velocity, they will give rise to relatively large oscillations in the pressure because of the division by the penalty parameter ε in equation (2.26). With respect to this phenomenon, the modified (two-step) formulation of the θ-method offers some advantages. Since the velocity at time-level $n+\theta$ is obtained by a Euler implicit step, these velocities will not give rise to oscillations

caused by an amplification factor tending to -1. In consequence, also the pressure at time-level n+θ will be free from these oscillations. Since the pressure at time-level n+1 is not needed to continue the time integration, one can omit the second step (2.29b) for the pressure and evaluate the pressure only for time levels n+θ. A confirmation of this will be given by the numerical tests described below.

Although preceding analysis only holds for linear equations with constant coefficients in time and therefore can only be applied to the Stokes equations, similar behaviour of the time integration can be expected for the Navier-Stokes equations. Besides the behaviour of the time integration for eigenvalues with a large negative real part, also the behaviour for eigenvalues with a dominating imaginary part is of interest. These eigenvalues will occur for equations with an important contribution of the convective terms. These terms give rise to a non-symmetric matrix and complex eigenvalues. From Fig. 2.4 it can be seen that the amplification factor of the Euler implicit method decreases for an increasing imaginary part of the eigenvalues. On the contrary, the Crank-Nicolson method gives rise to an increase of the amplification factor and therefore will not damp oscillations related with these eigenvalues. Since these oscillations are inherent to the physical problem, it is expected that the Crank-Nicolson method is preferable for these problems. In the next section this will be confirmed by the results of the calculation of a Von Karman vortex street.

The stability and accuracy of the time integration methods described are elucidated by computations of oscillating flow in a channel (two parallel plates) and the vortex shedding past a cylinder. The oscillating channel flow, which can be described by the Stokes equations, is chosen because an exact solution can be derived. The non-linear convective terms are neglected and only real eigenvalues occur. To get an idea of the influence of an imaginary part of the eigenvalues on the behaviour of the time integration, also the vortex shedding phenomenon is analysed. There the convective terms do play an important role.

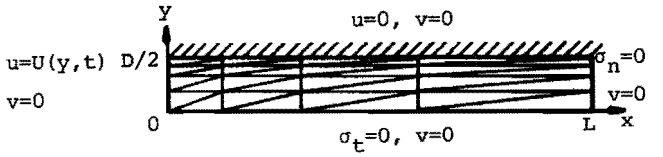

Fig. 2.6 : Geometry and boundary conditions for the oscillating channel flow problem (L=15D), $U(y,t)=U_0(1-(2y/D)^2)\cos\omega t$, $\alpha\approx 8$.

Fully developed oscillating flow between two parallel plates.

To elucidate the stability and accuracy of the time integrations used, the development from rest of oscillating flow between two parallel plates was analysed. For convenience an oscillating parabolic velocity profile was used as an inflow condition (see Fig. 2.6).

The exact solution of the fully developed flow can be determined in a similar way as the fully developed oscillating flow in a circular cylinder (Schlichting, 1979) and is given by:

$$u = \mathrm{Re}\left[Q_0 \left(\frac{1-K(\alpha,y)}{1-P(\alpha)} \right) e^{i\omega t} \right] \quad , \; v = 0 \tag{2.31a}$$

$$\frac{\partial p}{\partial x} = \mathrm{Re}\left[-i\omega Q_0 \left(\frac{1}{1-P(\alpha)} \right) e^{i\omega t} \right] \quad , \; \frac{\partial p}{\partial y} = 0 \tag{2.31b}$$

with $x=x_1/D$, $y=x_2/D$, $u=u_1/U_0$, Q_0 the flow amplitude ($Q_0=\frac{2}{3}U_0D$), D the channel height, U_0 the velocity amplitude , Re[..] is real part of [..] , $i=\sqrt{-1}$ and :

$$K(\alpha,y) = \frac{e^{\alpha\sqrt{iy}} + e^{-\alpha\sqrt{iy}}}{e^{\alpha\sqrt{i}} + e^{-\alpha\sqrt{i}}} \tag{2.32a}$$

$$P(\alpha) = \frac{1}{\alpha\sqrt{i}} \frac{e^{\alpha\sqrt{i}} - e^{-\alpha\sqrt{i}}}{e^{\alpha\sqrt{i}} + e^{-\alpha\sqrt{i}}} \tag{2.32b}$$

$$\alpha = D\sqrt{\omega/\nu} \tag{2.32c}$$

The solution is approximated by solving the unsteady Stokes equations for an angular frequency ω, a viscosity ν and a channel height D, such that the frequency parameter α leads to a value of $\alpha \approx 8$, corresponding with certain physiological flows. The length of the channel was taken to be 15D. As the pressure derivative did not change in the first 3 significant decimals in the last and last but one element upstream the outlet, the conclusion is justified that the assumed channel length is sufficient to guarantee a fully developed oscillating flow at the outlet. Comparisons of numerical and analytical solutions are made for different θ-values in the time integration with time steps of 0.2, 0.1 and 0.05 times the cycle period T of the flow, respectively, and with the aid of the following error definitions:

$$\Delta u = \left. \frac{\left[\int_0^{1/2} (u - u^h)^2 dy \right]^{1/2}}{\left[\int_0^{1/2} u^2 dy \right]^{1/2}} \right|_{x=\,15} \qquad (2.33a)$$

$$\Delta p_x = \left. \frac{\left| \frac{\partial p}{\partial x} - \frac{\partial p^h}{\partial x} \right|}{\left| \frac{\partial p}{\partial x} \right|} \right|_{x=15\ ,\ y=0} \qquad (2.33b)$$

As expected from (2.24) the time integration was unstable for $0 \leq \theta < 0.5$ for all timesteps used. The large negative eigenvalues resulting from the penalty function method would require timesteps of order ε. Since θ-values in the range $0.5 < \theta < 1$ also results in a first order accuracy just like (θ=1), only the EI and CN time integrations were analysed in detail.

a) The Euler implicit scheme (EI) :

Figs. 2.7a and 2.7b show the velocity profiles and pressure gradient approximations in the fifth period for $\Delta t/T = 0.2$, $\Delta t/T = 0.1$ and $\Delta t/T = 0.05$, respectively, together with the exact solution. In Fig. 2.7c the relative errors as defined in (2.33) are plotted against the time for the first five periods of the flow oscillation.

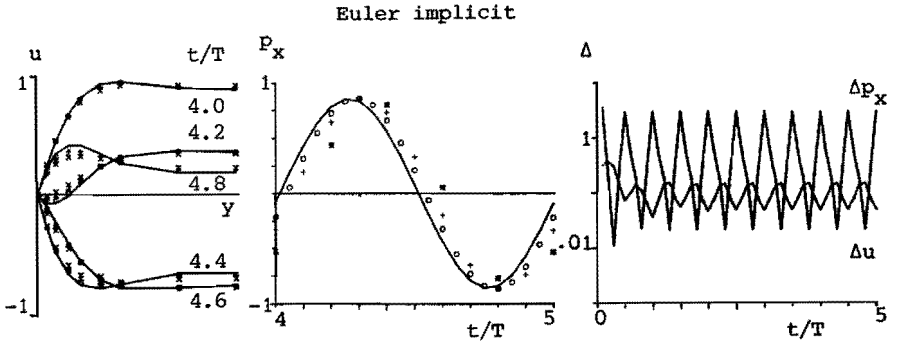

Fig. 2.7 : a) Velocity profiles at the outstream (-: exact, *: $\Delta t/T=0.2$, +: $\Delta t/T=0.1$, o: $\Delta t/T=0.05$) during one flow cycle.
b) Pressure gradients at the outstream (-: exact, *: $\Delta t=0.2$, +: $\Delta t=0.1$, o: $\Delta t=0.05$) during one flow cycle.
c) Relative errors in the velocity and pressure gradients at the outstream during 5 flow cycles ($\Delta t/T=0.1$).

The timestep used was $\Delta t/T=0.1$. The corresponding errors were averaged in time and are given as a function of Δt in Table 2.1. The large errors found for the pressure derivatives are attributed to the phase-lag between the exact and approximated solutions, as is visible in Fig. 2.7b.

b) The Crank-Nicolson scheme (CN) :

The same analysis was performed for the case that the CN-scheme was used (Figs. 2.8a, 2.8b, 2.8c and Table 2.1). From these results it is concluded that the CN-scheme gives considerably better velocity approximations but worse pressure approximations. As can be seen from Fig. 2.8b , the worse pressure approximations are the result of undamped oscillations. These oscillations are the consequence of the amplification factor tending to -1 for large negative eigenvalues of the coefficient matrix.

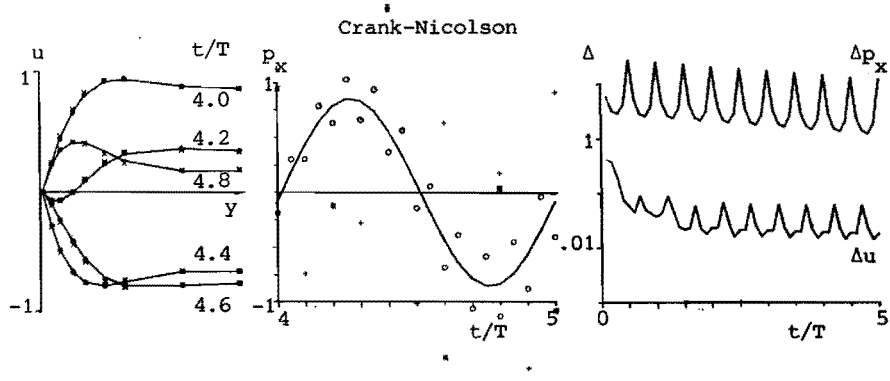

Fig. 2.8 : a) Velocity profiles at the outstream (-: exact, *: Δt/T=0.2, +: Δt/T=0.1, o: Δt/T=0.05) during one flow cycle.
b) Pressure gradients at the outstream (-: exact, *: Δt=0.2, +: Δt=0.1, o: Δt=0.05) during one flow cycle.
c) Relative errors in the velocity and pressure gradients at the outstream during 5 flow cycles (Δt/T=0.1).

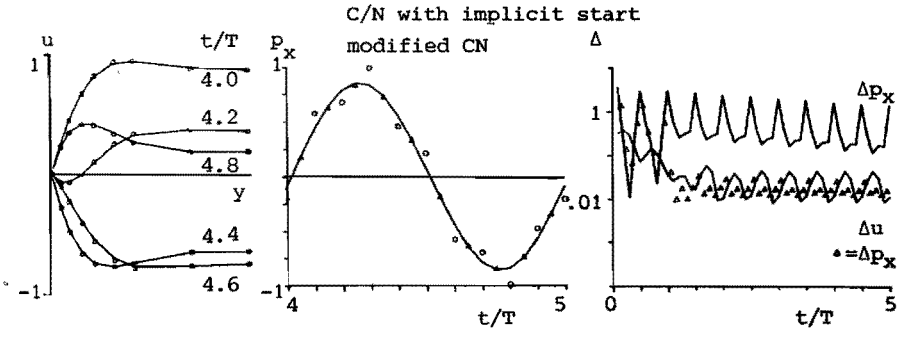

Fig. 2.9 : a) Velocity profiles at the outstream (Δt/T=0.1) (-: exact, o: CN with implicit start, Δ: modified CN) during one flow cycle.
b) Pressure gradients at the outstream (Δt/T=0.1) (-: exact, o: CN with implicit start, Δ: modified CN) during one flow cycle.
c) Relative errors in the velocity and pressure gradients at the outstream during 5 flow cycles (Δt/T=0.1) (-: CN with implicit start, Δ: modified CN).

c) The Crank-Nicolson scheme with an implicit start (ISCN) :

Better results are obtained when the errors induced by the arbitrary initial value (u=0) are damped by an implicit start of the CN-scheme. In Fig. 2.9 the results of the ISCN-scheme are given for a timestep $\Delta t/T=0.1$ (see for averaged values Table 2.1). In the ISCN-scheme the first period of the flow oscillation was integrated with the EI-scheme. The results of the CN-scheme are considerably improved when an implicit start is used to damp the errors induced by the assumed initial value.

d) The modified Cranc-Nicolson method with an implicit start (MCN)

From Fig. 2.9b,c and Table 2.1 it can be seen that significant better results for the pressure can be obtained if the pressure is evaluated at the timesteps n+ϑ. In fact this means that only the first step of (2.29) is executed for the pressure. Since the pressure on time level n+1 is not needed to continue the time integration, the second relation of (2.29b) can be omitted. The pressure now is approximated with about the same accuracy as the velocity for a timestep $\Delta t/T=0.1$.

Table 2.1 : Time averaged relative errors in the velocity and the pressure gradient for the EI, CN, ISCN and MCN method, respectively.

method	Euler Implicit		Crank-Nicolson		CN impl.start		modified CN impl.start	
$\Delta t/T$	Δu	Δp_x	Δu	Δp_x	Δu	Δp_x	Δu	Δp_x
0.20	0.16	2.13	0.05	5.15	-	-	-	-
0.10	0.09	1.01	0.03	4.19	0.02	0.57	0.02	0.02
0.05	0.05	0.40	0.02	0.76	-	-	-	-

Another way of analysing the fully developed oscillating channel flow is using an oscillatory normal stress at the inflow instead of the Dirichlet conditions used here. Then only one element in x-direction is needed since the pressure only varies linearly and the velocity does not change at all in that direction. However, this has two important disadvantages compared with the Dirichlet boundary conditions. Firstly the pressure is found to be independent of the timestep used. In fact the pressure is prescribed indirectly by the normal stresses, so no information on the accuracy of the pressure approximation can be obtained. Secondly, a rather long transition time of about 20 time cycles was found before the velocity was fully developed in time. The errors for the velocity were observed to be of the same order as in the problem with the Dirichlet boundary conditions.

Vortex shedding behind a circular cylinder.

To evaluate the behaviour of the two time integration methods in a more complicated flow situation, the vortex shedding behind a circular cylinder with a diameter D=1 was simulated. The geometry was chosen equal to the geometry used by Gresho et al.(1980) and is shown in Fig. 2.10. Uniform Dirichlet inflow boundary conditions ($u=U_0=1, v=0$) and stress-free outflow conditions were used, together with moving wall conditions ($u=1, v=0$) at the upper and lower walls. The Reynolds number based on the diameter of the cylinder was taken to be 100. Both the Euler implicit and the Crank-Nicolson time integration methods arrived at a steady solution after about 30 timesteps of $\Delta t/\tau=1$ ($\tau=D/U_0=1$). Owing to the symmetry of the mesh and boundary conditions, the vortex shedding was not generated spontaneously. To trigger the vortex shedding, the steady solution was disturbed in one timestep by setting the velocity of the cylinder to $0.1U_0$ in y-direction. Next, 10 EI timesteps were performed to damp this distortion and to avoid hereby a too important influence on the flow field. After these implicit steps both integration schemes were applied with timesteps $\Delta t/\tau=1$, resulting in a periodic shedding cycle as shown in Fig. 2.11a, where the velocity component in y direction at $(x,y)=(10,0)$ is plotted as a function of time . With the EI time integration the amplitude of the velocity component turns out to be

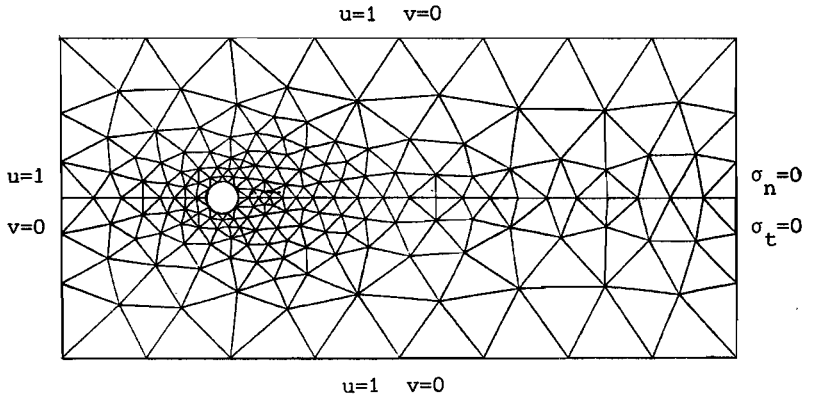

Fig. 2.10 : Geometry, mesh and boundary conditions for the vortex shedding computation (Re=100).

an order smaller in magnitude than when the CN scheme was used. Furthermore, the amplitude damps rapidly for increasing time. In Fig. 2.11b this velocity component is given for the CN method. The amplitude of this fluctuation agrees with the amplitude found by Gresho et al. (1980). The Strouhal number (fD/U_0) of the vortex shedding is predicted to be 0.17. Experiments by Tritton (1959) showed a Strouhal number of 0.16 for Re=100. Finally, in Fig. 2.12 the streamline pattern during one shedding cycle is given for 6 instants of time.

The performances of the EI scheme are expected to be better at smaller timesteps. Anyhow, it can be concluded that, although the EI time integration has its advantages with respect to the numerical stability of the solution, this first order scheme is far less applicable than the CN scheme in simulations of flows with an important convective property like the vortex shedding process.

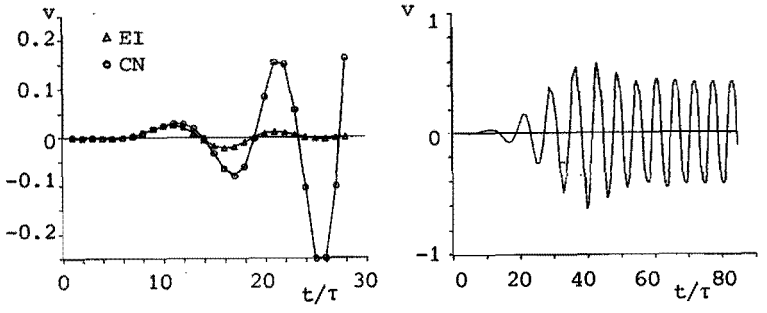

Fig. 2.11 : a) Velocity component in y-direction as a function of time : distortion at $t/\tau=1$, $0<t/\tau\leq 10$: EI, $t/\tau>10$: (Δ: EI, o: CN), $\Delta t/\tau=1$.
b) Velocity component in y-direction as a function of time : distortion at $t/\tau=1$, $0<t/\tau<10$: (EI,$\Delta t/\tau=1$), $10<t/\tau<40$: (CN,$\Delta t/\tau=1$), $40<t/\tau\leq 55$: (CN,$\Delta t/\tau=0.5$), $55<t/\tau\leq 85$: (CN,$\Delta t/\tau=0.25$).

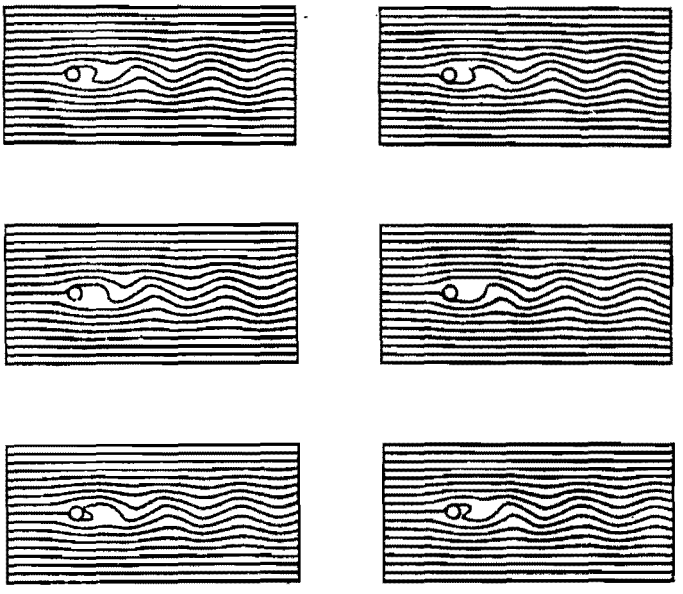

Fig. 2.12 : Streamline pattern during a shedding cycle (time difference 1τ).

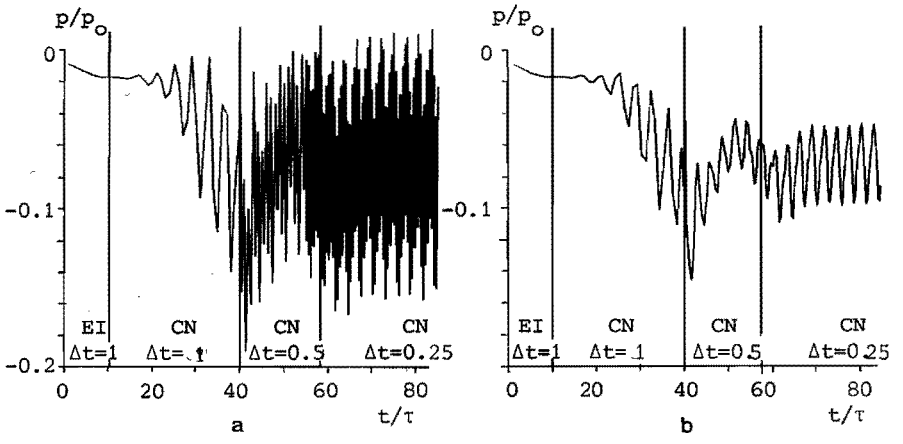

Fig. 2.13 : a) Pressure at x=(10.0) as a function of time evaluated at timelevels n+1 (a) and n+1/2 (b) respectively.

In Fig. 2.13 the pressure at point (x,y)=(10,0) is given as a function of time for time-levels n+1 (a) and n+1/2 (b). From this figure it is observed that although an implicit start is used in the time integration , a change in the magnitude of the timestep can cause oscillations in the pressure at time-levels n+1. However, the pressure at levels n+1/2 does not show these oscillations, because the unstable second relation of (2.29b) is omitted.

2.5.Concluding remarks.

As far as the spatial discretization of the Navier-Stokes equations is concerned, the $(P_2^+-P_1)$ Crouzeix-Raviart element provides an approximation with a third order of error for the velocity and a second order of error for the pressure.

The behaviour of the Euler implicit and Crank-Nicolson time integration schemes for the unsteady Stokes equations using a penalty finite element method can be explained by a simple stability analysis of linear parabolic differential equations in general. In that case, the performance of the integration methods for eigenvalues of the system of equations with a large negative real part is important with respect to possible numerical oscillations of the solution . The

first order EI algorithm has an amplification factor approaching zero when the real part of the eigenvalue goes to minus infinity. Therefore errors induced by the computation or errors due to the initial condition (often a steep velocity gradient in time) damp very quickly. On the contrary, the more accurate second order Crank-Nicolson rule gives rise to an amplification factor tending to -1, and therefore an oscillatory propagation of the introduced errors is expected. This phenomenon is illustrated by the analysis of the oscillating channel flow and the vortex shedding and is mainly visible in the worse pressure approximations. If the disturbance of the initial value is damped out by a fully implicit time integration, the pressure oscillations observed, for the (smooth) boundary conditions used here, were reduced significantly. However, as found in the vortex shedding calculation, a small disturbance such as a change of the magnitude of the timestep can cause a new appearance of these oscillations. Omittance of the extrapolation step in the Crank-Nicolson algorithm (2.29b) can be used to overcome this problem. Finally it is assumed that the stability properties are thought to be affected mostly by the penalty parameter. The non-linear convective terms give rise to complex eigenvalues. These are not expected to lead to much different stability properties. However, the (physically originated) oscillatory properties of the solution of the differential equations can be damped incorrectly by the EI scheme. The CN method with an implicit start is preferable then. This statement is confirmed by the computation of the vortex shedding behind a circular cylinder.

references.

- Batchelor G.K.,'An introduction to fluid dynamics.',Cambridge Univ.Press (1979).
- Bercovier M., 'Pertubation of mixed variational problems. Application to mixed finite element methods.', RAIRO Anal. Numer., 12, p 211-236 (1978).
- Bercovier M.,'A family of finite elements with penalisation for the numerical solution of Stokes and Navier-Stokes equations.', Information Processing 77, IFIP, Ed. Gilcrist B., North-Holland publishing Company (1977).

- Brezzi F.,'On the existence, uniqueness and approximation of saddle point problems arising from Lagrangian multipliers.' RAIRO Anal. Numer., 8-R2, p 129-151 (1974).
- Caray G.F. and Krishnan R.,'Penalty finite element method for the Navier-Stokes equations.', Comp. Meth. Appl. Mech. Eng., 47, p 183-224 (1984).
- Crouzeix M. and Raviart P.-A.,'Conforming and nonconforming finite element methods for solving the stationary Stokes equations I.', RAIRO Anal. Numer., 7, p 33-76 (1973).
- Cuvelier C., Segal A. and Van Steenhoven A.A.,'Finite element methods and Navier-Stokes equations.', D.Reidel Publishing comp. Dordrecht/Boston/Lancaster/Tokyo (1986).
- Engelman M.S., Sani R.L., Gresho P.M.and Bercovier M.,'Consistent vs. reduced integration penalty methods for incompressible media using several old and new elements.', Int. J. Num. Meth. Fluids', 2, p 25-42 (1982).
- Fortin M.,'An analysis of the convergence of mixed finite element methods.', RAIRO Anal. Numer., 11, p 341-354 (1977).
- Fortin M.,'Old and new finite elements for incompressible flows.', Int. J. Num. Meth. Fluids, 1, p 347-364 (1981).
- Fortin M. and Fortin A.,'Newer and newer elements for incompressible flow.', In : Finite elements in fluids, Eds. Gallagher R.H., Caray G.F., Oden J.T. and Zienkiewicz O.C., John Wiley & Sons Ltd (1985).
- Girault V. and Raviart P.-A.,'Finite element approximation of the Navier-Stokes equations.', Springer-Verlag, Berlin,Heidelberg, New York (1979).
- Gresho P.M., Lee R.L. and Sani R.L.,'On the time-dependent solution of the incompressible Navier-Stokes equations in two and three dimensions.', In : Recent advances in numerical methods in fluids, Eds. Taylor C. and Morgan K., Pineridge Press Ltd. (1980).
- Griffiths D.F.,'Finite element methods to solve the stationary Navier-Stokes equations.', Int. J. Num. Meth. Fluids., 2, p 269-280 (1985).
- Hughes T.J.R., Liu W.K. and Brooks A.,'Finite element analysis of incompressible viscous flows by the penalty function formulation.', J.Comp.Phys. , 30, p 1-60 (1979).

- Oden J.T., Kikuchi N. and Song Y.J.,'Penalty-finite element methods for the analysis of Stokesian flows.', Comp. Meth. Appl. Mech. Eng., 31, p 297-329 (1982).
- Raviart P.-A.,'Mixed finite element methods'. In : The mathematical basis of finite element methods., Ed. Griffiths D.F.,Clarendon Press,Oxford (1984).
- Reddy J.N.,'On penalty function methods in finite element analysis of flow problems.', Int. J. Num. Meth. Fluids., 2, p 151-171 (1982).
- Sani R.L., Eaton B.E., Gresho P.M., Lee R.L. and Chan S.T.,'On the solution of the time-dependent incompressible Navier-Stokes equations via a penalty Galerkin finite element method.', Num. Meth. Lam. Turb. Flow. in Proc. Second Int. Conf. (Venice), p 41-51 (1981).
- Schlichting H.,'Boundary-Layer Theory',7nd ed McGraw-Hill (1979)
- Segal A.,'On the numerical solution of the Stokes equations using the finite element method.', Comp. Meth. Appl. Mech. Eng., 19, p 165-185 (1979).
- Segal A. and Praagman N.,'SEPRAN user manual and programmers guide.', Ingenieurs buro SEPRA ,Leidschendam (1984).
- Taylor C. and Hood P.,'A numerical solution of the Navier-Stokes equations using the finite element technique.', Comp. Fluids, 1, p 73-100 (1973).
- Temam R.,'Navier-Stokes equations.', North-Holland,Amsterdam (1977).
- Tritton D.J.,'Experiments on the flow past a circular cylinder at low Reynolds numbers.', J. Fluid Mech., 6, p 547-567 (1959).
- Van de Vosse F.N., Segal A., Van Steenhoven A.A. and Janssen J.D.,'A finite element approximation of the unsteady two-dimensional Navier-Stokes equations.', Int. J. Num. Meth. Fluids, 6, p 427-443 (1986).

CHAPTER 3: STEADY AND UNSTEADY FLOW OVER A SQUARE STEP : A TWO-DIMENSIONAL STENOSIS MODEL.

3.1. Introduction.

In this chapter the steady and unsteady incompressible Newtonian flow over a square step is analysed by solving the Navier-Stokes equations as described in the previous chapter. Furthermore, the numerical approximations are validated by comparison with experimental data.

The choice to analyse the flow over a square step has been made for different reasons. First, this configuration is suitable to evaluate the numerical method for complex flow properties, including steady and time-dependent flow separation. Next, this and related flow configurations have been investigated intensively in various research disciplines, so that a comparison with solution procedures and both numerical and experimental data obtained from literature can be made. Furthermore, the two-dimensional flow over a square step can be regarded as a two-dimensional stenosis model from which some information on the flow properties at arterial stenoses can be obtained. The main purpose of the analysis described in this chapter, however, is to analyse the numerical results with respect to the boundary conditions and mesh distribution applied and to validate the numerical method by means of comparison with experimental results.

As mentioned above, the flow over steps or in ducts with sudden or gradual constrictions has been the subject of many investigations. Laminar steady flow over backward-facing steps has been studied experimentally by Goldstein et al. (1970), Denham and Patrick (1974), Sinha et al. (1981), Durst and Tropea (1983) and Armaly et al. (1983). From these studies it follows that the flow separation at the step edge results in a recirculation zone downstream of the step. The length of this zone (i.e. the distance between the step and the reattachment of the separation streamline) increases with the Reynolds number based on the step-height and the ratio between the step-height and the height of the duct, but also depends on the shape of

the velocity profile at the step. Furthermore, for increasing Reynolds number, flow separation is observed at the wall opposite to the step at the same axial location where reattachment occurs at the step-side wall. Numerical predictions of steady laminar flow over backward-facing steps are reported by Atkins et al. (1980), Hutton (1980), Thomas et al. (1981), Armaly et al. (1883) and Ecer et al. (1983) and generally a good agreement with the experiments was found as long as the flow remains laminar. Steady state numerical approximations of the laminar flow over a square step are reported by Leone and Gresho (1981) and Gresho and Lee (1981).

At higher Reynolds number, transition to turbulence at reattachment is observed (Goldstein et al. (1970), Sinha et al (1981), Durst and Tropea (1982) and Armaly et al. (1983)). Goldstein (1970) derived two criteria that must hold simultaneously for laminar flow. The Reynolds number based on the step-height must be less than 520 and the ratio of the displacement boundary layer thickness at the step to the step height must be greater than 0.4 (i.e. $(1/h)_o\int^{\delta}(1-u/u_m)dy > 0.4$, with h the step height, δ the boundary layer thickness, u the axial velocity, u_m the maximal axial velocity and y the cross-sectional direction). Assuming the flow to be fully developed at the step, the displacement thickness amounts to D/6h, so that for steady flow over a backward facing step no transition to turbulence is expected as long as $h<0.4D$ and $Re_h<520$. In this study, stenoses are considered with h=0.25D for a flow with $Re_h<200$ and thus no turbulence is expected as far as the rough estimate above based on the steady fully developed flow over a backward facing step holds. Particularly the assumption of fully developed flow does not hold for the flow over a step (i.e. a converging and diverging duct) and in virtue of Goldsteins second criterion transition to turbulence is expected at lower Reynold numbers with respect to backward-facing steps. The steady flow in ducts with local constrictions has been studied experimentally by Forrester and Young (1970), Azuma and Fukushima (1976), Yongchareon and Young (1979), D'Luna et al. (1982) and Ahmed and Giddens (1983[a,b]). From these studies it is known that poststenotic flow instabilities and turbulence may develop for increasing Reynolds number and increasing stenotic area reduction. The steady flow through an axisymmetric stenosis (following a cosine curve) with 25% area reduction, however, remains laminar and stable

for Reynold numbers, based on the diameter of the vessel, up to 1000 (Ahmed and Giddens, 1983[a,b]). On the other hand, the flow over step-like stenoses is less stable than that over a smooth constriction (Yongchareon and Young, 1979), so instabilities can be expected at lower Reynolds numbers.

Even more complicated is the unsteady flow over a step. Experimental studies of Azuma and Fukushima (1976), Khalifa and Giddens (1978,1981) and Yongchareon and Young (1979), show that under unsteady flow conditions poststenotic development of instabilities and turbulence may occur depending on the shape and size of the stenosis, the Reynoldsnumber, the time dependence of te flow rate and the frequency parameter $\alpha=D\sqrt{(2\pi f/\nu)}$, with f the frequency of the flow period and ν the kinematic viscosity). The studies referred to above deal with rather large Reynolds numbers based on aortic flow and with rather severe stenoses. Although not negligible beforehand, less important flow disturbances are expected for the flow in the carotid artery. Khalifa and Giddens (1981) observed in a 25% smooth stenosis geometry under pulsatile flow conditions ($500<Re<2400$) that all flow disturbances are periodic and no transition to turbulence occurs, so that no turbulence is expected in the range of the Reynolds number used in this study ($200<Re<800$). Numerical studies of unsteady flow through stenoses deal with laminar and stable flow in geometries with axial symmetry (Daly, 1976, Bordon et al., 1978, Padmanabhan, 1980 and Wille and Walløe, 1981), or with transition to a steady state in two-dimensional asymmetric square step models (Bercovier and Engelman (1979), Hughes et al. (1979) and Yang and Alturi (1984)). From these studies it follows that the reversed flow region downstream of the step strongly varies with time and exhibits properties which deviate significantly from a quasi-static approach. As far as is known, no numerical analyses of unsteady laminar flow in asymmetric step geometries are reported yet.

In section 3.2 the steady flow over a step is dealt with. In order to optimize the numerical method with respect to its practical application, the emphasis lies on the incorporation of the in- and outflow boundary conditions and the influence of the coarseness of the finite element mesh applied on the velocity and pressure distribution obtained. In order to determine whether the solution is influenced by the sharp corners of the square step, also the steady

flow over a step with rounded corners is calculated. Next the influence of the Reynolds number on the calculated velocity field is analysed for Reynolds numbers lying in the range from 100 to 800. In order to validate the numerical method and to examine whether the flow which is modelled remains laminar, laser-Doppler measurements in an experimental model with steady flow over a square step have been performed. Since flow instabilities are observed in the experiments, an attempt is made to simulate these instabilities by solving the instationary Navier-Stokes equations with steady and slightly perturbed boundary conditions.

In section 3.3 the analysis of a time-dependent pulsatile flow over a square step is described. First the fully developed flow between two flat plates, on which the (physiological) flow rate function as obtained from the study of Ku (1984) is imposed, is calculated. Next, the flow over a step is analysed using the fully developed flow as inflow condition. Also here the numerical approximation is validated experimentally. For a pulsating sinusoidal flow, with non-zero mean, over a square step, calculations are compared with results of laser-Doppler measurements. Special attention is paid to the development and break-down of reversed flow regions downstream the step at both the step-side wall and the non-step-side wall.

The analyses of the steady and unsteady flow over a square step will be discussed separately in sections 3.2.4 and 3.3.5, respectively.

3.2. Steady flow over a step.

3.2.1. Introduction.

From the study of Leone and Gresho (1981) and Gresho and Lee (1981) it is known that spurious in- and outlet wiggles in the velocity can occur depending on the in- and outflow boundary conditions and the coarseness of the mesh near the step. With regard to the inlet wiggles they distinguished two situations. For relative low Reynolds number flow they suggested to use a fully developed parabolic velocity profile as inlet condition to avoid a leading edge singularity as, for instance, introduced by a uniform inlet flow (u_n=1,u_t=0). For advection dominated flows the cause had to be sought

in too coarse a mesh near the step, unable to capture the steep velocity gradient. A local mesh refinement then is advised by them to be the best way to overcome these inlet wiggles. The outflow condition may also lead to numerical oscillations. As outflow condition would be usable a fully developed flow condition (σ_n=0, u_t=0) at a location far from the step. However, in practice this leads to the introduction of many degrees of freedom in a region that is not of interest. On the other hand, application of this outflow condition at locations which are too short downstream the step, may cause outlet wiggles. A way to overcome these wiggles is to use a less restrictive stress-free condition (σ_n=0,σ_t=0) (Leone and Gresho, 1981).

To evaluate the possibility of wiggles in the flow problem considered here and on the other hand to optimize the calculation procedure with respect to its practical application, as a preparation for the more complicated flow problems described in chapters 4 and 5, first several numerical tests have been performed. So, in section 3.2.2 the influence of the stress-free outflow condition, which is incompatible with fully developed flow, is described. Furthermore, the influence of the coarseness of the mesh and the shape of the inflow velocity profile is analysed. To indicate whether the velocity and pressure fields are strongly influenced by the sharp corners of the step, the results are compared with the results of calculations of the flow over a rounded step. Also, the influence of the Reynolds number on the velocity and pressure distributions is analysed.

Finally, in section 3.2.3 the numerical results are compared to experimental data and discussed in section 3.2.4.

3.2.2. Influence of boundary conditions, mesh-size, step geometry and Reynolds number.

Influence of the outflow boundary conditions.

For the numerical tests the geometry and element distribution as shown in Fig. 3.1 are used. The height (D) of the channel is 4h and at 9h from the inlet a step is present with a height and length of 1h. The Reynolds number based on the height of the channel is 400. At the inlet a fully developed velocity profile (u_n=parabolic,u_t=0) was assumed. No slip boundary conditions (u_n=0,u_t=0) were used at the

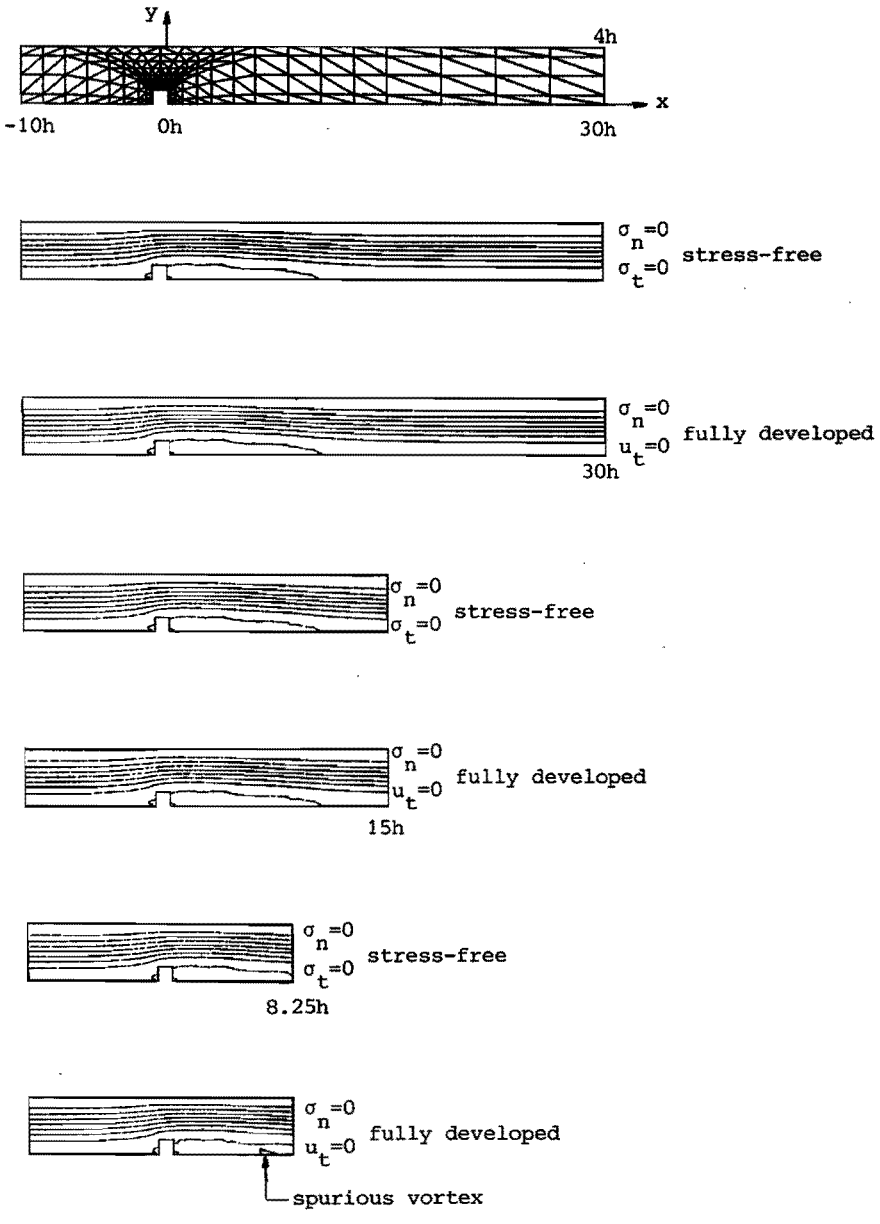

Fig. 3.1 : **Element distribution (272 elements, 609 nodes) and streamlines for different channel lengths and outflow boundary conditions for the steady flow over a square step (Re=400).**

upper and lower boundaries. To analyse the influence of the outflow boundary condition on the upstream flow field, the outflow condition was prescribed at x=30h, x=15h and x=8.25h. As a guideline for the length of the longest channel, half the entrance length for fully developed channel flow (L=0.04*Re*D, Schlichting,1979) was chosen. At these three outflow locations stress-free (σ_n=0,σ_t=0) as well as the more restrictive fully-developed outflow condition (σ_n=0,u_t=0) were applied.

In Fig. 3.1 the streamline plots are given for the three different channel lengths; they show a large downstream eddy and a relative small upstream eddy. A reattachment length, defined by the intersection of the dividing streamline with the lower boundary, of about 10.6h is found for both the stress-free and the fully-developed outflow conditions. Even for the shortest channel, the different outflow conditions do not seem to have much influence on the streamline patterns although a small spurious vortex downstream of the step is found when the fully-developed outflow condition is used.

More quantitative information about the influence of the outflow conditions can be obtained from the axial and cross-sectional velocity profiles for the cross-section x=3h, where the reversed flow region reaches about its maximal cross-sectional extension (see Fig.3.2). The computational results in case of the stress-free outflow condition are given in Figs. 3.2a and 3.2c, whereas the results for the fully developed outflow condition are given in Figs. 3.2b and 3.2d. Here the circles, triangles and asterisks refer to the results for the long, intermediate long and short channel, respectively. The computation with the stress-free outflow condition in the longest channel is used as reference situation and is given in solid lines in all graphs. From the axial velocity profiles (Figs. 3.2a and 3.2b) it is observed that for the long channel the applied outflow condition is indifferent. The computations with the stress-free outflow conditions (Fig. 3.2a) do not show any influence of the channel-length upon the axial velocity profiles, even if the outflow is located upstream the reattachment point of the eddy. Better visible differences are found in the profiles of the velocity in cross-sectional direction (Figs. 3.2c and 3.2d). Outside the recirculation area (y>1.1h) this velocity component is negative, in other words the flow is directed to the step-side wall of the channel. In case of the

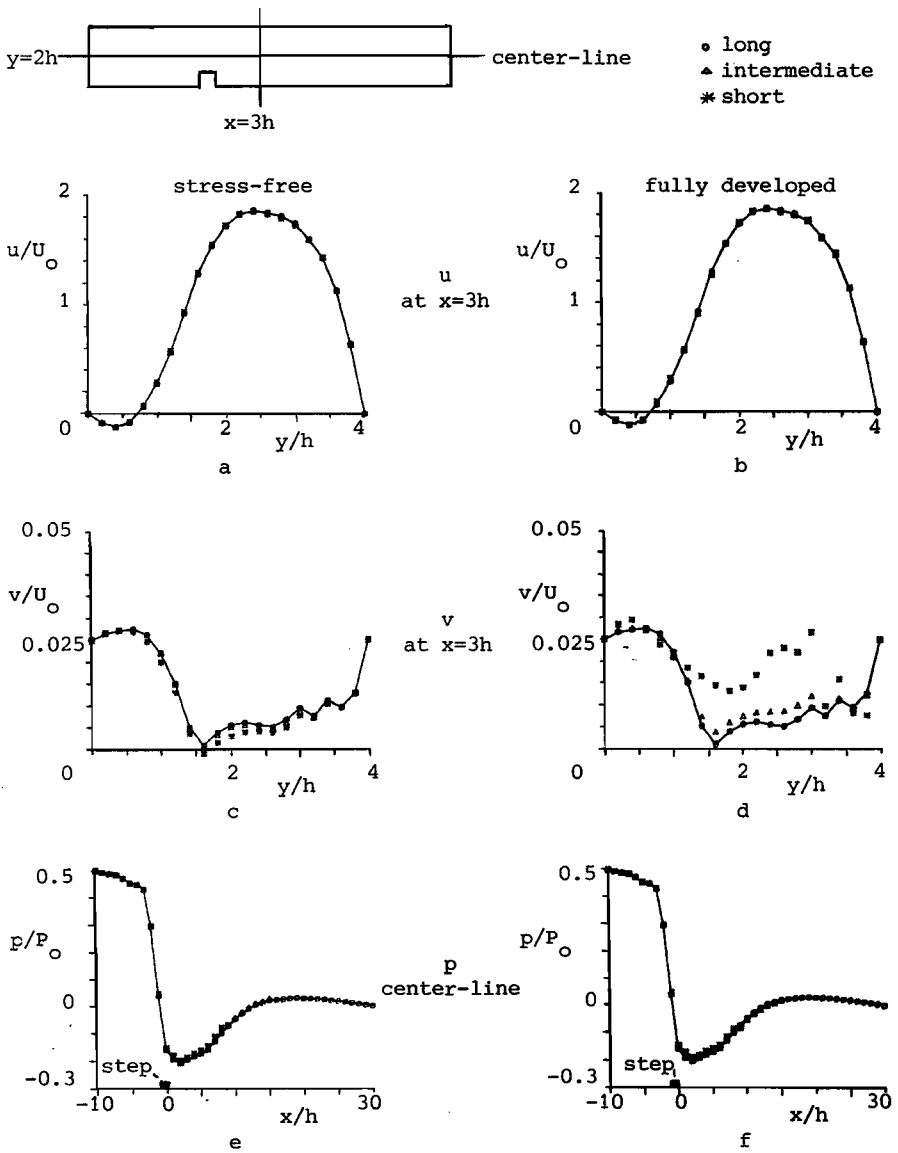

Fig. 3.2 : Influence of the outflow boundary conditions for the steady flow over a square step (Re=400) :
Axial and cross-sectional velocity profiles at cross-section x=3h and centerline pressure values as calculated with a long, intermediate long and short channel for stress-free and fully developed outflow conditions.

shortest channel combined with fully developed (unidirectional) outflow conditions, this velocity component is then underestimated significantly. In Figs. 3.2e and 3.2f the pressure is given as a function of the axial co-ordinate for locations on the centerline (y=2h) of the channel for both outflow conditions applied. These centerline pressure values show a relatively good agreement for all situations, even the large pressure drop at the step location and the outflow pressure gradient differs little for both situations.

Influence of the coarseness of the mesh.

To examine the influence of the mesh coarseness on the approximation of the velocity and pressure field, three different element distributions were generated (see Fig. 3.3a). The calculations were performed assuming stress-free outflow conditions while at the inlet a fully developed flow was prescribed. The Reynolds number of the flow is 400 and the length of the channel is 15h.

The calculated streamline distributions are given in Fig. 3.3b. In agreement with the observations made by Leone and Gresho (1981), an underestimation of the length of the recirculation zone and a tendency of a spurious splitting up of this zone can be observed for

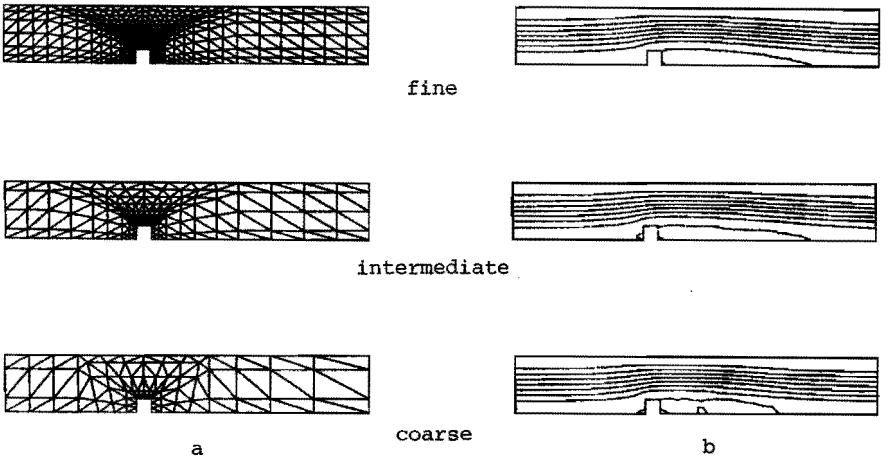

Fig. 3.3 : Influence of the coarseness of the mesh on the steady flow over as square step (Re=400) : a) Finite element meshes as used to analyse the influence of the coarseness of the mesh.
b) Streamlines for the different meshes.

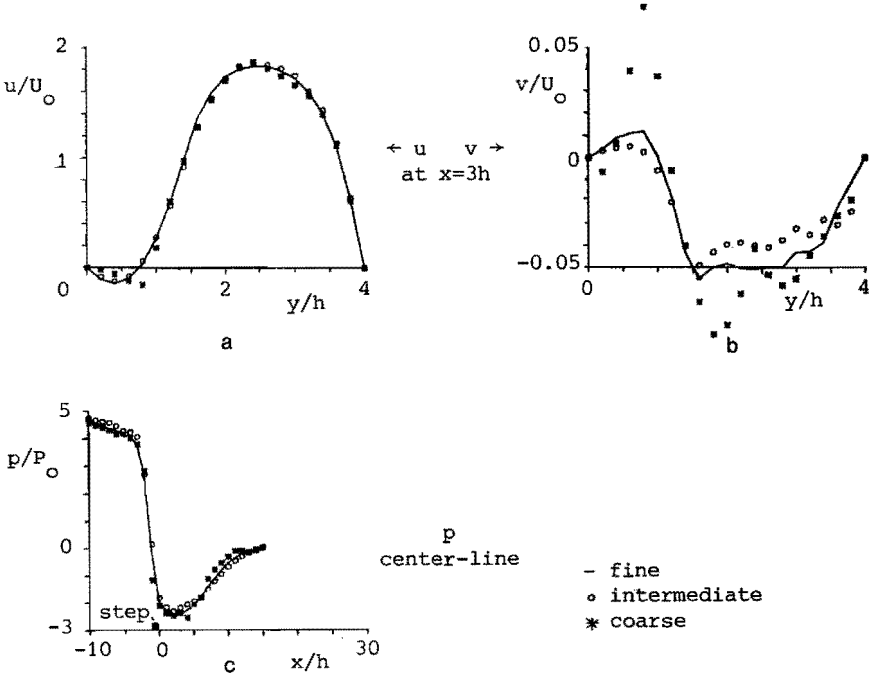

Fig. 3.4 : Influence of the coarseness of the mesh on the steady flow over a square step (Re=400) :
Axial and cross-sectional velocity profiles at cross-section x=3h and centerline pressures, for the fine, intermediate fine and coarse mesh.

the coarsest mesh. Besides, it is noted that the small upstream eddy disappears when the finest mesh is applied.

A more quantitative impression of the influence of the coarseness of the mesh is obtained from the velocity profiles at the cross-section x=3h and from the centerline pressure values (Fig. 3.4). In Fig. 3.4a the axial velocity profiles are given for the three meshes. The calculations with the finest mesh, indicated by the solid line, show a smooth axial velocity profile with a reversed flow region with a width of about .75h. The axial velocity profile as obtained with the intermediate fine mesh (dots in Fig. 3.4a) is in good agreement with these results. The coarse mesh, however, results in an under-

estimation of the magnitude of the reversed flow and an overestimation of the width of the reverse flow region. As observable from Fig. 3.4b, the cross-sectional component of the velocity is even more sensitive to the coarseness of the mesh. Large differences with respect to the fine mesh are found for the coarse mesh (asterisks) and large gradients of the cross-sectional component of the velocity occur. Although not negligible, these differences are significantly smaller when the intermediate fine mesh (dots) is applied. Besides, only slight influence of the coarseness of the mesh is found on the centerline pressure distributions (see Fig. 3.4c).

Influence of the inflow velocity profile.

Since the imposed inflow condition in numerical models of practical flow configurations is mostly based on either physical experience or experimental information, it is of importance to have an idea of the influence of the inflow condition on the calculated velocity and pressure distribution downstream. Here two inflow conditions will be evaluated for the problem of a steady flow over a step: a fully developed parabolic axial velocity profile and a uniform axial velocity profile, both combined with zero cross-sectional velocity. The Reynolds number is 400, stress-free outflow conditions were applied and the finest mesh shown in Fig. 3.3a was used. The inlet conditions are prescribed at x=-9h and the outlet conditions at x=15h.

In Fig. 3.5 the axial and cross-sectional velocity profiles at the cross-section x=3h are given. The solid lines represent the profiles as calculated with a parabolic axial inlet profile, whereas the dots represent the profiles for a uniform axial inlet profile. For both the axial and cross-sectional velocity components only slight differences are found between both cases. The differences are mainly visible in a more flattened axial velocity profile at the centre of the channel in case of the uniform inflow condition. The reversed flow at the lower wall shows for both cases a similar behaviour for both the axial and the cross-sectional velocity components. From Fig. 3.5c, where the centerline pressure values are given

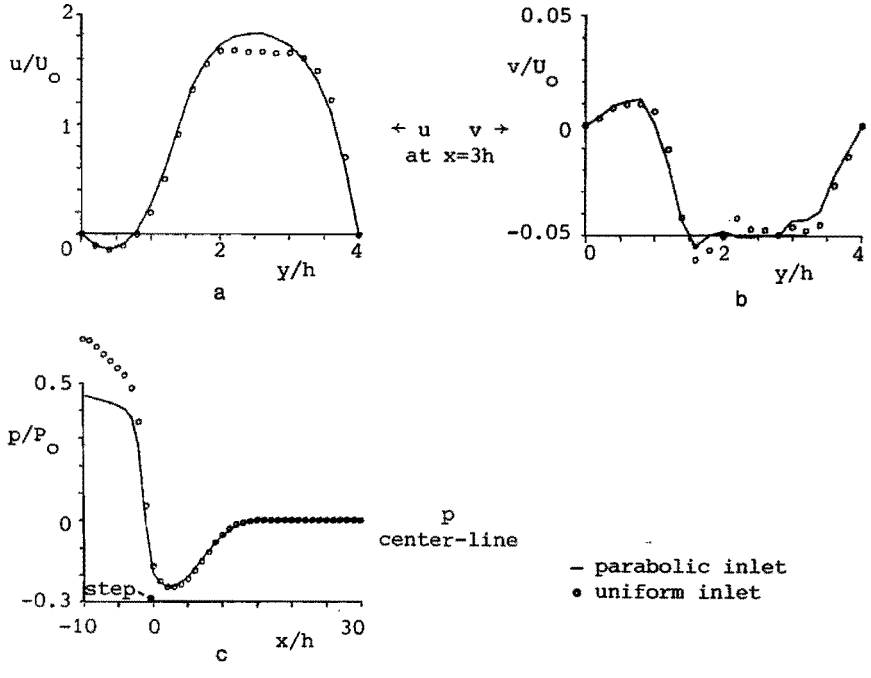

Fig. 3.5 : Influence of the inflow velocity profile on the steady flow over a square step (Re=400) :
Axial and cross-sectional velocity profiles at cross-section x=3h and centerline pressures, for the parabolic and uniform inlet velocity profiles.

for both inlet conditions, the most striking difference in the pressure approximation is found to be the larger pressure drop upstream the step for the uniform inflow condition. Also here a quite similar behaviour is found downstream the step location.

Influence of the step geometry.

The geometrical modelling of a stenosis with a square step is rather arbitrary and obviously not in accordance with the situation in vivo. In order to obtain an idea if, in particular, the sharp corners of the square step give rise to large differences in comparison with, for instance, rounded corners, also a computation in a

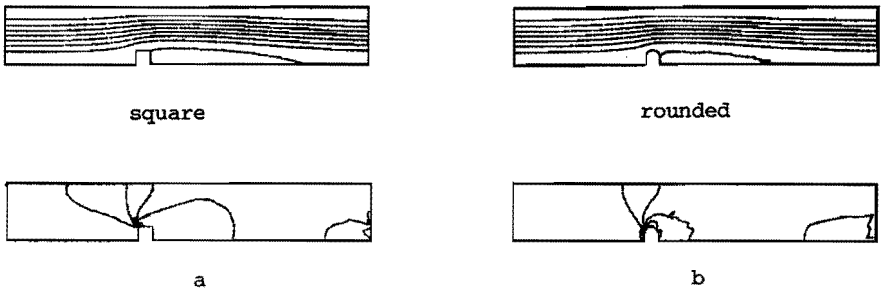

Fig. 3.6 : Influence of the step geometry on the steady flow over a square step (Re=400) :
Streamlines and isobars for the flow over a square and a rounded step.

geometry with a rounded step (see Fig. 3.6) was performed. At the inlet a parabolic axial (and zero cross-sectional) velocity was described and at the outlet stress-free outstream conditions were used. The Reynolds number amounts to 400, the length of the channel downstream the step is 15h and the finest mesh shown in Fig. 3.3a was used.

In Fig. 3.6 the streamlines and the isobars are given for the square as well as the rounded step configuration. As indicated by the streamlines, the boundary layer in the rounded step configuration separates closer to the wall of the channel. This results in a smaller recirculation zone in both the axial and the cross-sectional directions, and in consequence, in a lower pressure drop over the step. The pressure maximum at the proximal side of the step and the pressure minimum at the upper side of the step, as visible in the isobars are spread in case of the rounded step configuration but still exhibit the same characteristics as in the case of the square step. These observations are quantified in Fig. 3.7, where the axial and cross-sectional velocity profiles at x=3h and the centerline pressures are given for the square step (solid lines) and the rounded step (dots) geometries. For the rounded step the reversed flow velocities are found to be lower and restricted to a smaller region in

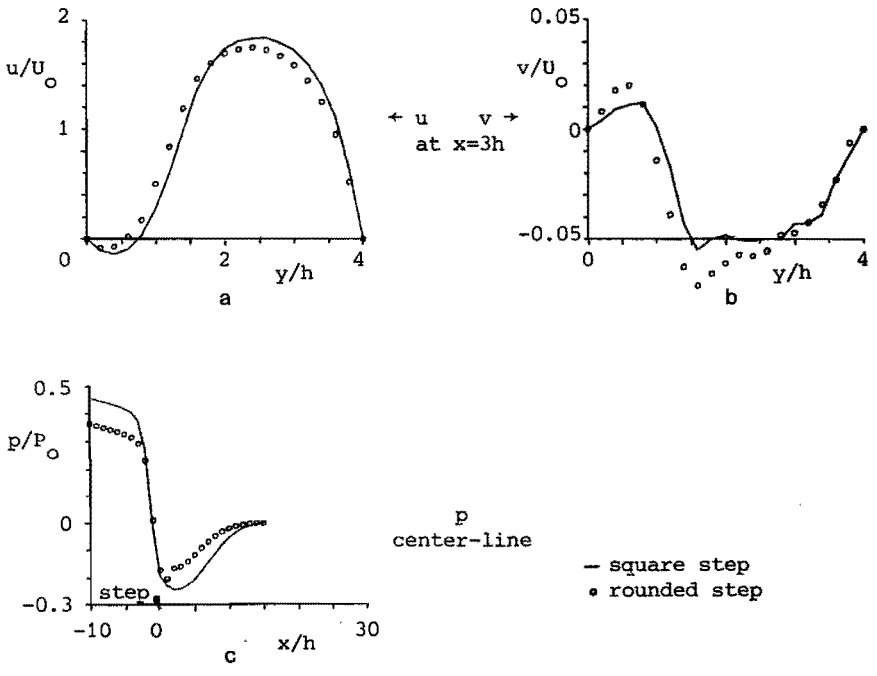

Fig. 3.7 : Influence of the step geometry on the steady flow over a square step (Re=400) :
Axial and cross-sectional velocity profiles at cross-section x=3h and centerline pressures, for the flow over a square and rounded step.

cross-sectional direction. Nearly similar profiles of the cross-sectional velocity component are found. The resulting overall pressure drop is smaller for the rounded step configuration.

Influence of the Reynolds number.

The physiological range of the Reynolds number in the common carotid artery is from Re=200 to Re=800. To get an impression whether the physiological (unsteady) flow (see section 3.3.3) can be modelled by a quasi static flow, the influence of the Reynolds number on the velocity and pressure distribution was analysed. Again a parabolic axial velocity profile together with zero cross-sectional velocity

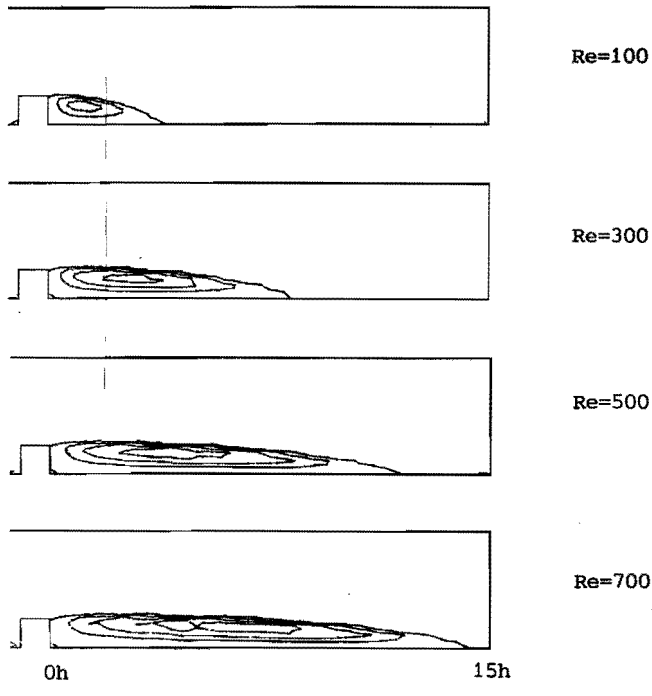

Fig. 3.8 : Influence of the Reynolds number on the steady flow over a square step :
Streamlines in the recirculation zones of the flow over a square step for different Reynolds numbers.

was used at the inlet and stress-free outflow conditions were assumed. The length of the outflow channel is 15h. Since the stress-free outflow conditions exhibit only little influence on the velocity distribution upstream, it is assumed that this channel length is sufficient for all Reynolds numbers used.

In Fig. 3.8 the streamline plots of the recirculation zones are given for Re=100, 300, 500 and 700 respectively. The axial extent of this zone increases almost proportional to the Reynolds number. Hence, a suitable parameter to describe the flow characteristics as a function of the Reynolds number is the length of the reversed flow region. This parameter was determined from the axial velocity profiles at several cross-sections of the channel and obtained by linear

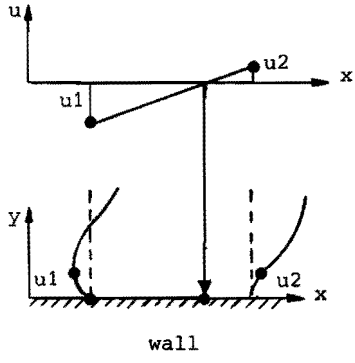

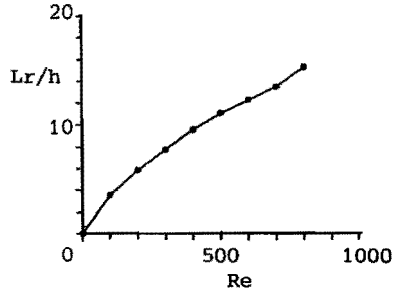

Fig. 3.9

Fig. 3.10

Fig. 3.9 : Determination of the length of the reversed flow region from the axial velocity profiles.

Fig. 3.10 : Length of the reversed flow region of the steady flow over a square step as a function of the Reynolds number.

interpolation using the velocity profiles at two successive cross-sections, one on which reversed flow and one on which forward flow was found near the wall (see Fig. 3.9). Note that at the downstream face of the step, the width of the reversed flow region was assumed to be equal to h/2. In Fig. 3.10, the length of the reversed flow region is given as a function of the Reynolds number. In accordance with the reattachment lengths, an almost linear relationship is found between the length of the reversed flow region and the Reynolds number of the flow.

3.2.3. Experimental validation.

To validate the finite element analyses as described in the previous subsection, a comparison is made with laser-Doppler measurements in an experimental model of the flow over a square step for one specific situation (Van de Vosse et al.,1985). In essence the experimental model consists of a channel with a rectangular cross-section with a height to width ratio of 1:4. A variable flow can be generated from which the axial velocities are measured with a one-component laser-Doppler equipment. Halfway the channel a step is present with a height equal to a quarter of the channel height. Care was taken to create a fully developed flow in height direction upstream the step. Axial velocity profiles in height-direction at various axial positions in the centerplane perpendicular to the width direction were determined for a steady flow with a Reynolds number equal to 660. To increase the measurement accuracy, the measurements were repeated 10 times and averaged. Furthermore, 95%-confidence intervals were calculated from a Student-t distribution. A more extended description of the experimental set-up and measurement procedure is given in appendix 3. Numerical approximation of the flow was performed with inflow conditions using the experimental data for the axial component and a zero cross-sectional component of the velocity at the inlet at 9h upstream the step. Stress-free outflow was assumed at 30h downstream the step.

The measured and calculated axial velocity profiles are presented in Fig. 3.11 for several cross-sections in the channel. The measured velocity profiles are indicated by dots representing the 95% confidence intervals. At a location of 9h upstream the step, the flow is found to be almost fully developed. The influence of the step is hardly noticable up to 2h upstream. A downstream reversed flow region is found with a length that amounts to about 13h. Also at the non-step-side wall of the channel, the flow tends to separate starting at the location where the above mentioned reversed flow region ends. Globally speaking the calculated velocity profiles (indicated by the solid lines) are similar to the experimental data. However, the reversed flow region as found in the experiments is larger, while also larger negative axial velocities are found there to occur. Relative large differences are found downstream the eddy, where the

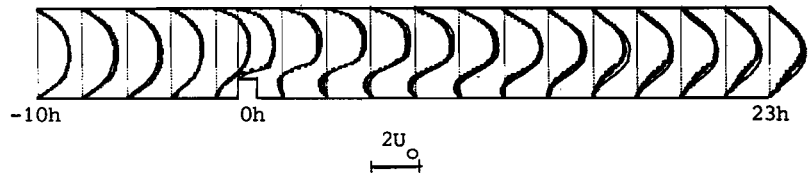

Fig. 3.11 : Experimental and numerical axial velocity profiles for the steady flow over a square step (Re=660).

axial velocities obtained from the experiments are smaller than the computed velocities.

The differences found between the experimental and numerical results are thought to be caused by two flow phenomena present in the experiments. In the first place, the flow in the experimental model is not fully two-dimensional but also three-dimensional effects are found. This is observable from the axial velocity profiles in Fig. 3.11 , where the integrals of the experimental velocity profiles over the different cross-sections are not constant and decrease for locations downstream the step. A second phenomenon present in the experiments, is the occurrence of spatial flow instabilities downstream the step. In Fig. 3.12 the measured axial velocities at several axial locations downstream the step at y=h, are plotted as a function of time. At axial locations up to 7h, the fluctuations are small and random. From the locations 9h to 21h, the amplitude of the fluctuations increases considerably and a mean frequency of about 0.25Hz is found. This corresponds to a Strouhal number, defined as $Sr=fh/U_0$, of about 0.125. A possible explanation for these flow instabilities lies in the shape of the velocity profiles near the reversed flow region. These profiles feature points of inflection, from which it is known (Schlichting,1979) that they are connected with the so-called Tollmien-Schlichting waves.

Since spatial flow instabilities are described by the unsteady Navier-Stokes equations, also an attempt was made to simulate the instabilities found in the experiments, by solving the same problem with the time dependent solution procedure described in chapter 2. The time was made dimensionless with a characteristic time $\tau=h/U_0=1$. First, the transition of the flow starting from rest was simulated.

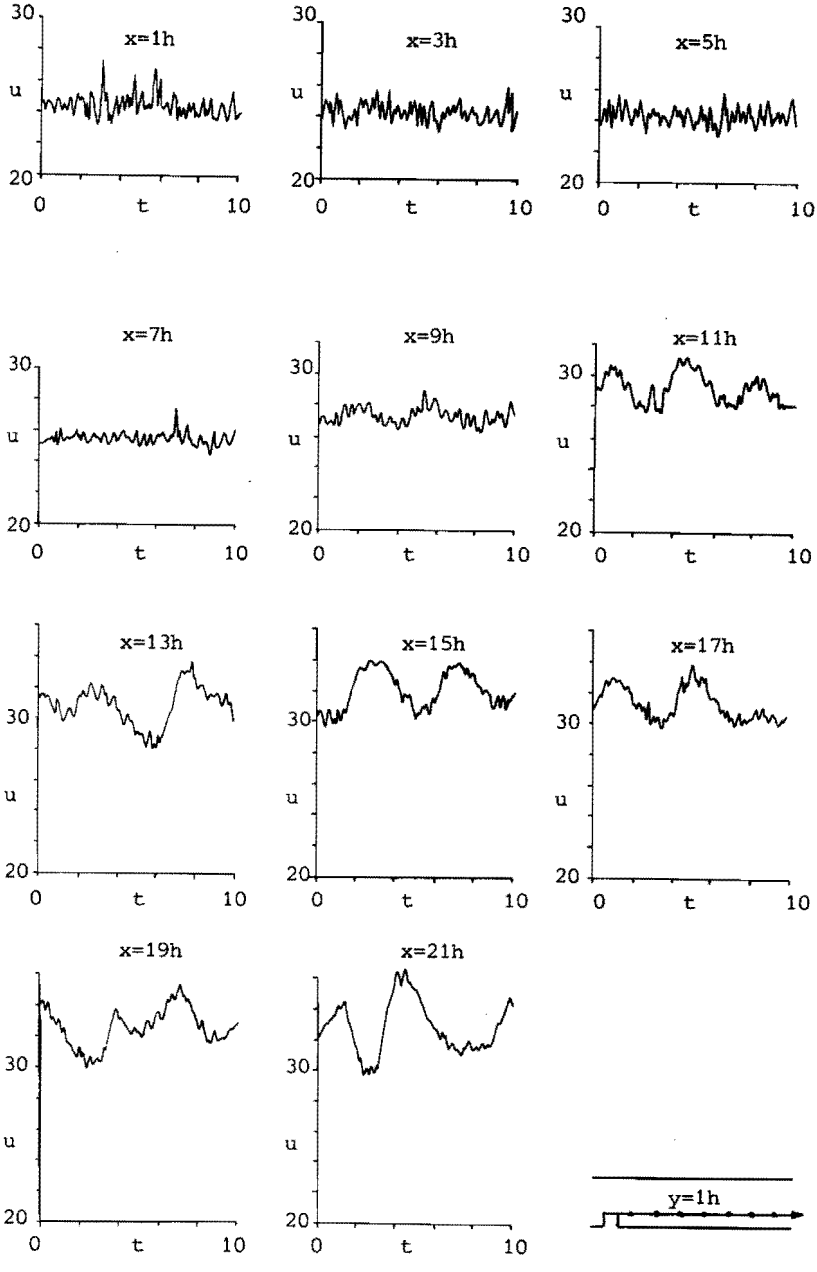

Fig. 3.12 : Measured axial velocity (arbitrary units) as a function of time for several locations on the axis y=1h for the flow over a square step (Re=660).

After 2 Euler implicit timesteps to damp the oscillations related to the steep jump in the flow induced by the initial value, 118 Crank-Nicolson steps with a timestep $\Delta t/\tau=0.5$ were performed. The solution converges only very slowly to a steady state, which is not yet reached after 120 timesteps ($t/\tau=60$). No spontaneous oscillatory behaviour of the flow was found. Similar to the triggering of the vortex shedding behind a circular cylinder (chapter 2), the cross-sectional velocity component of the step was set to a value of $0.1U_0$ during one timestep starting from the steady state solution of the problem. In Fig.3.13a, the streamfunction contours are given for $t/\tau=0$, 12, 24, 36, 48 and 60. The distortion at $t/\tau=0.5$ induces a temporal splitting up of the large eddy downstream the step and the formation of a small eddy at the opposite side of the channel. At

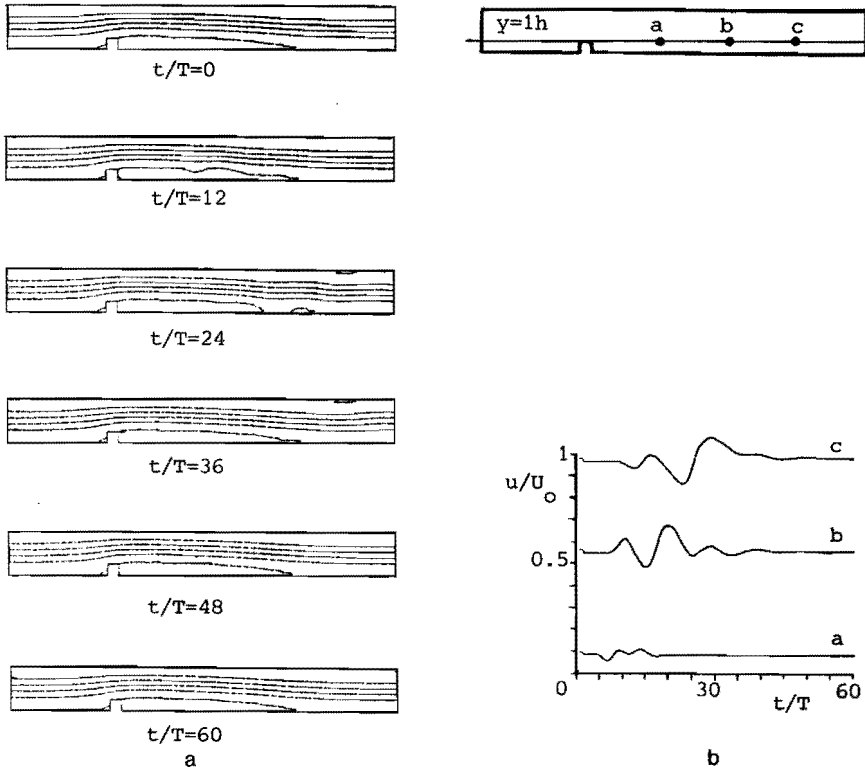

Fig. 3.13 : Time dependent solution of the flow over a square step with a distortion at t=0.5T for Re=800 : a) Streamfunction contours for t=0, 12, 24, 36, 48 and 60. b) Calculated axial velocity component as a function of time in several points on the axis y=1h.

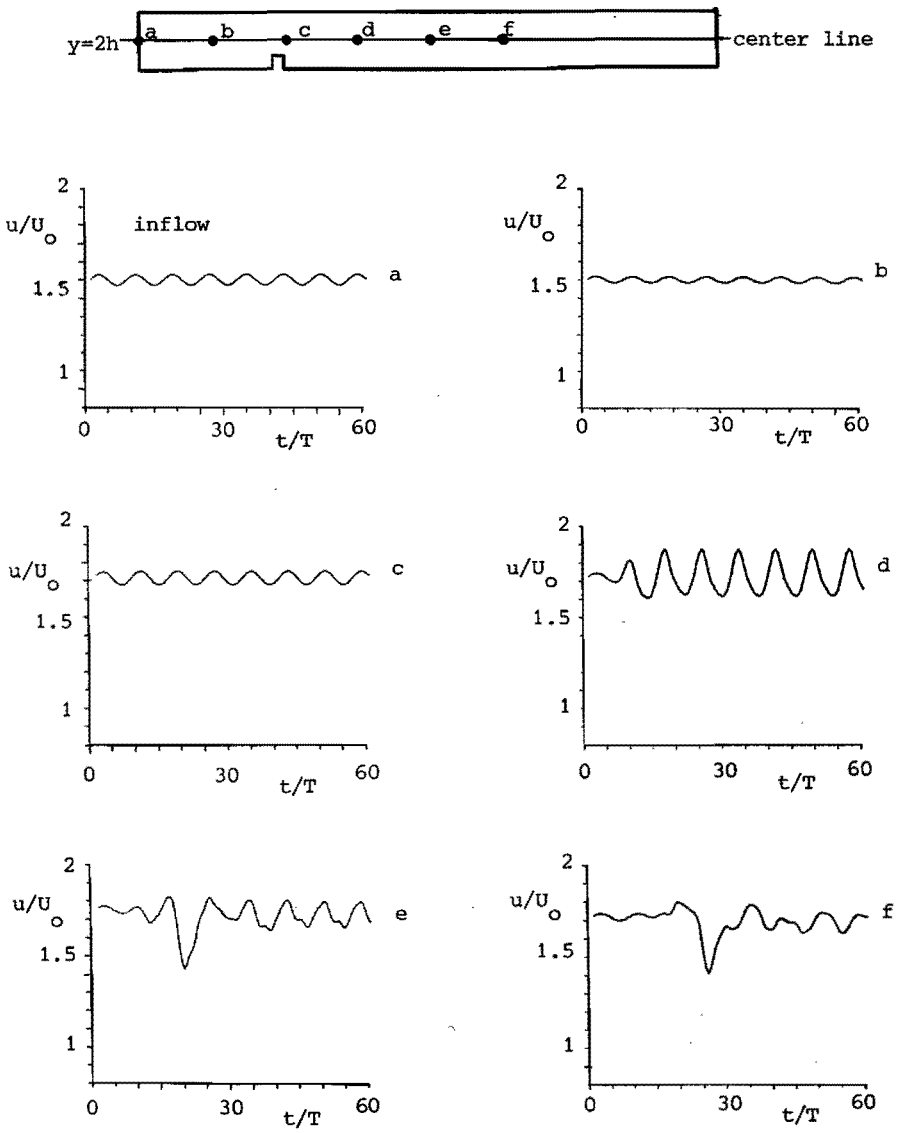

Fig. 3.14 : Flow over a square step with perturbed inflow condition ($u=U_o(1+0.02\sin(2\pi ft))$:
Calculated axial velocity component as a function of time in several points on the axis y=2h.

t/τ=60 (after 120 timesteps) the initial state is reached again. In Fig.3.13b, the axial velocity component at x=5, 10 and 15h is plotted as a function of time. They clearly do not show the periodic oscillations and spatial growth as found in the experiments. Therefore, also the sensitivity of the flow field for perturbations in the inflow velocity was determined. For this purpose, the parabolic inflow profile was multiplied by a factor $(1+0.02\sin 2\pi ft)$. The frequency f was taken to be equal to the frequency of the flow instabilities found in the experiments. After a transition from the steady state a periodic solution is now found. In Fig. 3.14, the axial velocity is given as a function of time for several locations at the centerline of the channel. The oscillations found have the same frequency as the perturbation of the inflow condition. A growth of the amplitude of the oscillations is found up to 5 step heights downstream the step, whereafter the amplitude decreases again and the distortion becomes less sinusoidal. If the frequency of the inflow perturbation is doubled, almost the same features are found. The amplitude of the oscillations is then found to be slightly smaller in magnitude and the frequency again is equal to the frequency of the inflow perturbation.

3.2.4. Discussion.

From the observations made from the computations for different outflow conditions and channel lengths in section 3.2.2, it is concluded that the stress-free outflow condition exhibits less upstream influence than the fully developed outflow condition. Furthermore it is found that at a Reynolds number of 400 an outflow channel length of 15h combined with stress-free outflow conditions gives a prediction of the velocity and pressure distribution which is not different from predictions obtained from calculations where a larger outflow channel is used. Stress-free outflow conditions seem therefore favourable especially when the outflow boundary is chosen at a relatively short location downstream the step. It is assumed that also for unsteady flow calculations being described in the next section, the stress-free outflow conditions have the same advantage. This is confirmed by the calculations of the vortex shedding behind a circular cylinder as described in the previous chapter, where the wave in

the streamlines leaves the computational domain without being influenced by the outflow boundary condition.

Assuming that the differences between the calculations with different mesh coarseness will be smaller when further mesh-refinement is applied, it is justified to state that the finest mesh is fine enough to approximate the steady velocity and pressure distribution for this step configuration.

Obviously the location of the step is so far from the inflow that only little influence of the inflow condition on the velocity and pressure distribution is found downstream the step. It is clear that this conclusion only holds if the inflow channel is long enough. It is disputable to extend this conclusion to the unsteady flow configuration. As observed from the calculations with slightly perturbed inflow conditions, these small perturbations may lead to relatively large disturbances downstream.

Although a more extensive study of the influence of the step geometry is needed to give a more solid conclusion, it can be assumed that, as far as the area reduction of the stenosis is chosen realistically, the modelling with a square step will not give significantly different characteristics as when geometrically more realistic models of the stenosis are used. For quantitative analyses, however, the geometry of the stenosis must be taken into account. Also with respect to the development of post-stenotic flow instabilities, the shape of the stenosis modelled is of interest (Yongchareon and Young, 1979).

Similar to the flow over backward facing steps (Goldstein et al., 1970, Denham and Patrick, 1974, Thomas et al., 1981, Durst and Tropea, 1982, Ecer et al., 1983 and Armaly et al., 1983) the length of the recirculation zone downstream the step is almost proportional to the Reynolds number, but is found to be about 3h larger in magnitude for the entire range of the Reynolds number. This larger reattachment length for the flow over a square step is probably a result of the direction of the velocity at the step location. In the backward-facing step geometry, the flow near the step location has an axial direction, whereas in case of the square step geometry used here, this flow is directed to the upper wall of the channel, due to the influence of the front face of the step, acting as an obstruction

in the flow. Besides, the reattachment length of the flow over backward-facing steps not only depends on the Reynolds number but also on the boundary layer thickness at the step (Goldstein et al., 1970), so a qualitative comparison of these reattachment lengths with those found in this study is difficult.

The length of the reversed flow region is thought to be a more suitable parameter to describe the flow downstream a step than the reattachment length. The former parameter keeps its physical meaning in case of unsteady flow analysis. This in contrast with the streamlines , and thereby the reattachment length, that are difficult to interpret for unsteady flow.

Furthermore, relatively good agreement exists between the axial velocity profiles obtained from the experiments and calculations. The flow instabilities that occur in the experiments show resemblance with the poststenotic flow disturbances with discrete oscillation frequency reported by Ahmed and Giddens (1983[a,b]) . Although a spatial (downstream) growth of inflow perturbations is predicted, the flow instabilities could not be simulated satisfactorily by solving the time dependent Navier-Stokes equations. It is not clear whether further mesh refinement and smaller timesteps are needed, or that the three-dimensional effects in the experiments have to be taken into account to simulate the flow instabilities with the finite element approximation.

3.3. Unsteady flow over a step.

3.3.1. Introduction.

In this section the unsteady flow over a square step is analysed. This is motivated by the fact that the physiological flow rate strongly varies with time (see chapter 1). The same geometry as in the steady flow analysis is used. In section 3.3.2 the fully developed unsteady flow in a straight channel is dealt with, scaled upon the situation in the common carotid artery. The dimensions and flow rate are adopted from the study of Ku (1983), who studied the physiological flow in an experimental model of the carotid artery bifurcation

(see also chapter 1). The results of the fully developed flow calculations then are used as inflow condition for the computation of the time-dependent flow over a square step, simulating a 25% stenosis in the common carotid artery (section 3.3.3). In particular the axial velocity profiles and the development of the induced reversed flow regions during the flow cycle are analysed and compared with data following from a quasi-static model of the flow. Finally in section 3.3.4, the unsteady flow calculations are validated with laser-Doppler measurements for the case of a sinusoidal flow with a static component .

3.3.2. Unsteady flow in a straight channel.

In order to obtain fully developed inflow conditions for the calculation of the unsteady flow in a stenosis model, the fully developed flow in a straight channel is computed. The geometry and flow rate were scaled on the flow in the common carotid artery (see chapter 1). The channel has a length of 7.5 times its height. The Reynolds number varies between 175 and 650 with a mean of 250, the frequency parameter α ($=D\sqrt{(2\pi/\nu T)}$) is equal to 4. Velocity profiles of the fully developed flow were computed by imposing a time dependent uniform axial velocity with zero cross-sectional velocity component corresponding with the flow given in Fig.3.15a. Fully developed flow conditions ($\sigma_n=0$, $u_t=0$) were used at the outflow of the channel. The calculations were performed with a Crank-Nicolson time integration with 100 timesteps per cardiac cycle and an implicit start of the first cycle.

Because of the relatively long period of almost steady flow in the diastolic phase, one cardiac cycle is sufficient to damp disturbances induced by the transition from the initial state.

The calculated outflow axial velocity profiles in the third cardiac cycle are given in Fig.3.15b for several instants of time (see Fig. 3.15a) in the systolic and diastolic phases of the flow. During the systolic acceleration phase, the axial velocity profile develops to a flattened profile. The maximum velocity value then is about three times larger than the maximum of the parabolic profile at the end of the diastolic phase. In systolic deceleration, a short period with reversed flow at the walls is observed. In the diastolic

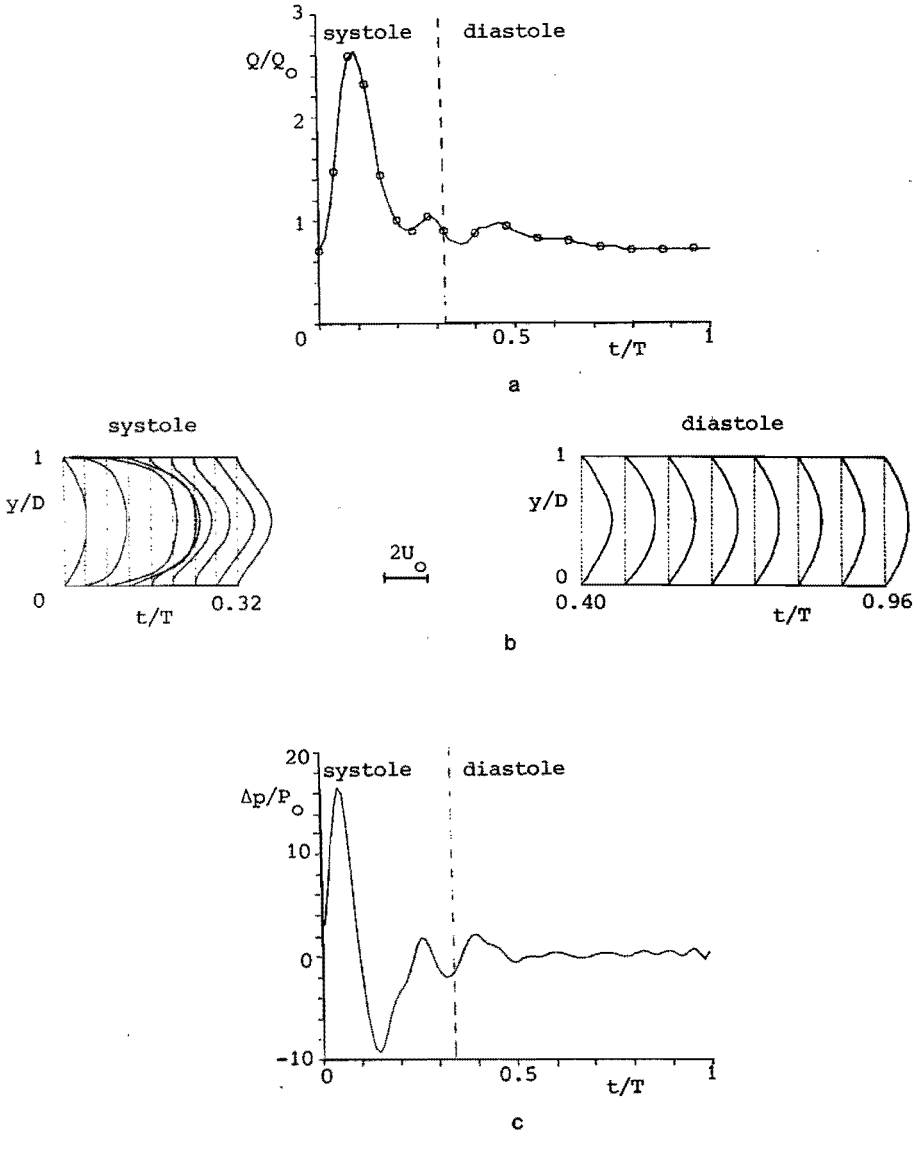

Fig. 3.15 : Fully developed physiological flow in a straight channel (175<Re<650, α=4) :
a) Flow as a function of time (Ku,1983).
b) Fully developed axial velocity profiles for systolic and diastolic flow phase, respectively.
c) Pressure drop over a channel with a length of 10 times its height.

phase, the axial velocity distribution slowly develops to a parabolic profile again. In Fig. 3.15c the pressure gradient at the outflow of the channel is given as a function of time. To enable a comparison with the calculations of the unsteady flow over a step (see next section) this pressure gradient is scaled such that it corresponds with the pressure drop over a channel with a length of 10 diameters. In agreement with the observations made by Womersley (1955), the systolic pressure gradient pulse precedes the flow pulse by about half the pulse time.

3.3.3. Unsteady flow over a square step.

The numerical two-dimensional stenosis model consists of a straight channel with a height of 4h and a length of 40h. The stenosis, modelled with a square step with a length and height of 1h, is located at 9 step heights from the inlet. The axial velocity profiles of the fully developed flow calculation described in the previous section, were used as inflow condition. Similar to the steady flow calculations, a stress-free outflow condition was used. The applied finite element mesh is given in Fig. 3.16. Since a more complicated velocity field with relatively large velocity gradients was expected, the mesh has been refined with respect to the steady flow calculations. Moreover, the outflow length has been enlarged with 10 step heights. Again a Crank-Nicolson time integration with 100 timesteps per cardiac cycle and an implicit start in the first calculated cycle was used.

In Fig.3.17 the calculated axial velocity profiles for several cross-sections of the channel are given at various instants of time in both the systolic and diastolic phases of the flow. During the systolic acceleration of the flow (t=0T - t=0.08T) a reversed flow region is formed downstream of the step and flattened axial velocity

Fig. 3.16 : Finite element mesh as used in the unsteady flow calculations (660 elements, 1445 nodes).

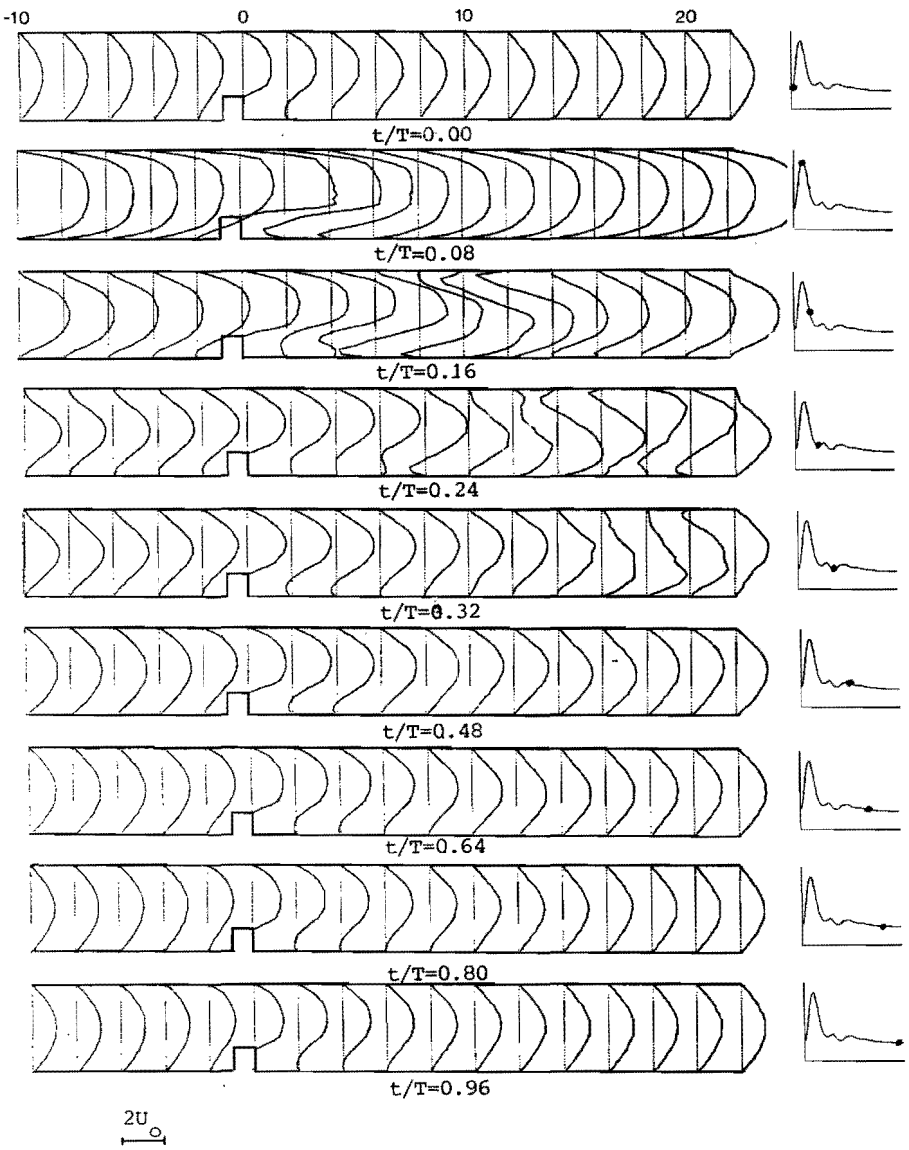

Fig. 3.17 : Axial velocity profiles at several times in both the systolic and diastolic phase of the unsteady flow (175<Re<650, α=4).

profiles are observed at all cross-sections. During the systolic deceleration (t=0.08T - t=0.32T) a complex flow field arises with reversed flow regions at both the step-side and non-step-side walls.

These regions move downstream and disappear at the end of the systolic phase. In the diastolic phase a gradual recovery to a steady flow takes place.

A more detailed picture of the appearance and behaviour of the reversed flow regions is given in Fig. 3.18. Here the axial locations of reversed flow (i.e. negative wall shear stress) at the step-side wall as well as the non-step-side wall are given as a function of time during the entire cardiac cycle. For clearness the flow curve is given at the top of this figure. From this figure it is observed that at the beginning of the systolic acceleration, only one reversed flow region, starting from the downstream face of the step, is present which has a length of about 5h. In the following this reversed flow region will be denoted as the primary step-side reversed flow region. During the onset of the systolic acceleration (t=0.01T), this region disappears completely after which it recovers again and grows to a length of about 7h at the end of the systolic acceleration. During the systolic deceleration the primary step-side reversed flow region grows in length and covers a small region with positive axial velocity. At the same time a primary non-step-side reversed flow region appears starting at about the same axial location as where the primary step-side reversed flow region ends (≈7h). Subsequently, both a secondary step-side and non-step-side reversed flow region appear, leading to the situation in which alternating reversed flow regions exist at both walls. During the onset of the diastolic phase all reversed flow regions except for the primary step-side region disappear. Another striking phenomenon at the end of the systolic phase and the onset of the diastolic phase is the splitting up of the primary step-side reversed flow region during the small flow accelerations. The most distal separated reversed flow regions then move downstream and disappear later on. At the same time the primary step-side reversed flow region recovers again.

The length of the step-side reversed flow region is also determined from the steady flow calculations given in section 3.3.3. Since this length appeared to be almost proportional to the Reynolds number, the quasi-static length curve in Fig. 3.18 follows the flow curve. This curve only matches the curve of the primary step-side reversed flow region at the end of the diastolic phase of the flow.

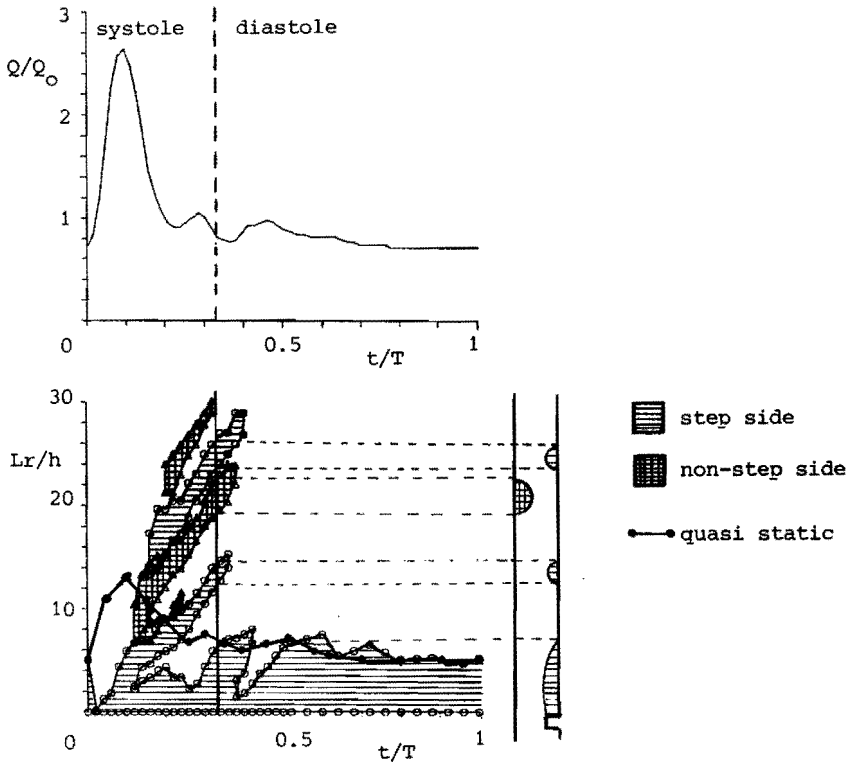

Fig. 3.18 : Zones with negative axial velocities at both the step-side and opposing-side wall as a function of time during one flow cycle of the unsteady flow over a square step ($175<Re<650$, $\alpha=4$).

This indicates that the instationary inertial effects induce a much more complicated flow field than expected from a quasi-static model.

Finally the pressure drop over the channel is given as a function of time during the cardiac cycle and compared with the pressure drop as obtained in a channel without a step (Fig. 3.19). No essential differences are found between both cases. Hence, the pressure drop fluctuations induced by the unsteady flow appear to be much more important than the pressure drop caused by the step. The latter seems to have only a local influence on the pressure distribution.

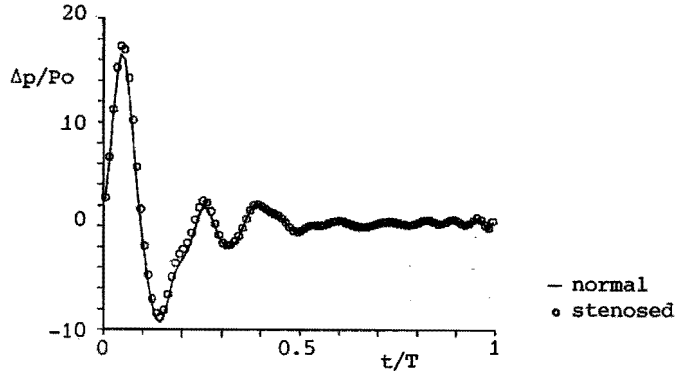

Fig. 3.19 : Pressure drop over a straight and stenosed channel as a function of time during one period of the unsteady flow (175<Re<650, α=4).

3.3.4.Experimental validation.

As in the steady flow analysis, a comparison is made with laser-Doppler measurements performed in an experimental model (Van de Vosse et al.,1985) to validate the finite element analysis. In Fig. 3.21a the flow as used in the experiments is given as a function of time for two flow cycles. This flow nearly is sinusoidal with a mean Reynolds number ($Re=U_0D/\nu$) of about 550 varying from about 200 up to 800. The cycle time T was taken to be such that the frequency parameter α ($=D\sqrt{(2\pi/\nu T)}$) amounts to about 16. This is 4 times larger than used in the calculations with the physiological flow rate in order to obtain a better adjustment with the systolic flow pulse. To increase the measurement accuracy, the experiments were repeated 10 times, from which after averaging, the 95% confidence intervals were determined. The computations were performed on the mesh of Fig. 3.16 with a Crank-Nicolson time integration with 70 timesteps per cycle period of the flow. The inflow velocity profiles in the computation were taken equal to the measured velocity profiles, whereas stress-free outflow conditions were applied.

In Fig. 3.20 the measured axial velocity profiles for several cross-sections are given. The 95%-confidence intervals are indicated with dots. The inlet profiles resemble qualitatively the profiles of

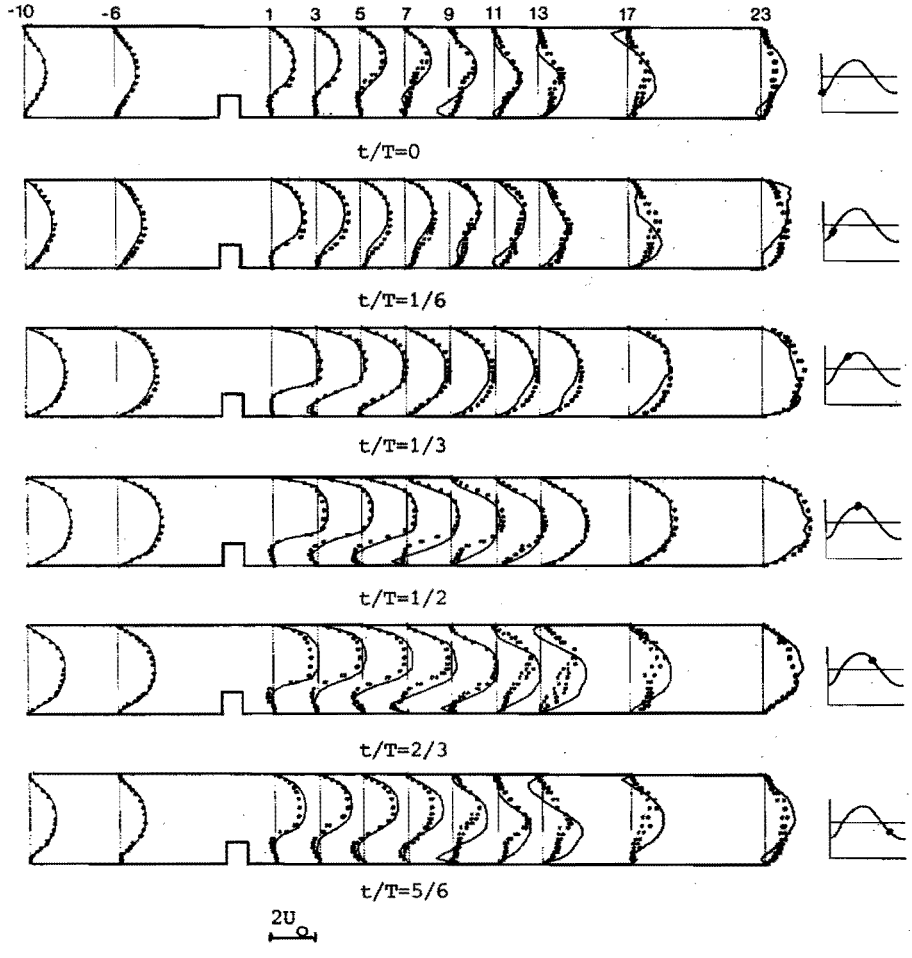

Fig. 3.20 : Axial velocity profiles at several times in both the acceleration and deceleration phase of the experimental flow over a square step (200<Re<800, α=16).

a fully developed oscillating flow between two flat plates (see chapter 2) superimposed to a steady parabolic profile. The suppressed steady component is so large that no reversed flow occurs at this site, but the phase-lag between the velocities near the wall and in the center of the channel illustrates the unsteady effect. At an axial location of 1h downstream the step, the reversed flow is almost stationary with in the deceleration phase a tendency to forward flow near the wall. The region of reversed flow moves slightly towards the

center of the channel in this period of time. At locations up to x=9h, the flow is characterized by a gradual growth and break-down of the step-side reversed flow region. At the non-step-side a reversed flow region is formed in the deceleration and resolved in the acceleration phase. At axial locations from 11h up to the outflow of the channel, a sudden change in the velocity profiles is found at the onset of the deceleration of the flow. This change is accompanied with a significant increase of the magnitude of the confidence intervals, pointing to flow instabilities. In the acceleration phase, the flow stabilizes again, resulting in smooth profiles with relatively small confidence intervals at the end of the acceleration. The profiles at the axial location 23h, show a recovery towards the developed profiles as measured at the inflow, except for the period of time at the end of the deceleration and the onset of the acceleration. Here the outflow profiles are disturbed as a result of the instabilities generated upstream. Furthermore, it is observed that at the onset of the acceleration, the total flow along the outflow cross-section has decreased with respect to the inflow, pointing to three-dimensional effects in the experimental model.

In Fig. 3.20, also the calculated velocity profiles are given. A relatively good agreement with the experiments is found during the entire flow cycle as far as axial locations up to 9h downstream the step are considered. Relatively large differences are found there and then where flow instabilities occur in the experiments.

For a more detailed comparison of the zones of reversed flow, in Fig. 3.21 the locations with negative axial velocities close to the walls are given as a function of time for both the experimental (Fig. 3.21b) and numerical (Fig. 3.21c) models. In the experiments a gradual increase of the primary step-side reversed flow region from about 2h at the onset of the acceleration to about 12h half-way the deceleration, is found. The same characteristic is found in the computations, although the length of the reversed flow region is smaller during the entire flow cycle. Half-way the deceleration of the flow a primary non-step-side reversed flow region is formed at about the same axial location where the primary step-side region ends. This non-step-side region resolves at the end of the deceleration phase of the flow. In the computations, this region is formed earlier in time and continues to exist for a longer period of time.

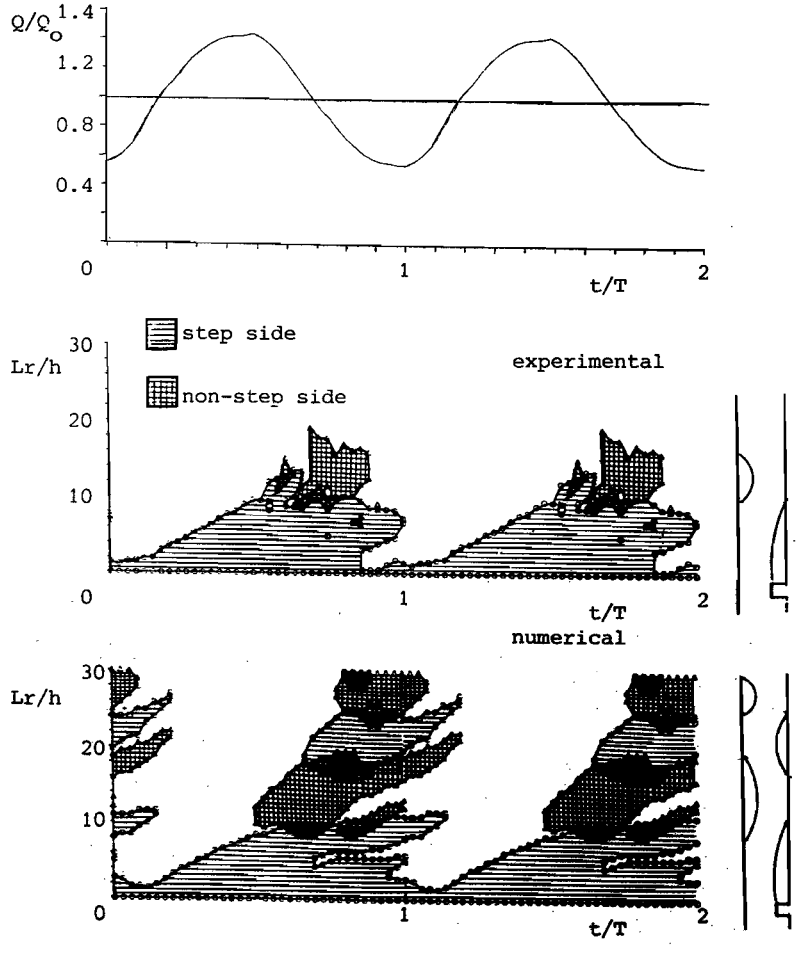

Fig. 3.21 : Zones with negative axial velocities at both the step-side and non-step-side wall as a function of time during two flow cycles of the experimental flow over a square step ($200<Re<800$, $\alpha=16$).

The secondary and even tertiary reversed flow regions, found during the deceleration phase of the flow in the numerical model, are not observed in the experiments, probably because of the flow instabilities and three-dimensional effects ocurring in that period of time and at those locations. Besides, the splitting-up of the primary

step-side reversed flow region is observed to start earlier in time in the computations than in the experiments.

Finally, it is remarked that the characteristics of the calculated pulsating flow are quite similar to those of the calculations with the physiological flow rate during the systolic phase (cf. Fig. 3.18 and Fig. 3.21).

3.3.5. Discussion.

Comparing the steady and unsteady analyses of the flow over a square step the following comments are made. In the steady flow case, an almost proportional relation is found between the length of the reversed flow region downstream of the step and the Reynolds number. This completely differs from the unsteady flow over a step which leads to a relatively complex flow field. Quasi-static modelling appeared then to be only valuable for the end of the diastolic phase. During the systolic acceleration, the reversed flow region downstream of the step grows gradually but is significantly smaller than expected from a quasi-static analysis. During the systolic deceleration this region splits up and a reversed flow region is formed at the non-step-side wall and subsequently secondary and even tertiary reversed flow regions are formed at both the step-side and non-step-side walls. These reversed flow regions disappear during the diastolic phase of the flow. Only the primary step-side reversed flow region remains to exist although it almost completely vanishes at the onset of the systolic acceleration, where the instationary inertia terms seem to dominate the advective terms.

Quite similar characteristics are found in the calculation with the experimental pulsatile flow curve. With respect to the comparison with the experimental data, the influence of the three-dimensionality and instabilities in the experiments are even more confusing than in the steady flow analysis. A qualitative agreement is found between the experiments and the calculations for both the primary step-side and non-step-side reversed flow regions. Discrepancy is found downstream from the regions where flow instabilities and three-dimensional effects occur in the experiments.

The regions with negative axial velocities (i.e. negative wall shear stresses) exhibit well definable characteristics during the

acceleration and deceleration phases of the flow and are suitable to qualify the flow downstream a stenosis. Therefore, they will also be used in the next section to describe the two-dimensional steady and unsteady flow characteristics in bifurcation models.

references.

- Ahmed S.A. and Giddens D.P.,'Velocity measurements in steady flow through axisymmetric stenoses at moderate Reynolds numbers.', J. Biomech., 16, p 505-516 (1983).
- Ahmed S.A. and Giddens D.P.,'Flow disturbance measurements through a constricted tube at moderate Reynolds numbers.', J. Biomech., 16, p 955-963 (1983).
- Armaly B.F., Durst F. Pereira J.C.F. and Schönung B.,'Experimental and theoretical investigation of backward-facing step flow.', J. Fluid Mech., 127, p 473-496 (1983).
- Atkins D.J., Maskell S.J. and Patrick M.A.,'Numerical prediction of separated flows.', Int. J. Num. Meth. Fluids , 15, p 129-144 (1980).
- Azuma T. and Fukushima T.,'Flow patterns in stenotic blood vessel models.', Biorheology, 13, p337-355 (1976).
- Bercovier M. and Engelman M.,'A finite element for the numerical solution of viscous incompressible flows.', J. Comp. Physics, 30, p 181-201 (1979).
- Bordon P., Chagneau F., Doffin J. and Ripert G.,'Theoretical and experimental study of vortices produced by an oscillating flow in stenoses - Application to vascular mechanics.', 1st Int. Conf. Mech. Medic. Biol., p VII 243-246 (1978).
- Daly B.J.,'A numerical study of pulsatile flow through stenosed canine femoral arteries.', J. Biomech., 9, p 465-475 (1976).
- Denham M.K. and Patrick M.A.,'Laminar flow over a downstream-facing step in a two-dimensional flow channel.', Trans. Instn Chem. Engrs, 52, p 361-367 (1974).
- D'Luna L.J., Newhouse V.L. and Giddens D.P.,'In vitro Doppler detection of axisymmetric stenoses from transverse velocity measurements.', J. Biomech., 15, p 647-660 (1982).

- Durst F. and Tropea C.,'Flows over two-dimensional backward-facing steps.' IUTAM symposium Marseille, Ed. Dumas R. and Fulachier L., Springer Verlag Berlin, p 41-52 (1983).
- Ecer A., Rout R.K. and Ward P.,'Investigation of solution of Navier-Stokes equations using a variational formulation.', Int. J. Num. Meth. Fluids, 3, p 23-31 (1983).
- Forrester J.H. and Young D.F., 'Flow through a converging-diverging tube and its implications in occlusive vascular disease I: Theoretical development.', J. Biomech., 3, p 297-305 (1970).
- Forrester J.H. and Young D.F., 'Flow through a converging-diverging tube and its implications in occlusive vascular disease II: Theoretical and experimental results and their implications.', J. Biomech., 3, p 307-316 (1970).
- Goldstein R.J., Eriksen V.L., Olson R.M. and Eckert E.R.G., 'Laminar separation, reattachment, and transition of the flow over a downstream-facing step.',Trans. ASME J. Basic. Eng., 92, p 732-741 (1970).
- Gresho P.M. and Lee R.L.,'Don't suppress the wiggles - they're telling you something!.' Comp. & Fluids, 9, p 223-253 (1981).
- Hughes T.J.R., Liu W.K. and Brooks A.,'Finite element analysis of incompressible flows by the penalty function formulation.', J. Comp. Physics, 30, p 1-60 (1979).
- Hutton A.G.,'Incompressible viscous flow modelling by the method of finite elements'. ,in: Numerical methods in applied fluid dynamics, ed. Hunt B., p 178-201, Academic Press (1980).
- Khalifa A.M.A. and Giddens D.P.,'Analysis of disorder in pulsatile flows with application to poststenotic blood velocity measurement in dogs.', J. Biomech., 11, p 129-141 (1978).
- Khalifa A.M.A. and Giddens D.P.,'Characterization and evolution of poststenotic flow disturbances.', J. Biomech., 14, p 279-296 (1981).
- Ku D.N.,'Hemodynamics and atherogenesis at the human carotid bifurcation'., Ph.D. Thesis, Georgia inst.techn. (1983).
- Leone J.M. and Gresho P.M.,'Finite element simulations of steady, two-dimensional, viscous incompressible flow over a step.', J. Comp. Phys., 41, p 167-191 (1981).
- Padmanabhan N.,'Mathematical model of arterial stenosis.', Med. & Biol. Eng. & Comput., 18, p 281-286 (1980).

- Pedley T.J.,'The fluidmechanics of large blood vessels.', Cambridge University press (1980).
- Reneman R.S., van Merode T., Hick P. and Hoeks A.P.G.,'Flow velocity patterns in and distensibility of the carotid artery bulb in subjects of various ages.', Circulation, 71, p 500-509 (1985).
- Schlichting H.,'Boundary layer theory.', McGraw-Hill Inc. (1979).
- Sinha S.N., Gupta A.K. and Oberai M.M.,'Laminar separating flow over backsteps and cavities part I: Backsteps.', AIAA Journal, 19, p 1527-1530 (1981).
- Thomas C.E., Morgan K. and Taylor C.,'A finite element analysis of flow over a backward facing step.' Comp. & Fluids, 9, p 265-278 (1981).
- Van de Vosse F.N., Vial F.H., Van Steenhoven A.A., Segal A. and Janssen J.D.,'A finite element and experimental analysis of steady and pulsating flow over a two-dimensional step.', In : Numerical methods in laminar and turbulent flow., p 515-526, Eds. Taylor C., Olson M.D., Gresho P.M. and Habashi W.G., Proc.Fourth.Int.Conf., Swansea (1985).
- Wille S.Ø. and Walløe L.,'Pulsatile pressure and flow in arterial stenoses simulated in a mathematical model.', J. Biomed. Engng., 3, p 17-24 (1981).
- Womersley J.R.,'Methods for calculation of velocity, rate of flow and viscous drag in arteries when the pressure gradient is known.', J. Physiol., 127, p 553-563 (1955).
- Yang C-T. and Alturi S.,'An "assumed deviatoric stress-pressure-velocity" mixed finite element method for unsteady, convective, incompressible viscous flow: Part II: computational studies.', Int. J. Num. Meth. Fluids, 4, p 43-69 (1984).
- Yongchareon W. and Young D.F.,'Initiation of turbulence in models of arterial stenoses.', J. Biomech., 12, p 185-196 (1979).

CHAPTER 4: PULSATILE FLOW IN TWO-DIMENSIONAL CAROTID BIFURCATION MODELS.

4.1. Introduction.

The numerical analysis of the flow in bifurcation models has been the subject of many investigations. Until now, fully three-dimensional time-dependent computations are limited by the required computer capacity. As far as we know, fully three-dimensional computations have only been reported by Wille (1984), who simulated the flow inside a model of the aortic bifurcation under steady flow conditions (Re=10) by means of a finite element method. In consequence, only two-dimensional numerical analyses will be reviewed here. They will be compared with experiments in three-dimensional configurations to get an idea of the relevance in physiological applications.

Computations of steady flow in two-dimensional bifurcation geometries are reported by Kandarpa and Davids (1976), Kawaguti and Hamano (1979), Wille (1980), Liepsch et al. (1982) and Friedman and Ehrlich (1984). From these steady flow analyses, the following characteristics can be derived :

i) boundary layer separation along the non-divider-side wall, resulting in a reversed flow region which extends into the daughter branch(es) of the bifurcation.

ii) the length of this reversed flow region increases with increasing Reynolds numbers and depends on the flow rate or area division ratio (Kandarpa and Davids, 1976, Kawaguti and Hamano, 1979, Wille, 1980 and Liepsch et al., 1982). The localization of the upstream end of this region for a given geometry, flow rate and area division ratio , however, is nearly unaffected by the Reynolds number (Kandarpa, 1976).

iii) at the divider side wall a peak in shear stress is observed at the apex which drops to an asymptotic value in the downstream direction (Kandarpa and Davids, 1976 and Friedman and Ehrlich, 1984).

iv) reduction of the branch angles diminishes the reversed flow area at the non-divider-side wall, but does not significantly affect the peak apex stress values (Kandarpa and Davids, 1976, Wille, 1980 and Kawaguti and Hamano, 1979).

These steady flow observations were confirmed by the results of two-dimensional experiments of Mark et al. (1977) and Liepsch et al. (1982).

The importance of unsteadiness of the flow has been pointed out by Friedman et al. (1975), O'Brien et al. (1976), Fernandez et al. (1976), Ehrlich and Friedman (1977), Florian and Perktold (1982), Perktold and Gruber(1983) and Perktold and Hilbert (1986), all of whom studied numerically the flow in two-dimensional bifurcation models under both steady and unsteady flow conditions. From these studies it follows that the unsteadiness of the flow implies temporal variations in the localization and length of the reversed flow regions, and in the wall shear stress values, which are significantly larger than their mean values. These variations depend on the temporal variations of the flow rate distribution. The experimental study of two-dimensional unsteady flow in bifurcation geometries of Mark et al. (1977) partly confirms the above mentioned observations.

The most important shortcoming of two-dimensional analyses is the negligence of secondary velocity components occurring in three-dimensional geometries. Until now, insight into the characteristics of this secondary flow field and its influence on the axial velocity distribution in bifurcation geometries could only be obtained from experimental studies. Steady flow studies were performed in symmetrical (Ferguson and Roach, 1972, Rodkiewicz and Roussel, 1973, Brech and Bellhouse, 1973, Fuerestein at al., 1976 and Siouffi el al., 1984) and asymmetrical (LoGerfo et al., 1981, Liepsch et al., 1981, Karino et al., 1982, Bharadvaj et al., 1982 and Zarins et al., 1983) models of planar (all branches located in one plane of symmetry) bifurcation geometries. Unsteady flow in three-dimensional bifurcation models has been studied by Ferguson and Roach (1972), Brech and Bellhouse (1973), LoGerfo (1981), Walburn and Stein (1981), Battan and Nerem (1982), Ku and Giddens (1983), Ku (1983), Siouffi et al. (1984) and Ku et al. (1985). An additional characteristic of three-dimensional flow, as compared to two-dimensional flow, is the helical

flow pattern in the daughter branches induced by the secondary velocity distribution, which is found to have properties similar to those observed in three-dimensional bend flow (Brech and Bellhouse, 1973, LoGerfo, 1981). Because of this secondary flow, fluid from the non-divider-side wall of the daughter branch, which has a small or even negative axial velocity component at the entrance, is transported to the center of the branch. Fluid from the divider-side wall, which has a relatively large axial velocity component, is transported along the walls of the branch towards the non-divider side. It is clear that this flow phenomenon, related to the centrifugal forces acting at this site of the bifurcation, influences the axial velocity distribution in the plane of symmetry and that deviations from two-dimensional models can be expected. Still, the axial velocity and wall shear stress distributions show characteristics similar to those described above for two-dimensional flow.

The influence of the presence of a small stenosis in bifurcation geometries has been studied less extensively. Clark et al. (1983) derived numerical approximations of the pulsatile flow in a two-dimensional bifurcation geometry with stenoses of 0%, 25% and 50% area reduction proximal to the flow divider of a symmetric branching and observed significant differences in velocity, pressure and wall shear stress distribution. The presence of a stenosis causes a large increase in wall shear stress and negative pressure excursion at the site of maximal area reduction, which increases with the severity of the stenosis. Gruber and Perktold (1983) only studied the influence of severe stenoses (>75% area reduction) in the femoral artery by means of a two-dimensional finite element analysis. Laser-Doppler measurements of steady axial velocity profiles in the plane of symmetry of a model carotid bifurcation, having a geometry as proposed by Bharadvaj et al. (1983), have been reported by Corver et al. (1985). In these experiments it was found that a smooth filling-in of the non-divider side of the internal carotid sinus exhibits only small deviations in axial velocity profiles as compared to measurements in a non-stenosed geometry.

Most of the three-dimensional experimental studies mentioned above indicate that the results of two-dimensional analyses have to be interpreted with care, when applied to the physiological situation in-vivo because secondary flow is not considered. In spite of this it

is assumed that two-dimensional analyses do give qualitative insight into some important characteristics of the axial velocity and wall shear stress in the plane of symmetry of the flow pattern in three-dimensional geometries.

In section 4.2 of this chapter, some general properties of pulsatile flow in a two-dimensional asymmetric bifurcation (Bharadvaj geometry) will be described. The description will be based on the computed axial velocity profiles, wall shear stresses and reversed flow regions in several phases of the cardiac cycle. Then in section 4.3 the calculations will be validated by means of a comparison with the results of Laser-Doppler measurements of unsteady flow in a two-dimensional experimental model. Furthermore, a comparison will be made between the axial velocity profiles as recorded in the plane of the bifurcation of a three-dimensional model, and the results of two-dimensional calculations. Besides, in section 4.4, observations made on the influence of a small stenosis on the flow pattern in two-dimensional bifurcation geometries are described and discussed. In the concluding discussion (section 4.5), the results obtained from the computations and measurements will be discussed with emphasis on the relevance to the physiological situation.

4.2. General properties of pulsatile flow in a two-dimensional model of the carotid artery bifurcation.

4.2.1. Introduction.

In order to describe the general flow field in a two-dimensional model of the carotid artery bifurcation, the time-dependent Navier-Stokes equations are solved for the bifurcation geometry described by Bharadvaj et al. (1982) (see chapter 1). The geometry and mesh distribution as used in the computation are given in Fig. 4.1. , where the dimensions are scaled with regard to the diameter (L_1=D) of the common carotid artery.

The inflow conditions used were the fully developed velocity distributions in a straight channel as described in the previous chapter with the same mean Reynolds number (Re=250) and the same frequency parameter (α=4). Stress-free outflow conditions for both the internal and external carotid arteries were imposed, whereas no-

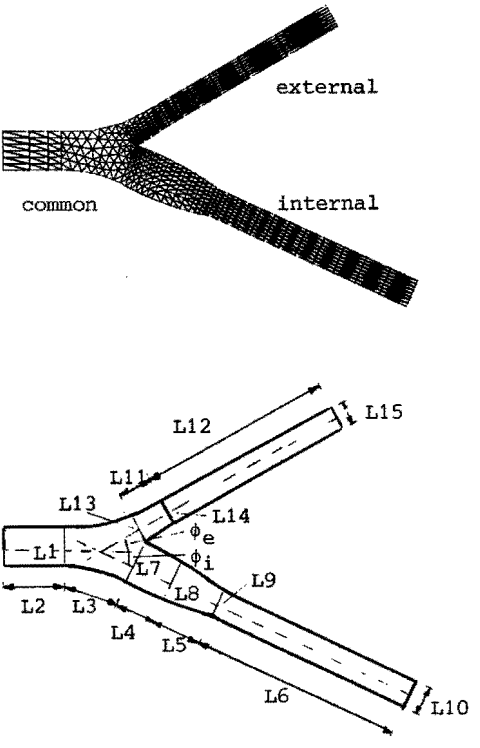

L1	1.00
L2	1.50
L3	2.00
L4	0.91
L5	1.49
L6	5.60
L7	1.04
L8	1.11
L9	0.72
L10	0.72
L11	1.00
L12	5.00
L13	0.69
L14	0.58
L15	0.58
ϕ_i	25.0°
ϕ_e	30.0°

Fig. 4.1 : Geometry and mesh of the two-dimensional bifurcation model after Bharadvaj (700 elements, 1511 nodes).

slip conditions were used at the walls. The solution of the steady Navier-Stokes equation for the flow rate value at the end of diastole was used as initial condition for the time-dependent calculation. A Crank-Nicolson time integration scheme (see chapter 2) was used with a timestep equal to 0.01T (i.e. 100 timesteps in one cardiac cycle). From the flow rate curve (Fig. 4.4a) it is observed that the flow in the internal and external carotid arteries mimics the total flow rate curve and that the difference in flow rate between the internal and external carotid arteries is constant during the entire flow cycle, except for a small period of time during systolic deceleration, where both flow rates are almost equal. The mean flow division ratio between the internal and external carotid arteries was found to be about 0.60:0.40.

In the remainder of this section detailed properties of the calculated flow field in various parts of the bifurcation are described by means of the axial velocity profiles, the wall shear stresses and the distribution of the reversed flow regions during the cardiac cycle.

The wall shear stresses were calculated from the velocity derivatives $\partial u_i/\partial x_j$ (i=1,2 and j=1,2) which were calculated from the velocity with the use of the following formula :

$$\frac{\partial u_i}{\partial x_j} = \frac{\partial}{\partial x_j} \sum_{k=1}^{N} u_{ik}\varphi_{ik} = \sum_{k=1}^{N} u_{ik}\frac{\partial \varphi_{ik}}{\partial x_j} \qquad i,j=1,2 \qquad (4.1)$$

with φ_{ik} the basis functions as used for the finite element approximation, u_{ik} the nodal velocity in node k, and N the number of nodal points. In order to obtain the velocity derivatives in the nodal points, formula (4.1) was applied element by element. Since these velocity derivatives are discontinuous over the element boundaries, an averaging over the elements, in which the node concerned is located, was performed to obtain uniquely defined values in the nodal points. Since on the boundary of the elements, the derivatives of the basis functions are linear functions, the velocity derivatives were only evaluated in the vertices of the elements. The wall shear stress $\tau_w=\nu(\partial u_t/\partial n)$ at the midpoints of the elements (node k) was then calculated from :

$$\tau_{wk} = \nu\frac{\partial u_t}{\partial n} = \nu \sum_{i=1}^{2}\sum_{j=1}^{2} \frac{\partial u_{ik}}{\partial x_j} t_i n_j \qquad (4.2)$$

with $\vec{t}=[t_1,t_2]^T$ the tangential vector and $\vec{n}=[n_1,n_2]^T$ the outer normal, both defined by the co-ordinates of the vertices. The wall shear stress was scaled with the value $6\nu U_0/D$, which is equal to the wall shear stress for a parabolic profile in the common carotid artery at a flow rate corresponding with the mean Reynolds number.

Axial velocity profiles were calculated at 4 equidistant (0.5D) cross-sections in the common carotid artery starting at 0.5D from the apex of the flow divider. In the internal carotid artery 9 cross-sections at distances of 0.25D apart, 2 cross-sections at distances of 0.5D apart and 2 cross-sections at a distance of 1D apart were

used. Finally, in the external carotid artery, 5 cross-sections at distances of 0.5D apart and 2 cross-sections at a distance of 1D apart were used. In Fig. 4.2, the axial velocity profiles are given for t/T=0.00 (end diastole), t/T=0.08 (peak systole) , t/T=0.16 (half-way systolic deceleration) and t/T=0.32 (end systole), respectively. As the diastolic flow is almost stationary its axial velocity profiles can be well described by the transient from the profiles given for t/T=0.32 to those given for t/T=0.00. In Fig. 4.3 the wall shear stresses for the various walls are given as a function of x/D for the times t/T=0.00 (end diastole), t/T=0.08 (peak systole), t/T=0.16 (half-way systolic deceleration) and t/T=0.32 (end systole). In these graphs, the wall shear stresses of the internal-side wall at the common carotid artery and of the non-divider side-wall at the internal carotid artery are marked with circles in Fig.4.3a, the wall shear stresses of the external-side wall and the non-divider-side wall of the external carotid artery are marked with circles in Fig. 4.3b. The wall shear stresses at the divider-side walls at the internal and the external carotid arteries are marked with asterisks in Fig. 4.3a and 4.3b, respectively.

4.2.2. Detailed description of the flow field.

common carotid artery

The velocity profiles (Fig. 4.2) at the two most upstream cross-sections do not show significant differences with the fully developed inflow velocity profiles. These profiles are almost parabolic at the end of the diastolic phase (t/T=0.00) of the flow. Then the velocity rapidly increases during systolic acceleration resulting in a flattening of the profiles. During systolic deceleration the profiles show a tendency to flow reversal at both walls and finally develop again to the parabolic shape at the end of the diastolic phase of the flow. In this entrance region, the wall shear stress (Fig.4.3) is observed to be equal for both the internal- and external-side walls. At the end of diastole (t/T=0.00) its value is about 0.7. This equals approximately the value of a parabolic profile at end-diastolic flow rate. At peak systole (t/T=0.08) the wall shear stress is about 7 times higher and about twice as high as can be

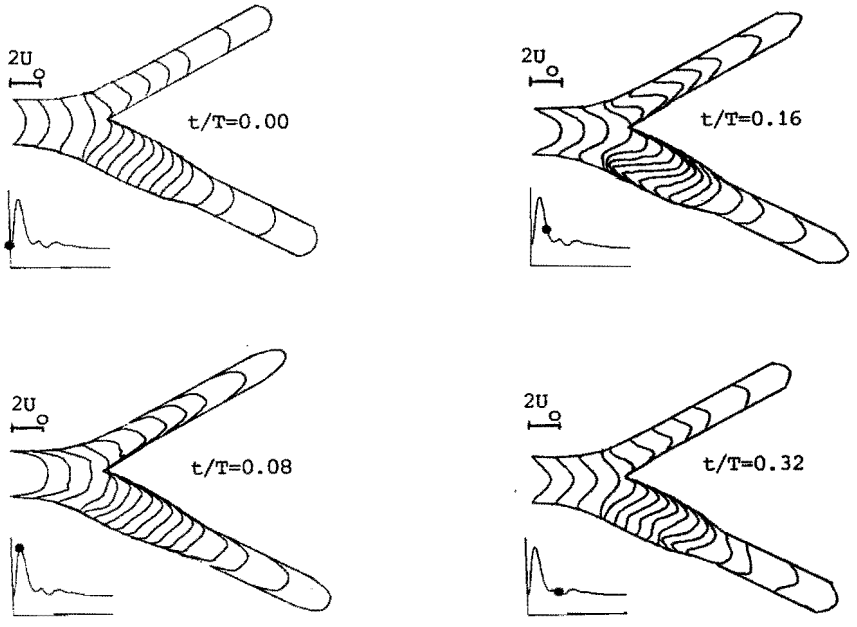

Fig. 4.2 : Axial velcity profiles for t=0.00T, t=0.08T, t=0.16T and t=0.32T respectively as calculated in the two-dimensional Bharadvaj geometry (175<Re<650, α=4).

expected from a parabolic profile at peak systolic flow rate. During systolic deceleration (t/T=0.08 to t/T=0.32) the wall shear stress in the entrance region of the common carotid artery rapidly recovers its end-diastolic value.

At the cross-section located 1D proximal to the apex, the axial velocity distribution is influenced by the widening of the common carotid artery resulting in reversed flow at the walls and a decrease of the wall shear stress at the end of the systolic deceleration. This phenomenon is found even more pronounced at the cross-section at 0.5D upstream of the apex. As the common carotid artery divides asymmetrically, the reversed flow occurring at the internal-side wall is larger and covers a larger region than that at the external-side wall. As a result a larger decrease of the wall shear stress is found at the internal-side wall. During diastolic flow the reversed flow,

caused by the widening of the common carotid artery, is small. During systolic acceleration no reversed flow is found at all but a relatively large decrease of the wall shear stress can be observed, whereas during systolic deceleration the reversed flow in this region reaches its maximum value and a negative wall shear stress is found. The distribution of the wall shear stress along the wall of the widening, however, is globally the same as at peak systole. The upstream influence of the apex of the flow divider is hardly noticeable in the velocity profiles, even at the nearest cross-section.

internal carotid artery

The flow in the internal carotid artery shows a relatively complex behaviour in place and time. At the end of the diastolic phase of the flow (t/T=0.00), the axial velocity in the carotid sinus features a region with small negative velocities at the non-divider side and positive velocities at the divider side of the cross-sections. In the downstream direction these profiles develop to parabolic profiles similar to those found in the common carotid artery. In consequence, relatively large values of wall shear stress are found at the divider-side wall, rapidly decreasing in downstream direction, whereas relatively small or negative values are found at the non-divider-side wall. At peak systolic flow (t/T=0.08), the reversed flow vanishes and the profiles are more or less blunted, though the maxima of the profiles are still located at the divider-side wall. The wall shear stresses are relatively high at both the divider- and the non-divider-side walls. A small local maximum is observed in the most distal part of the sinus where the walls converge maximally and develop into the parallel wall section of the internal carotid artery. During systolic deceleration (t/T=0.16) large differences in the axial velocities are found in the carotid sinus. Relatively large negative velocities with relatively large negative values of the wall shear stress occur at the non-divider-side wall up to 1.5D downstream of the apex. The region of reversed flow occupies up to 30% of the local diameter and is associated with high positive velocities at the divider-side wall where a large peak is found in the wall shear stress. At the cross-section located 1.5D downstream of the apex, the reversed flow is located at the divider-side wall whereas positive

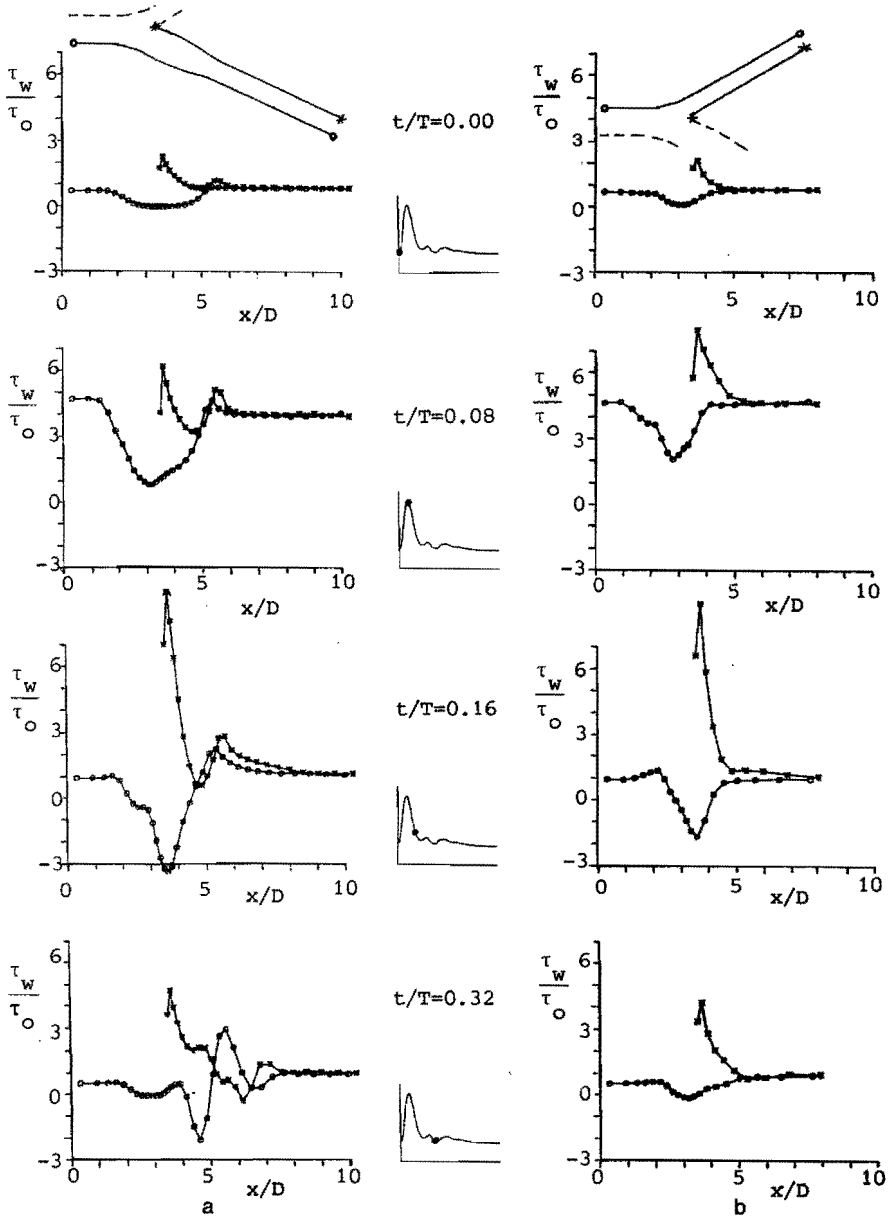

Fig. 4.3 : Dimenionless wall shear stress along the common-internal (o) ,divider-side internal (*), common-external (o) and divider-side external (*) walls for t=0.00T, t=0.08T, t=0.16T and t=0.32T respectively, as calculated in the two-dimensional Bharadvaj geometry (175<Re<650, α=4).

axial velocities are found on the non-divider sides of the cross-sections. The wall shear stress at this site shows a local minimum on the divider side and a rapid increase on the non-divider side both followed by a local maximum in the converging part of the sinus. Downstream of the carotid sinus, the profiles gradually recover a parabolic shape. Near the end of the systolic deceleration phase (t/T=0.32), the axial velocity profiles in the carotid sinus become even more complicated. At the entrance of the sinus the axial velocity profiles are characterized by a relatively large region with small negative velocities at the non-divider side wall, similar to the pattern at end-diastolic flow (t/T=0.00). At the cross-sections at 0.75D to 1.5D, however, the reversed flow region moves away from the wall, resulting in a situation with negative axial velocities in the centre of the sinus. Further downstream the reversed flow region reattaches to the wall. Downstream of the carotid sinus the profiles recover to a parabolic shape. This recovery features a shift of the maximum of the profiles from the divider-side to the non-divider-side wall between 3D and 4D downstream of the apex. In accordance, the wall shear stresses show complex spatial oscillations at both walls.

external carotid artery

The axial velocity profiles and wall shear stresses in the external carotid artery globally show the same characteristics as found in the internal carotid artery. Yet reversed flow is found at the non-divider side wall at the end of the diastolic phase of the cardiac cycle (t/T=0.00). This region, however, is smaller in both axial and cross-sectional directions and lower wall shear stresses are found. At peak systole (t/T=0.08) flattened velocity profiles are found with a maximum at the divider-side wall whereas no reversed flow occurs. During systolic deceleration (t/T=0.16) flow reversal at the non-divider-side wall is found in the external carotid artery. In contrast to the internal carotid artery, at the end of systolic deceleration (t/T=0.32) the axial velocity profiles do not show a deviation of the reversed flow region from the non-divider-side wall. Furthermore, the local maxima in the wall shear stress, as found at the transition from the carotid artery sinus to the parallel wall section have no counterpart in the external carotid artery.

reversed flow regions

Although the four phases of the pulse cycle used to describe the variations of the velocity profile and the wall shear stress are thought to be characteristic of the changes that take place during the cardiac cycle, they do not give a complete picture of the complex flow properties during the entire cardiac cycle. More insight into these complex properties can be obtained from the development and break-down of the reversed flow regions.

In Fig. 4.4 , the locations of reversed flow along the common-internal wall and the divider-side wall of the internal carotid artery are given as a function of time during one cardiac cycle. The flow rate curves for the common, internal and external carotid arteries are given at the top of this Figure to relate the properties of the reversed flow regions with the rate of flow.

From Fig. 4.4 it may be concluded that during the second half of the cardiac cycle ($t/T>0.5$) a reversed flow region exists at the common-internal wall covering the region from the diverging part of the common carotid artery ($x/D=3$) to the distal part of the internal carotid sinus ($x/D=5$). This reversed flow region is resolved by the systolic acceleration of the flow ($t/T=0.00$). Shortly after the peak systolic flow rate ($t/T=0.08$), a new reversed flow region starts at the widening of the common carotid artery, which gradually grows in both the upstream and downstream directions. Half-way the systolic deceleration ($t/T=0.20$) this reversed flow region covers a small region of forward flow at the entrance of the internal carotid artery. At the same time, reversed flows are observed in the common carotid artery and at the distal part of the divider-side wall of the internal carotid sinus. Subsequently, the reversed flow regions in the common carotid artery and the divider-side wall of the internal carotid artery vanish, whereas the reversed flow regions at the non-divider-side wall of the carotid sinus move in upstream direction. At the end of the systolic deceleration ($t/T=0.32$) the reversed flow region at the divider-side wall of the internal carotid sinus disappears, whereas the reversed flow region at the non-divider-side wall still moves in downstream direction. Furthermore, a new region of reversed flow is formed at the diverging part of the common carotid

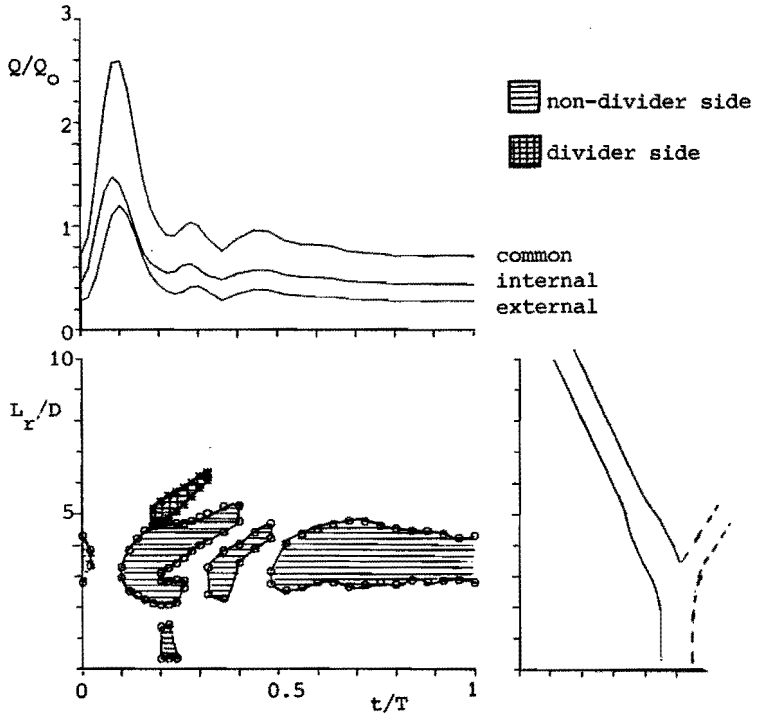

Fig. 4.4 : **Flow rate in the common, internal and external carotid artery as a function of time and locations of flow separation along the internal carotid walls as computed in the two-dimensional Bharadvaj geometry (175<Re<650, α=4).**

artery. Similar to the formation of the reversed flow region after peak systolic flow, the formation of this new region of reversed flow takes place at the onset of a deceleration of the flow. The two existing reversed flow regions at end systolic flow phase both move in downstream direction. During the third acceleration of the flow, the most distal reversed flow region disappears, whereas the other reversed flow region is restricted to the central part of the carotid sinus. At the onset of the third deceleration of the flow, again a new reversed flow region is formed at the diverging part of the common carotid artery. Meanwhile, the region of reversed flow in the carotid sinus disappears. Subsequently, the new formed reversed flow

region grows in downstream direction up to the parallel wall section of the internal carotid artery. This reversed flow region then does not undergo significant changes during the rest of the diastolic flow period.

4.3. Experimental validation.

4.3.1. Introduction.

In order to validate the numerical model, laser-Doppler measurements have been performed in both a two- and three-dimensional model of the carotid artery bifurcation. In the two-dimensional model, axial velocity profiles at several cross-sections in the bifurcation are determined. The results of the measurements are directly compared with corresponding velocity profiles obtained from calculations performed on the basis of equivalent flow rate conditions (Rindt et al.,1987). This comparison gives a good insight into the possible shortcommings of the numerical method. The comparison with measurements in the three-dimensional model of the carotid artery bifurcation (Versteijlen,1985) has been carried out to obtain an insight into the value of the two-dimensional modelling of the flow in a three-dimensional bifurcation. To this end, the axial velocity profiles in the plane of symmetry are compared with those obtained from two-dimensional calculations. The comparison with the measurements in the two- and three-dimensional models will be described in the sections 4.3.2 and 4.3.3, respectively. In these sections only little emphasis will be laid on the experimental method used. For a more extended treatment of this aspect, the reader is referred to appendix 3. In section 4.3.4, the results of the study of Ku (1983), who performed Laser-Doppler velocity measurements in a comparable but three-dimensional bifurcation geometry under the same flow rate conditions as in the two-dimensional calculations described in section 4.2, are used to relate the two-dimensional numerical results with fully three-dimensional experimental flow.

4.3.2. A comparison with measurements in a two-dimensional model.

In the measurement section of the two-dimensional experimental model,a relatively long rectangular entrance channel with a height of 1D and a width of 6D was used. This ensured the flow proximal to the bifurcation to be fully developed with respect to the height direction. The dimensions of the bifurcation in height direction correspond with the bifurcation geometry described in chapter 1. However,the angle between the axes of the common and the external carotid arteries was 30 instead of 25 degrees. Also relatively long outflow channels were used to ensure no upstream influence of the outflow configuration (see appendix 3). The flow rate, defined as the mean cross-sectional velocity times the diameter D, varied almost according to a sinus-function. Owing to the non-linearities in the transference between the stop-cock movement, used to impose the unsteady component of the flow, and the final flow rate, no pure sinusoidal flow rate was generated in the set-up used. This resulted in a flow rate as plotted in Fig. 4.5, where the Reyolds-number, based on the mean cross-sectional velocity in and the height of the common carotid artery, varies from 250 to 770 with a mean value of about 560. The frequency parameter α approximately equals 8. The flow rate division ratio between the internal and external carotid arteries is observed to be about 0.65:0.35 throughout the entire flow cycle. The axial velocities were measured at 40 equidistant points in time in one cycle of the flow (see appendix 3). The measuring accuracy was increased by averaging over 10 flow cycles.

In the calculations, the measured axial velocity at the cross-section located 2.5D upstream the apex of the flow divider was imposed as inflow condition, together with zero cross-sectional velocity. Per flow cycle 20 equidistant timesteps were used. In order to damp oscillations in the solution caused by the initial solution (u=v=0) a Euler-implicit time integration was used during the first flow cycle. Then two flow cycles were calculated with a Crank-Nicolson time integration, resulting in a solution which is not changing in the third significant number between two successive flow cycles.

In Fig. 4.6 the measured and calculated axial velocity profiles are given separately for the common (a), internal (b) and external (c) carotid arteries, respectively. For each branch, the profiles are

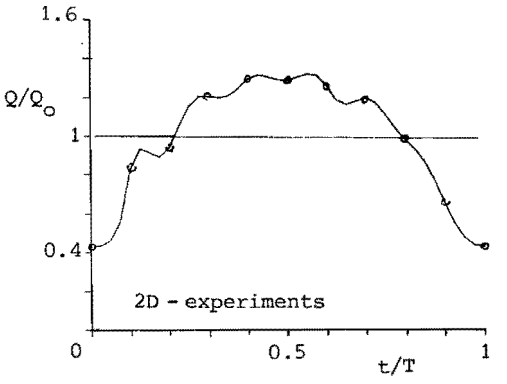

Fig. 4.5 : Flow rate as a function of time as used in the two-dimensional Laser-Doppler experiments (250<Re<770, α=8).

given for ten equidistant instants of time, starting from the moment with minimum flow rate (see Fig. 4.5). The calculated profiles are given by solid lines, whereas the circles represent the measurements. Small discrepancies between the geometries of the experimental and numerical models are visible at the entrances of the internal and external carotid arteries.

common carotid artery

The velocity profiles in the common carotid artery are given for 5 equidistant cross-sections at distances of 0.5D apart, with the most upstream cross-section at a distance of 2.5D from the apex of the flow divider (Fig. 4.6a).

At the entrance of the common carotid artery, the profiles are found to be symmetrical with respect to the axis of the channel during the entire flow cycle. Also, no significant changes are found in downstream direction until the walls of the common carotid artery diverge. The differences between calculations and measurements are relatively small and observed to be maximal during the onset of the acceleration phase of the flow (t/T=0.10 and t/T=0.20). As distinct from the pulsatile flow situation as described in the previous section, reversed flow is found even in the entrance region of the common carotid artery at the end of flow deceleration (t/T=0.90 and

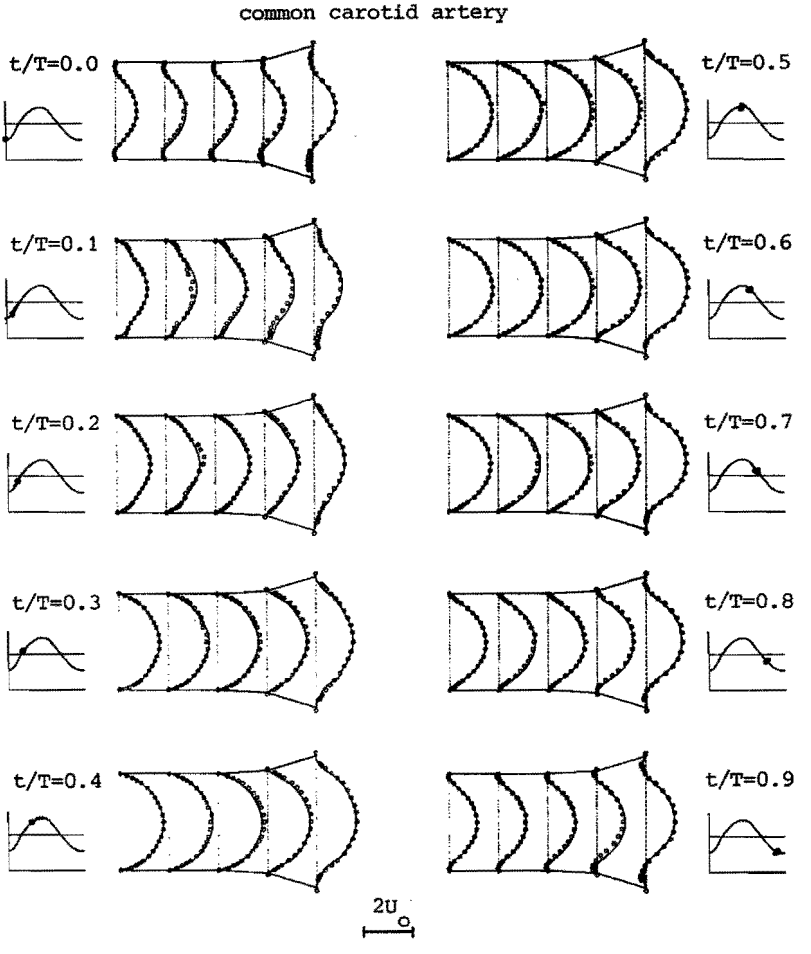

Fig. 4.6a : Two-dimensional experimental (o) and numerical (-) axial velocity profiles for the common carotid artery ($250<Re<770$, $\alpha=8$).

t/T=0.00). On the other hand, the divergence of the walls at the downstream side of the common carotid artery exhibits similar influences on the axial velocities, resulting in reversed flow at these walls during the deceleration phase of the flow. In these regions the differences found between the calculations and the measurements are slightly larger, partly due to the discrepancies in geometry.

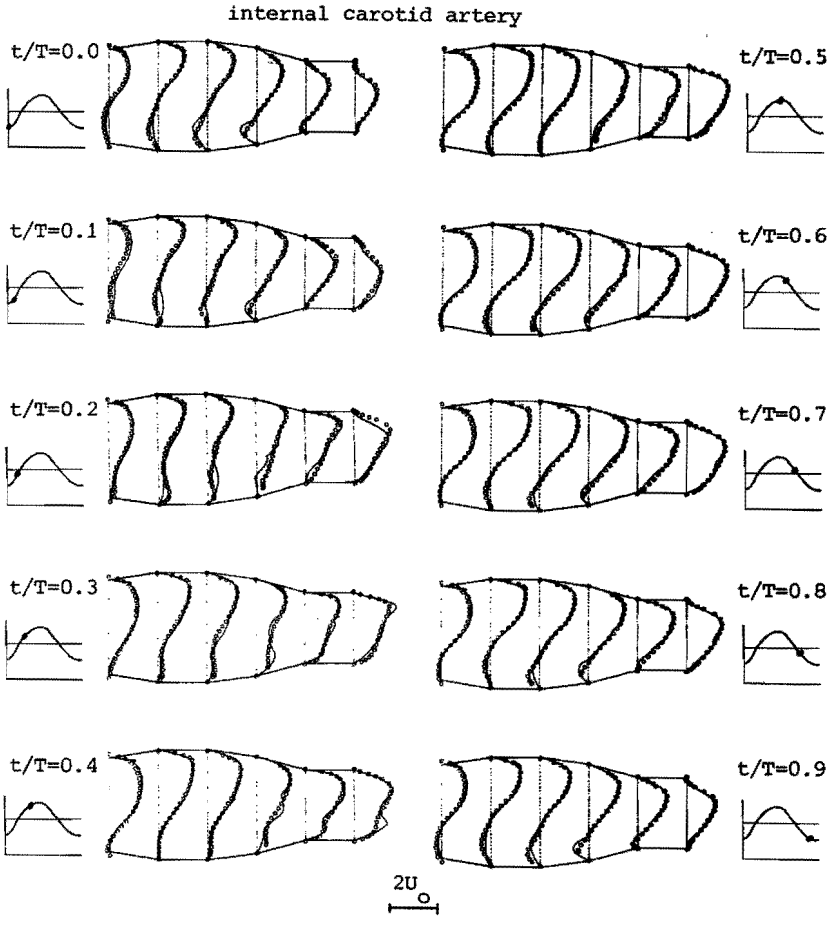

Fig. 4.6b : Two-dimensional experimental (o) and numerical (-) axial velocity profiles for the internal carotid artery (250<Re<770, α=8).

internal carotid artery

The velocity profiles in the internal carotid artery are given for 6 equidistant cross-sections with distances equal to 0.5D. Here the most upstream cross section is located at the apex of the flow divider (Fig.4.6b).

The axial velocity profiles resemble the ones found for the systolic phase of the flow described in the previous section. During flow acceleration, the reversed flow region at the non-divider-side wall, as formed in the deceleration phase of the flow, is resolved and velocity profiles with their maximum at the divider-side wall and low velocities at the non-divider-side wall, are observed. The flow characteristics connected with the transient to the steady-state flow in the diastolic phase of the pulsed flow configuration have not their counterpart in the 'sinusoidal' flow configuration described here, although, the separation of the reversed flow region at the end of the deceleration phase of the flow recurs in the measured velocities at the onset of the acceleration (t/T=0.20). Reversed flow at the divider-side wall is only found at the end of the deceleration phase of the flow at x/D=2.5. In general a good agreement is found between the experiments and the calculations. Similar to the situation in the common carotid artery, also here the largest differences between the measured and calculated velocities are found during the flow acceleration. Furthermore, it is observed that the deviations between the experiments and calculations in the large velocity gradient region at the divider-side wall are relatively small in comparison with those found in the regions with low and negative velocity gradients at the non-divider-side wall. Nevertheless, the successive development and break-down of the reversed flow regions are similar for both the experimental and numerical methods.

external carotid artery

In Fig. 4.6c the axial velocity profiles in the external carotid artery are given for 5 equidistant cross-sections at 0.5D apart starting from apex location. The shape of these profiles shows resemblance with the shape of the profiles in the internal carotid artery. Also here the largest differences between experimental and numerical data are found during the acceleration phase of the flow. The reversed flow regions, however, are approximated even better than in the internal carotid artery.

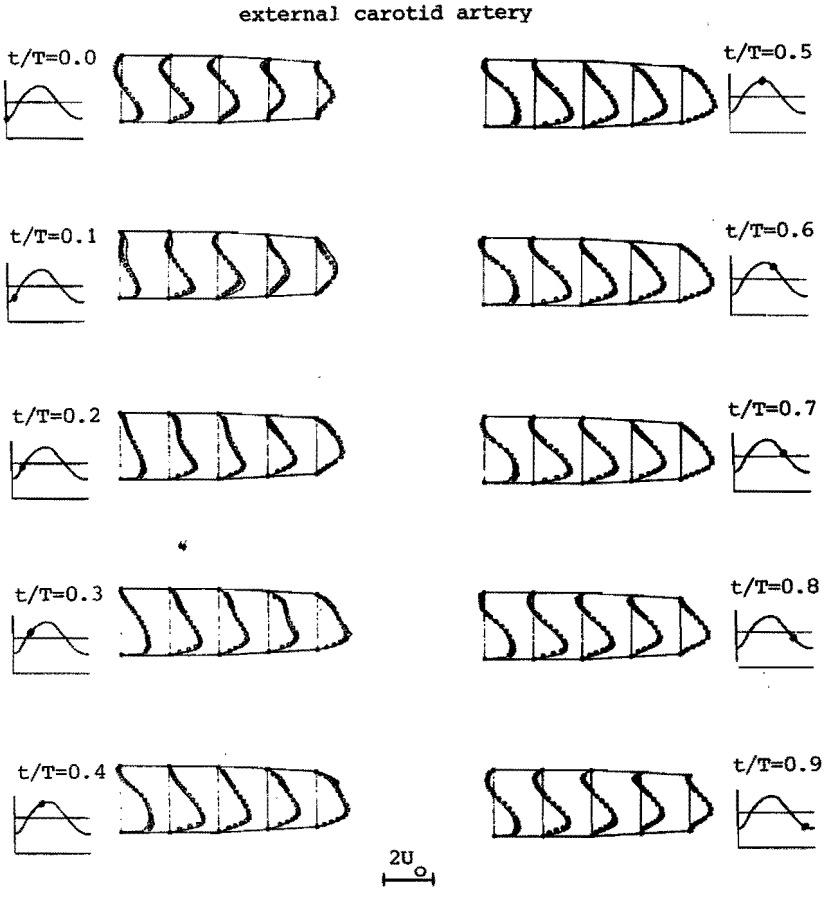

Fig. 4.6c : Two-dimensional experimental (o) and numerical (-) axial velocity profiles for the external carotid artery (250<Re<770, α=8).

4.3.3. A comparison with measurements in a three-dimensional model.

The dimensions of the three-dimensional model were, as far as the plane of symmetry of the bifurcation is concerned, equivalent to those of the two-dimensional model described above. Except for the transition region from the common carotid artery to the two daughter branches, the cross-sections were circular. In the transition region,

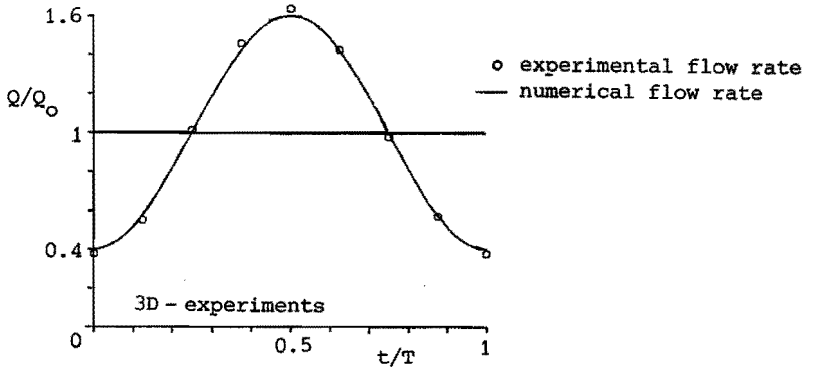

Fig. 4.7 : Flow rate as a function of time as used in the three-dimensional Laser-Doppler experiments (200<Re<800, α=6).

care was taken for a smooth intermediate shape. The flow rate, defined as the mean cross-sectional velocity in the plane of symmetry times the diameter D, varied sinusoidally (see Fig. 4.7), resulting in a mean Reynolds number, based on the diameter D and the cross-sectional and temporal mean velocity in the plane of symmetry, of about 500 and an amplitude equal to approximately 300. The frequency parameter α is equal to 6. The flow rate division between the internal and external carotid arteries was measured by means of two electromagnetic flow meters (see appendix 3) and amounts to approximately 0.70:0.30. At 40 equidistant points of time per flow cycle, the axial velocities in the plane of symmetry of the bifurcation were measured. Similar to the two-dimensional measurements described above, the measurement accuracy was increased by averaging over 10 flow cycles.

Since only little deviation is found between the experimental flow rate and a purely sinusoidal flow rate with a non-zero mean, the fully developed axial velocity profiles of such a flow in a straight channel were used as inflow condition for the calculations. The mean Reynolds number was taken to be 500, whereas the amplitude of the superimposed sinusoidal flow rate was equal to 300. Per flow cycle 64 equidistant timesteps were used. Similar to the strategy used for the computations described in the previous section, three flow cycles were calculated, of which the first has been performed with a Euler implicit and the last two with a Crank-Nicolson time integration. The same element distribution as used in the calculations described in

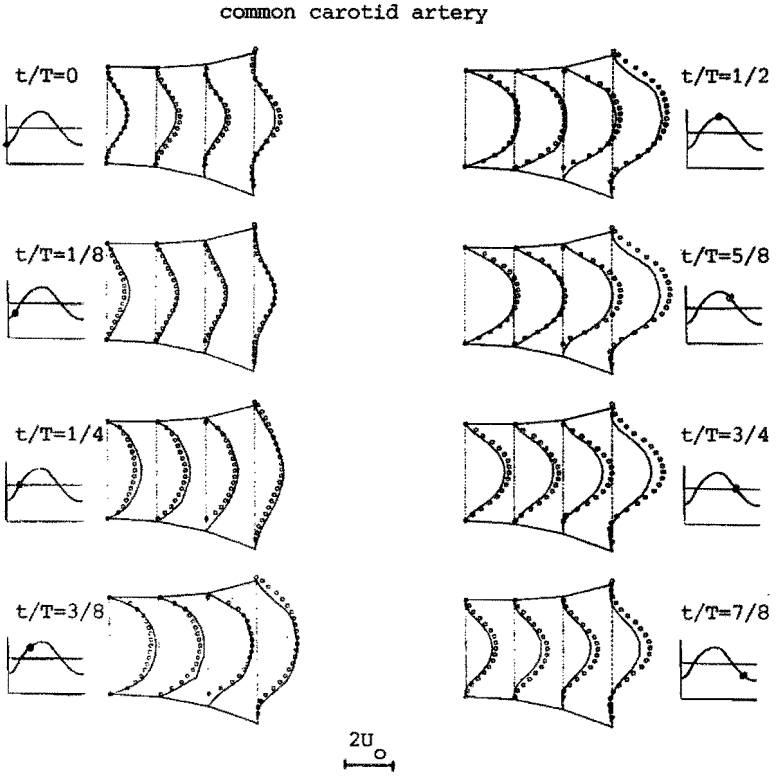

Fig. 4.8a : Three-dimensional experimental (o) and two-dimensional numerical (-) axial velocity profiles for the common carotid artery ($200<Re<800$, $\alpha=6$).

section 4.3.2 was applied. The measured and calculated axial velocity profiles are given in Fig. 4.8, separately for the common (a), internal (b) and external (c) carotid arteries. The profiles are given for 8 equidistant points of time throughout the flow cycle. The first point of time corresponds with minimal flow rate (see Fig. 4.7). The calculated profiles are given by the solid lines, whereas the experimental data are indicated by the circles.

common carotid artery

The velocity profiles in the common carotid artery are given for 4 equidistant cross-sections located at 0.5D apart. The most upstream cross-section is located at 2D from the apex of the flow divider. Despite the small discrepancies in the geometry and in the flow rate, mainly caused by a small phase shift (see Fig. 4.7), and despite the fact that three-dimensional measurements are compared with two-dimensional computations, relatively good agreement is found between the axial velocity profiles throughout the entire flow cycle.

internal carotid artery

In Fig. 4.8b, the velocity profiles in the internal carotid artery are given for 8 cross-sections at 0.25D apart. In this part of the bifurcation, the differences between two-dimensional numerical and three-dimensional experimental results are observed to be most important. The most striking deviations are found in the reversed flow regions. Except for the entrance region of the internal carotid artery, the reversed flow obtained from the computations covers cross-sectional regions which are about 50% of the regions as found in the experiments and exhibits negative axial velocities which are significantly larger. However, the lengths of the reversed flow regions found in the two-dimensional numerical model do not differ much from those observed in the three-dimensional experiments. Furthermore, relatively good agreement is found at the divider-side wall during the entire flow cycle.

external carotid artery

The axial velocity profiles in the external carotid artery are plotted in Fig. 4.8c. Here 3 cross-sections at a distance of 0.5D apart are used. Similar remarks as made for the internal carotid artery can be made here, and also here a relatively good agreement is found between the three-dimensional experimental results and the two-dimensional calculations.

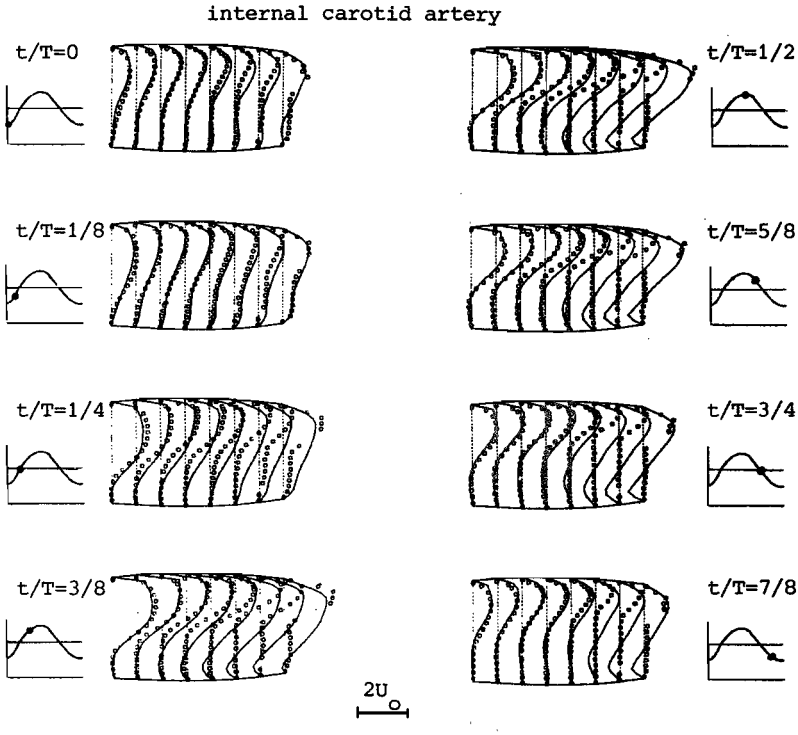

Fig. 4.8b : Three-dimensional experimental (o) and two-dimensional numerical (-) axial velocity profiles for the internal carotid artery ($200<Re<800$, $\alpha=6$).

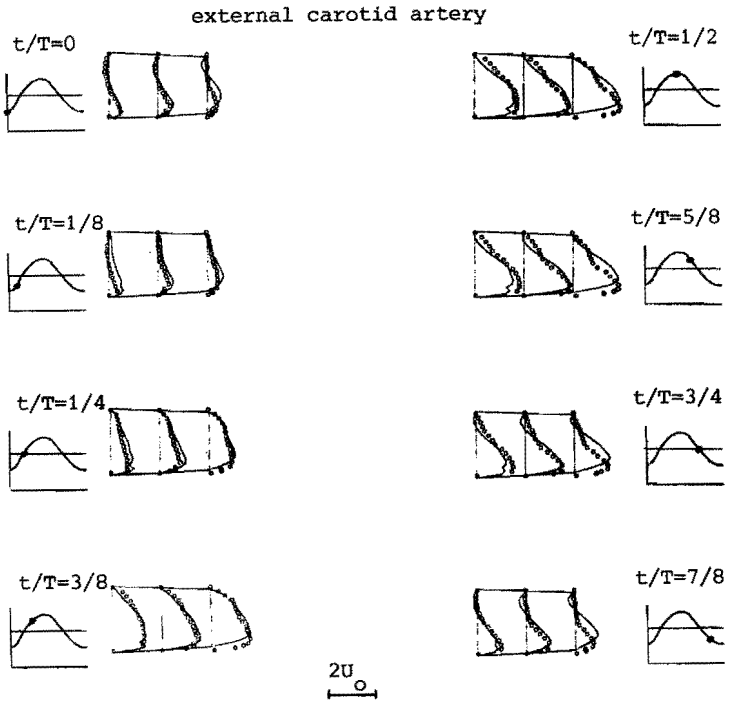

Fig. 4.8c : Three-dimensional experimental (o) and two-dimensional numerical (-) axial velocity profiles for the external carotid artery ($200<Re<800$, $\alpha=6$).

4.3.4. A comparison with measurements of Ku.

The calculations of the two-dimensional bifurcation flow described in section 4.2 are performed with a flow rate distribution and a geometry (in the plane of symmetry) similar to those of the three-dimensional measurements of Ku (1983). Since comparison of the axial velocity profiles obtained from both models is difficult because of the large amount of data, the comparison has been made by means of the axial wall shear stresses. Ku (1983) obtained the wall shear stresses from the measured axial velocities at three locations near the wall. In Fig. 4.9, the wall shear stresses at several locations on the wall are given as a function of time. For both models, the values have been scaled with the mean value in time found in the common carotid artery (location 1). The solid lines represent the experimental wall shear stresses, whereas the computed values are marked with circles.

In the common carotid artery (location 1 in Fig. 4.9), the wall shear stress follows the flow curve and good agreement is found between the experiments and calculations. At the entrance of the carotid sinus, the wall shear stress at the non-divider side (location 5 in Fig. 4.9) shows a relatively small increase at systolic deceleration followed by occurrence of negative values during the deceleration of the flow. In Ku's measurements the same features are found but they occur at an earlier time in the flow cycle. A similar time-dependence of the wall shear stress is found in the middle of the non-divider-side sinus-wall, although larger fluctuations are found. The two-dimensional (numerical) model predicts larger negative wall shear stresses than found in the three-dimensional (experimental) model. At the most distal location (location 7) on the non-divider-side sinus-wall, a relatively large peak in the wall shear is observed during systole for both models. In the two-dimensional model, this peak is followed by a second peak at the onset of diastole. In the mean, the wall shear stress found at this site in the three-dimensional model is larger than in the two-dimensional model. At the divider-side wall of the internal carotid sinus, relatively large values of the wall shear stress are found decreasing in downstream direction (locations 2,3 and 4 in Fig. 4.9). At the apex (location 2) and in the middle of the divider-side sinus-wall good

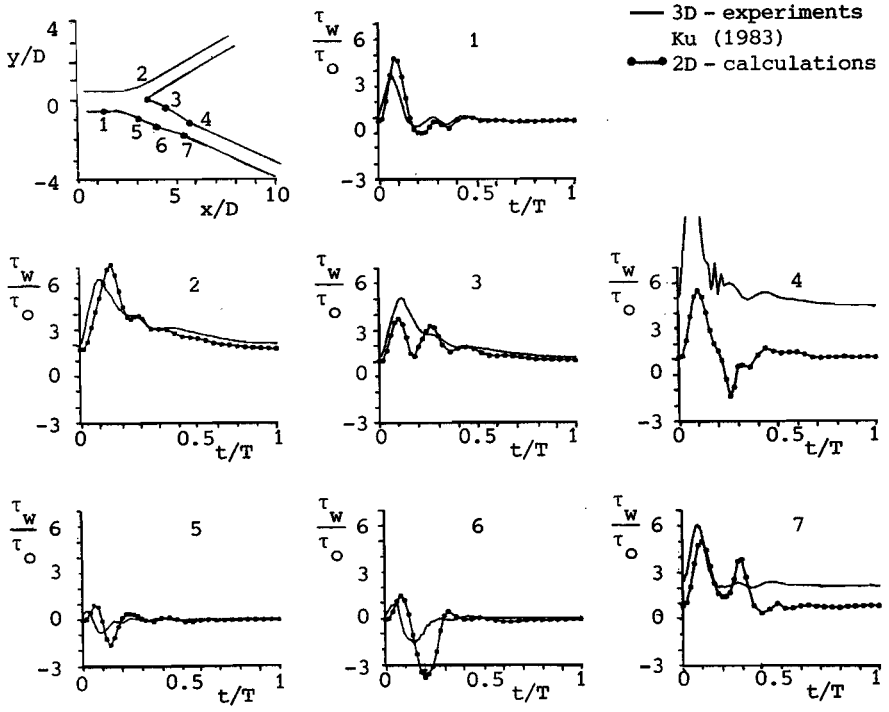

Fig. 4.9 : Dimensionless wall shear stress as a function of time for severeal locations in the common and internal carotid artery as calculated in the two-dimensional Bharadvaj geometry (o-o) compared with data obtained from the three-dimensional experiments of Ku (-) (175<Re<650, α=4).

agreement is found between both models, although a second oscillation in the wall shear stress of the two-dimensional model is found at the latter location. Relatively large values of the wall shear stress are observed at the most distal location (location 7) for the three-dimensional model. The shape of this curve, however, is quite similar to the one obtained from the two-dimensional calculations.

The essentials of the comparison are summarized in Table 4.2 (p 122, columns 2 and 3), where the minimum, maximum and mean wall shear stresses at several locations in the bifurcation are given and compared with the Ku's results (1983). In general it is concluded that relatively good agreement is found in the common carotid artery and in the entrance region of the carotid sinus. More downstream the differences become more serious, especially at the divider side wall.

4.4. Observations on the influence of a stenosed sinus based on two-dimensional computations.

The influence of the presence of a small stenosis (25% diameter reduction) in the internal carotid sinus on the velocity distribution and wall shear stress, has been analysed. Results of such an analysis can be useful for studies dealing with the detectability of atherosclerotic lesions from blood flow velocity patterns obtained from in-vivo measurements. As regards the detectability of atherosclerotic lesions, it is of importance to have an idea to what extent the influence of the stenosis on the flow field can be distinguished from inter-individual variations in geometry. Therefore, calculations were performed for two different geometries both with and without a stenosis in the internal carotid sinus, which is a common location for stenoses to occur. The geometries chosen are based on the dimensions obtained by Reneman et al. (1983), who studied the velocity patterns in subjects of various ages by means of in-vivo ultra-sound pulsed Doppler measurements. They distinguished between two groups (younger and older subjects) with small but characteristic differences in geometry of the carotid artery bifurcation. In Table 4.1 these characteristic dimensions are given together with those used in the Bharadvaj-geometry as used in section 4.2 . All dimensions are scaled to the diameter of the common carotid artery. The most characteristic difference between the two groups is found in the diameters of the internal carotid artery downstream the sinus (L10). In the group of younger subjects (group I) these diameters were observed to be smaller (0.87D) than in the group of older subjects (group II) (0.97D). In the Bharadvaj geometry, these diameters were significantly smaller and equal to 0.72D. For the angle of the axis of the internal with the common carotid artery, a mean value of about 12.5^{o} was found for both groups (twice as small as the value given by Bharadvaj et al. (1982)). Since in Reneman et al. (1983) no dimensions of the external carotid artery are reported, the geometry of this branch was taken to be equal for both groups.

The stenosis consists of a smooth fill-in of the upstream part of the non-divider-side wall of the sinus and a rounded step-like transition at the downstream side, resulting in a maximum diameter

Table 4.1 : Geometry parameters for the Bharadvaj geometry and Reneman geometries as used in the two-dimensional calculations (see also Fig. 4.1).

	Bharadvaj	Reneman I	Reneman II
L1	1.00	1.00	1.00
L2	1.50	1.00	1.00
L3	2.00	2.68	2.68
L4	0.91	1.50	1.50
L5	1.49	0.50	0.50
L6	5.60	5.50	5.50
L7	1.04	1.00	1.08
L8	1.11	1.03	1.11
L9	0.72	0.87	0.97
L10	0.72	0.87	0.97
L11	1.00	1.00	1.00
L12	5.00	5.00	5.00
L13	0.69	0.60	0.60
L14	0.58	0.60	0.60
L15	0.58	0.60	0.60
PHIi	25.0^{o}	12.5^{o}	12.5^{o}
PHIe	30.0^{o}	20.0^{o}	20.0^{o}

reduction of about 25% of the local diameter, assuming to be a possible stenosis geometry.

The boundary conditions and solution strategy were similar to those for the calculations with the Bharadvaj geometry (see section 4.2).

The results of the calculations for both geometries with and without stenosis will be compared by means of the axial velocity profiles, wall shear stresses and reversed flow regions. Despite the difference in flow rate between group I (flow division ratio of about 0.75:0.25) and group II (flow division ratio of about 0.85:0.15), the axial velocity profiles are quite similar for all situations and

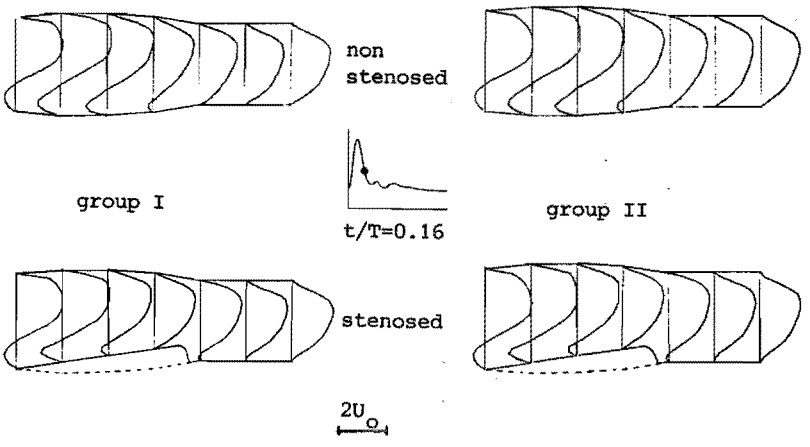

Fig. 4.10 : Axial velcity profiles for t=0.16T as calculated in the two-dimensional Reneman geometries for both non-stenosed and stenosed configurations (175<Re<650, α=4).

resemble the axial velocity profiles as found in the Bharadvaj geometry. The largest differences are observed during systolic deceleration (t/T=0.16) in the internal carotid sinus (Fig. 4.10). The reversed flow at the non-divider-side wall of the sinus is smaller than in the Bharadvaj geometry and almost identical for both groups for both the non-stenosed and the stenosed geometries. Here the influence of the stenosis is expressed most clearly at the first cross-section downstream the stenosis, where reversed flow is found in the stenosed geometries, whereas in the non-stenosed geometries the axial velocity remains positive for this cross-section.

The wall shear stresses are almost equal for geometry I and geometry II for both the non-stenosed and stenosed geometries (see Table 4.2, p 122). Maximal deviation is found at the apex (location 2). Furthermore, the wall shear stresses in the non-stenosed geometries do not show features different from those observed in the Bharadvaj geometry.

The influence of the stenosis is expressed in an increase of the wall shear stress proximal to the location of maximal diameter reduction (location 6). This increase is accompanied with a sudden

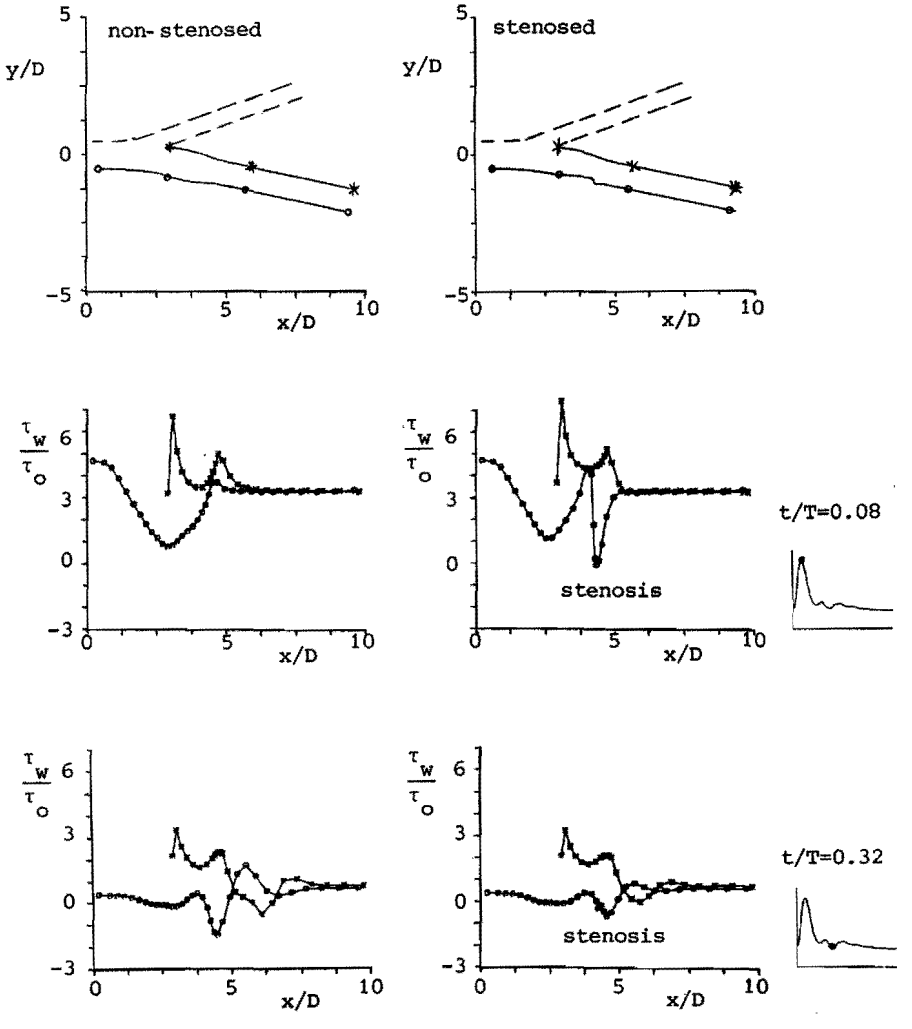

Fig. 4.11 : Dimenionless wall shear stress along the common-internal (o) and divider side internal (*) walls for t=0.08T and t=0.32T, respectively, as calculated in the two-dimensional Reneman geometrie (group I) for both non-stenosed and stenosed configurations (175<Re<650, α=4).

decrease downstream the stenosis (location 7) (see also Fig. 4.11 where the wall shear stress in the internal carotid artery is given for two points of time in systolic deceleration). At the end of the systolic deceleration (t/T=0.32), it is observed that the oscillations of the wall shear stress along both walls of the internal carotid artery as found in the Bharadvaj geometry, also occur in the geometries used here. At the non-divider-side wall, these oscillations are smaller in amplitude especially for the stenosed geometries (see Fig. 4.11). In Fig.4.12, the wall shear stresses at several locations in the common and internal carotid arteries are given as a function of time and compared with those obtained from a stenosed geometry. From these graphs it is observed that the upstream influence of the stenosis is negligible (locations 1, 2 and 5). The largest differences between the wall shear stresses in the stenosed and in the non-stenosed geometries are found during systolic deceleration. At the non-divider-side sinus-wall (location 6), the wall shear stress is slightly larger for the stenosed geometries but still similar characteristics are found for both stenosed and non-stenosed geometries. Further downstream (location 7), the situation is quite opposite: the wall shear stress in the stenosed geometry is now slightly smaller. At the divider-side wall, the most striking difference between the flows in the stenosed and in the non-stenosed geometries is observed at the distal part of the sinus (location 4) during systolic deceleration. At this site, negative wall shear stresses are found in the non-stenosed geometries, whereas in the stenosed geometries the wall shear stress remains positive.

The locations of reversed flow along the common-internal wall and the divider-side wall of the internal carotid artery are given as a function of time in Fig. 4.13 for geometry I-non-stenosed (a), geometry I-stenosed (b). Geometry II does not give different information. At the top of these pictures the flowrate in the common carotid artery is given as a function of time. The development and break-down of the reversed flow regions in the non-stenosed geometries exhibit properties comparable to those observed in the Bharadvaj geometry. In contrast with the situation in the Bharadvaj geometry, the reversed flow region in the sinus of the internal carotid artery disappears during the diastolic phase of the flow. The development and break-down of the reversed flow regions in the stenosed geometries show

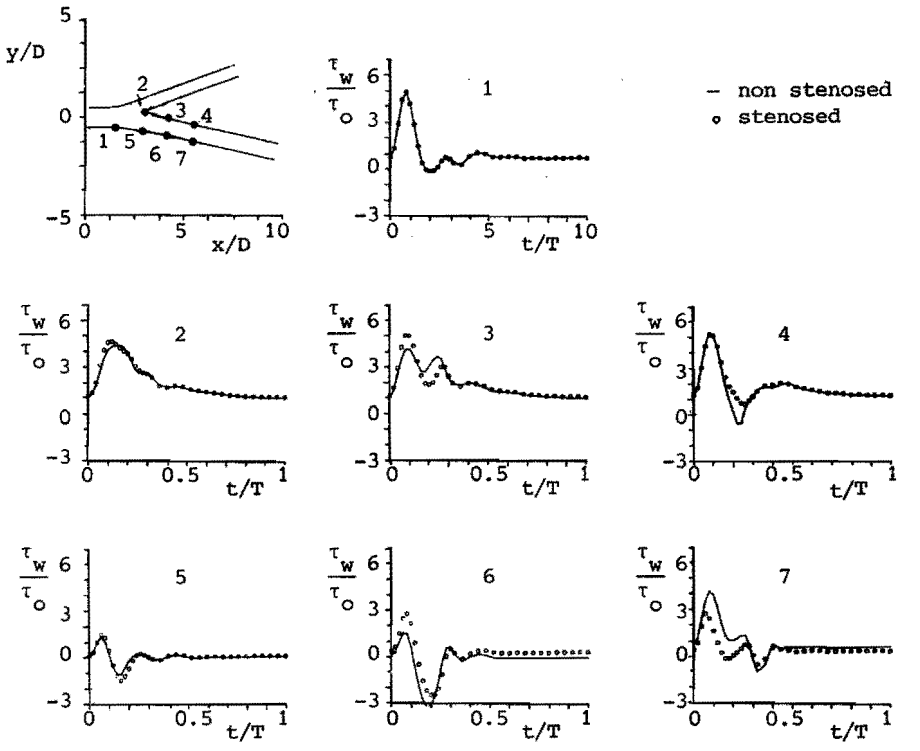

Fig. 4.12 : Dimensionless wall shear stress as a function of time for severeal locations in the common and internal carotid artery as calculated in the two-dimensional Reneman geometrie (group I) for both non-stenosed and stenosed configurations (175<Re<650, α=4).

some striking deviations from the situation in the Bharadvaj and the non-stenosed geometries. During the systolic flow acceleration, a reversed flow region is formed downstream the stenosis. Subsequently, this region grows in downstream direction and covers an axial distance of approximately 1D half-way the systolic deceleration of the flow. Hereafter, this region resolves rapidly, simultaneously with the reversed flow in the common carotid artery. Furthermore, except for a small period of time at the end of systolic deceleration, no reversed flow is observed at the divider-side wall of the internal carotid artery. Also the reversed flow region as found at the non-divider-side sinus-wall during the diastolic phase of the flow, has no counterpart in the stenosed geometries. On the other hand, a small region of reversed flow is observed downstream the stenosis.

Table 4.2 : Mean, maximal end minimal wall shear stress at several locations in the common and internal carotid artery (the wall shear stresses are made dimensionless by division with the mean value in the common carotid artery).

		Bharadvaj		Reneman			
location		Ku 3D exp.	Bh 2D num.	NI 2D num.	SI 2D num.	NII 2D num.	SII 2D num.
	mean	1.0	1.0	1.0	1.0	1.0	1.0
1: communis	max	3.6	4.7	4.9	4.9	4.9	4.9
	min	0.4	0.0	-0.1	-0.1	-0.1	-0.1
int.car.	mean	3.2	3.0	2.0	2.0	1.2	1.3
2: sinus	max	6.3	7.2	4.4	4.7	3.5	3.4
prox.div.	min	2.1	1.7	1.1	1.1	0.6	0.6
int.car.	mean	0.0	0.0	0.0	0.0	0.1	0.1
5: sinus	max	0.5	0.9	1.3	1.5	1.3	1.4
prox.non.	min	-0.8	-1.7	-1.1	-1.5	-1.0	-1.4
int.car.	mean	2.1	1.7	1.9	2.0	1.8	1.8
3: sinus	max	5.1	3.7	4.2	5.1	4.1	5.9
midp.div.	min	1.2	1.0	1.0	1.1	0.9	1.0
int.car.	mean	-0.1	-0.3	-0.2	0.2	-0.2	0.2
6: sinus	max	1.0	1.5	1.5	2.8	1.5	2.5
midp.non.	min	-1.7	-3.8	-3.2	-2.5	-3.1	-2.5
int.car.	mean	5.8	1.5	1.7	1.8	1.5	1.6
4: sinus	max	13.6	5.5	5.3	5.2	4.4	4.3
dist.div.	min	4.4	-1.4	-0.6	0.7	-0.5	0.6
int.car.	mean	2.5	1.5	0.9	0.5	0.7	0.3
7: sinus	max	6.1	5.0	4.2	2.7	3.7	2.2
dist.div	min	2.0	0.4	-1.0	-0.5	-1.7	-1.0

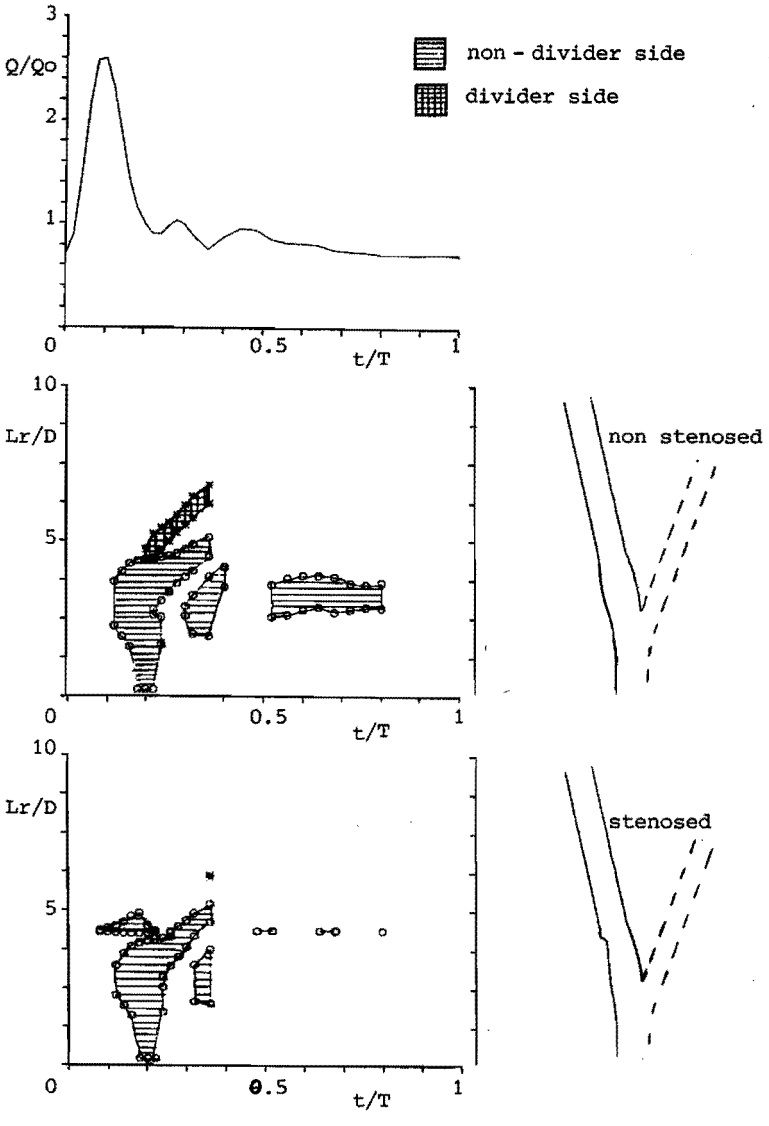

Fig. 4.13 : Flow rate in the common, internal and external carotid artery as a function of time and locations of flow separation along the internal carotid walls as computed in the two-dimensional Reneman geometrie (group I) for both the non-stenosed and stenosed configurations (175<Re<650, α=4).

4.5. Conclusions and discussion.

The results of the calculations presented in the preceding sections have given an indication of the complexity of the flow in two-dimensional carotid artery bifurcation geometries. From the two-dimensional experimental validation it is concluded that the numerical method used provides an accurate approximation of the spatial and temporal velocity distributions of unsteady flow in rigid two-dimensional bifurcation geometries.

As the results of the numerical two-dimensional models must be regarded carefully because they give only a partial picture of the flow situation in three-dimensional geometries, in this section these results will be discussed and related to properties which are thought to be of importance for the in-vivo situation. As far as possible, a comparison will be made with information obtained from literature, and the deviation from three-dimensional flow will be indicated. Furthermore, cautious conclusions concerning the influence of a small stenosis in the internal carotid artery sinus will be given.

Properties and physiological relevance of the flow in two-dimensional bifurcation models.

From the computations of the flow in the two-dimensional Bharadvaj geometry the following general properties can be derived.

At the entrance region of the common carotid artery, the influence of the bifurcation is not detectable and fully developed flow occurs. The axial velocity profiles are nearly parabolic at the end of diastolic flow, show a rather blunted shape at peak systole and gradually develop to a parabolic shape during systolic deceleration and the diastolic phase of the flow. The wall shear stress at this site is observed to increase with increasing flow rate and attains relatively low values at the end of systolic deceleration, where a tendency to flow separation is found. Similar properties were observed by Ku (1983) for three-dimensional flow. Also the agreement between two-dimensional calculations and three-dimensional measurements (see section 4.3.3) confirms the validity of two-dimensional modelling at this site of the bifurcation.

The distal part of the common carotid artery is characterized geometrically by a widening of the vessel. This widening is clearly expressed in the decrease of the wall shear stress and features flow reversal at end diastolic flow rate. During the acceleration phase of the flow, this tendency is opposed by the influence of the instationary inertia forces, resulting in relatively large wall shear stresses, whereas during flow deceleration, this tendency is intensified by the influence of the instationary inertia forces. Also at this site, the agreement between two-dimensional calculations and three-dimensional measurements (see section 4.3.3) indicates that the two-dimensional model still provides valuable information with respect to three-dimensional configurations.

Most complex flow properties are observed to occur in the carotid artery sinus. At this site, three geometrical factors are of importance. First, the internal carotid sinus exists of a widening and tapering of the vessel. Secondly, the transition from the common to the internal carotid artery exhibits curved tube-like properties. Lastly, the flow is influenced by the flow divider. At the end of diastole, the flow is almost steady and instationary inertia forces are thought to be less important. The flow divider and bend-like property of the transition from common to internal carotid artery give rise to axial velocity profiles with a maximum at the divider side of the sinus and therefore to relatively large values of the shear stress at the divider side wall. The widening and tapering of the sinus is most clearly expressed in the local minimum of the wall shear stress at the midpoint of the sinus. At the proximal part of the non-divider side of the sinus, all above mentioned geometrical properties co-operate to induce low and even negative axial velocities. At the distal part, the tapering of the sinus gives rise to a small increase of the wall shear stress with a maximum at the transition to the parallel wall section of the internal carotid artery. Since this transit is modelled with a relatively sharp corner, the importance of the magnitude of this maximum must not be overestimated. At peak systole, more or less blunted axial velocity profiles are observed, although their maxima are still located at the divider side. No reversed flow is found then and the wall shear stresses are relatively large at both the divider- and non-divider-side walls. The

wall shear stress distribution along the sinus walls shows characteristics similar to those observed at the end of diastole, although shifted to larger values. During systolic deceleration, the flow through the proximal part of the sinus is characterized by negative axial velocities at the non-divider-side wall and relatively large positive axial velocities at the divider-side wall. At the distal part, also reversal flow develops at the divider-side wall. Consequently, the wall shear stresses attain relatively large negative values at the non-divider-side wall and high values at the divider-side wall. At the end of systolic deceleration, the reversed flow region at the non-divider-side wall separates from the wall, resulting in an oscillating wall shear distribution along this wall.

From the comparison between the two-dimensional calculations and the three-dimensional velocity measurements (see section 4.3.3) it is observed that in the proximal part of the carotid artery sinus a relatively good agreement exists, whereas in the distal part significant deviations are found especially in the reversed flow region. Here the negative axial velocities obtained from the numerical model are larger and cover a smaller cross-sectional distance. This numerical overestimation of the negative axial velocities also follows from the comparison of the calculated wall shear stresses in the sinus with Ku's measurements. As the secondary velocity distribution in the three-dimensional flow affects the axial velocity component, the deviation between two- and three-dimensional flows at this site of the sinus is not inexplicable. Namely, from the experimental studies of Olson (1971), Brech and Bellhouse (1973) and LoGerfo (1981), it follows that these secondary velocity components exhibit properties resembling the entrance flow in a curved tube (see also Chapter 5). Combined with the axial velocity components, this gives the fluid a helical motion, transporting fluid along the side walls to the plane of symmetry, back to the divider-side wall. In consequence, fluid with a relatively large axial velocity is transported along the side walls to the non-divider side wall and fluid with a relatively small axial velocity is transported towards the centre of the vessel. Depending on the magnitude of the secondary velocity components, this results in a reversed flow region with a larger cross-sectional extension and smaller negative velocities. At the proximal part of the carotid sinus, however, the secondary flow is

not yet developed and its influence is still restricted to a small region; therefore it exhibits less important effects on the axial velocity at this site.

The parallel-wall section of the internal carotid artery generally shows a gradual recovery to fully developed flow as observed in the entrance region of the common carotid artery. At the end of the systolic deceleration, however, this recovery is accompanied by a shift of the maximum of the axial velocity profiles from the divider-side wall to the non-divider-side wall. This shift is also expressed in the wall shear stress, exhibiting spatial and temporal oscillations. In Ku's three-dimensional experiments (1983) this phenomenon is found less pronounced.

The flow in the external carotid artery globally shows similar characteristics as the flow in the internal carotid artery, although less pronounced. The most striking deviation from the internal carotid flow is found at the end of systolic deceleration, where the flow in the sinus features a separation of the reversed flow region from the non-divider-side wall and a relatively large reversed flow in the distal part.

Quite similar flow properties as described above have recently been reported by Perktold and Hilbert (1986), who approximated the two-dimensional flow in the Bharadvaj geometry for a slightly different flow rate form with a mean Reynolds number of 100 (varying from about 50 to 300) by means of a finite element method.

Although not always insignificant deviations between the flows in two- and three-dimensional models of the carotid artery bifurcation are found, it is thought that the two-dimensional numerical analyses can contribute to the interpretation of the three-dimensional flow field and give a reliable picture of some important features as wall shear stress and reversal flow.

The most important shortcoming of the two-dimensional analysis seems to be the neglect of the secondary flow components, resulting in an overestimation of the magnitude and an underestimation of the cross-sectional extension of the reversed flow, especially in the distal part of the carotid artery sinus.

Influences and physiological relevance of a small stenosis in the carotid artery sinus.

From the computations of the flow in the two bifurcation geometries, it is concluded that the geometry variation does not lead to different flow characteristics for stenosed and non-stenosed geometries. The influence of the stenosis is most clearly expressed in the velocity downstream the stenosis, where especially at peak systolic flow rate, reversed flow and relatively large negative wall shear stresses are found. Furthermore, it is observed that the spatial and temporal oscillations of the wall shear stress at the distal part of the sinus are smaller in the case of a stenosed geometry, especially at the divider-side wall. This seems to be in contrast with the in-vivo pulsed Doppler observations made by Van Merode (1986) who mentioned an increased probability of the occurrence of flow reversal at the divider side-wall for stenosed geometries.

For two-dimensional geometries, it is hardly possible to distinguish between the influence of the stenosis and the influence of the geometry variation, and no striking deviations in flow characteristics are found. From this two-dimensional analysis it can be stated that the outlook for the usability of in-vivo measurements of the axial velocity for detection of minor stenoses is not very promising. However, fully three-dimensional analyses must be performed to obtain information needed to prove whether this statement is correct.

references.

- Batten J.R. and Nerem R.M.,'Model study of flow in curved and planar arterial bifurcations.', Cardiovasc. Res., 16, p 178-186 (1982).
- Bharadvaj B.K., Mabon R.F. and Giddens D.P.,'Steady flow in a model of the human carotid bifurcation. Part I - Flow visualization.', J. Biomech., 15, p 349-362 (1982).
- Bharadvaj B.K., Mabon R.F. and Giddens D.P.,'Steady flow in a model of the human carotid bifurcation. Part II - Laser-Doppler anemometer measurements.', J. Biomech., 15, p 363-378 (1982).

- Brech R. and Bellhouse B.J.,'Flow in branching vessels.', Cardiovasc. Res., 7, p 593-600 (1973).
- Clarck M.E., Robertson J.M. and Cheng L.C.,'Stenosis severity effects for unbalanced simple-pulsatile bifurcation flow.', J. Biomech., 16, p 895-906 (1983).
- Corver J.A.W.M., Van de Vosse F.N., Van Steenhoven A.A. and Reneman R.S.,'The influence of a small stenosis in the carotid artery bulb on adjacent axial velocity profiles.', In : Biomechanics: Current Interdisciplinary Research, Eds. Perren S.M. and Schneider E., p 239-244, Martinus Nijhoff Publ., Dordrecht (1985).
- Ehrlich L.W. and Friedman M.H.,'Particle paths and stasis in unsteady flow through a bifurcation.', J. Biomech., 10, p 561-568 (1977).
- Ferguson G.G. and Roach M.R.,'Flow conditions at bifurcations as determined in glass models, with reference to the focal distribution of vascular leasions.', In : Cardiovascular fluid dynamics 2, Ed. Berger D.H., p 141-156, Acad.Press., London (1972).
- Fernandez R.C., De Witt K.J. and Botwin M.R.,'Pulsatile flow through a bifurcation with applications to arterial disease.', J. Biomech., 9, p 575-580 (1976)
- Feuerstein I.A., El Masry O.A. and Round G.F.,'Arterial bifurcation flows - effects of flow rate and area ratio.', Can. J. Physiol. Pharmacol., 54, p 795-808 (1976).
- Florian H. and Perktold K.,'Finite element computer simulation of pulsatile flow in an arterial bifurcation.', Biomed. Techn., 27, p 79-84 (1982).
- Friedman M.H., O'Brien V. and Ehrlich L.W.,'Calculations of pulsatile flow through a branch.', Circ. Res. , 36, p 277-285 (1975).
- Friedman M.H. and Ehrlich L.W.,'Numerical simulation of aortic bifurcation flows: the effect of flow divider curvature.', J. Biomech., 17, p 881-888 (1984).
- Gruber K. and Perktold K.,'Strömungsverhalten für Stadien einer stenotischen Veränderung am Beispiel der arteria femoralis.', In : Monitoring in der Anaesthsiologie und Intensivmedizin., Eds. Bergmann H., Gilly H. Kenner T., Schuy S. and Steinberiethner K., p 321-332, Verlag Wilheim Maudrich, Wien (1983).

- Kandarpa K. and Davids N.,'Analysis of the fluid dynamic effects on atherogenesis at branching sites.', J. Biomech., 9, p 735-741 (1976).
- Karino T., Motomiya M. and Goldsmith H.L.,'Flow patterns in model and natural vessels.', In : Biologic and synthetic vascular prostheses, Ed. Stanley J.C., p 153-178, Grune & Straton,Inc. (1982).
- Kawaguti M. and Hamano A.,'Numerical study on bifurcation flow of viscous fluid'. J. Phys. Soc. Japan, 46, p 1360-1365 (1979).
- Ku D.N.,'Hemodynamics and atherogenesis at the human carotid bifurcation'. Ph.D. Thesis, Georgia Inst. Techn. (1983).
- Ku D.N. and Giddens D.P.,'Pulsatile flow in a model carotid bifurcation.', Arteriosclerosis, 3, p 31-39 (1983).
- Ku D.N., Gidens D.P., Phillips D.J. and Strandness D.E., 'Hemodynamics of the normal human carotid bifurcation: in vitro and in vivo studies.', Ultrasound. Med. Biol., 11, p 13-26 (1985).
- Liepsch D., Moravec S. and Zimmer R.,'Influence of the hemodynamic effect on vessel alterations (influence of blood flow in arteries on the formation of thromboses and stenoses).' Biomed. Techn., 26, p 115-122 (1981).
- Liepsch D., Moravec S., Rastogi A.K. and Vlachos N.S.,'Measurement and calculations of laminar flow in a ninety degree bifurcation.', J. Biomech., 15, p 473-485 (1982).
- LoGerfo F.W., Nowak M.D. Quist W.C. Crawshaw H.M. and Bharadvaj B.K.,'Flow studies in a model carotid bifurcation.', Arteriosclerosis, 1, p 235-241 (1981).
- Mark F.F., Bargeron C.B., Deters O,J, and Friedman M.H., 'Experimental investigations of steady and pulsatile laminar flow in a 90^{o} branch.', J. Appl. Mech., 44, p 372-377 (1977).
- Van Merode T.,'The use of a multi-gate pulsed Doppler system in the evaluation of the carotid artery circulation.', Thesis, University of Limburg, The Netherlands (1986).
- O'Brien V., Ehrlich L.W. and Friedman M.H.,'Unsteady flow in a branch.', J. Fluid Mech., 75, p 315-336 (1976).
- Olson D.E.,'Fluid mechanics relevant to respiration: flow within curved or elliptic tubes and bifurcation systems.', Ph.D. thesis, University of London (1971).

- Perktold K. and Gruber K.,'Teilchenbahnen in einem Modell eines gesunden und stenotisierten Beinarteriensegments.', In : Monitoring in der Anaesthsiologie und Intensivmedizin., Eds. Bergmann H., Gilly H. Kenner T., Schuy S. and Steinberiethner K., p 333-340, Verlag Wilheim Maudrich, Wien (1983).
- Perktold K. and Hilbert D.,'Numerical simulation of pulsatile flow in a carotid bifurcation model.', J. Biomed. Eng., 8, p 193-199 (1986).
- Reneman R.S., Van Merode T., Hick P. and Hoeks A.P.G.,'Flow velocity patterns in and distensibility of the carotid artery bulb in subjects of various ages.' Circulation, 71, p 500-509 (1985).
- Rindt C.C.M., Van de Vosse F.N., van Steenhoven A.A., Janssen J.D. and Reneman R.S.,'A numerical and experimental analysis of the flow field in a two-dimensional model of the human carotid artery bifurcation.', to be published in J. Biomech. (1987).
- Rodkiewicz C.M. and Roussel C.L.,'Fluid mechanics in a large arterial bifurcation.', J. Fluid Eng., 95, p 108-112 (1973).
- Siouffi M., Pelissier R., Farahifar D. and Rieu R.,'The effect of unsteadiness of the flow through stenoses and bifurcations'., J. Biomech., 17, p 299-315 (1984).
- Versteijlen J.A.M.,'Metingen aan een instationaire stroming in een drie-dimensionaal model van de halsslagader vertakking.', Report of University of Technology Eindhoven, (1985) (in Dutch).
- Walburn F.J. and Stein P.D.,'Velocity profiles in symmetrically branched tubes simulating the aortic bifurcation.', J. Biomech., 14, p 601-611 (1981).
- Wille S.Ø.,'Pressure and flow in two dimensional numerical bifurcation models.', Appl. Math. Modelling, 4, p 351-356 (1980).
- Wille S.Ø.,'Numerical simulations of steady flow inside a three dimensional aortic bifurcation model.' J. Biomed. Eng., 6, p 49-55 (1984).
- Zarins C.K., Giddens D.P., Bharadvaj B.K., Sottiurai V.S., Mabon R.F. and Glagov S.,'Carotid bifurcation atherosclerosis. Quantitative correlation of plaque localization with flow velocity profiles and wall shear stress.', Circ. Res., 53, p 502-514 (1983).

CHAPTER 5: STEADY ENTRANCE FLOW IN A CURVED TUBE.

5.1. Introduction.

In this chapter the steady entrance flow in a curved tube is dealt with. The analysis of this flow configuration may be viewed as a first step towards a fully three-dimensional calculation of carotid artery flow, which is impracticable on the computer systems used sofar (PRIME 750 and APOLLO DSP90) because of the large amount of computing time and memory needed. Moreover, as mentioned in the preceding chapter, the flow in the internal carotid artery exhibits properties that resemble the entrance flow in a curved tube. Consequently, the analysis of this flow configuration contributes to the understanding of carotid artery flow. Furthermore, the calculations of the flow in a curved tube form a non-trivial way to evaluate the finite element approximation for three-dimensional flow, including non-negligible secondary flow components.

If the Navier-Stokes equations are rewritten in an orthogonal curvilinear toroidal co-ordinate system (see Fig. 5.1), two important dimensionless parameters are found (Ward-Smith, 1982) :

the curvature ratio $\delta = a/R$ (5.1)

and

the Dean number $\kappa = Re\sqrt{\delta}$ (5.2)

with a the radius of the tube, R the curvature radius and Re the Reynolds number based on the diameter of the tube and the mean axial velocity (Re=WD/v). The Dean number can be interpreted as the ratio of the square root of the convective inertial forces times the centrifugal forces to the viscous forces, i.e. :

$$\kappa = \frac{\sqrt{(W^2/2a)(W^2/R)}}{\nu W/(4a^2)} \qquad (5.3)$$

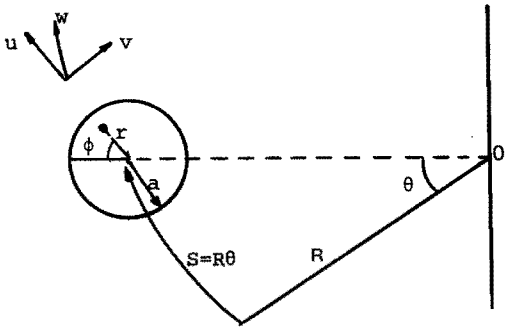

Fig. 5.1 : Toroidal co-ordinate system (r,φ,θ).

In this study a curvature ratio δ=1/6 is chosen. This value approximately corresponds with the curvature of the intermediate section between the common and internal carotid arteries. With Reynolds numbers in the range 100 < Re < 800 this leads to Dean numbers in the range 40 < κ < 330.

Experimental analyses in the range of δ and κ considered, using a uniform inlet flow profile, were made by Olson (1971), Agrawal et al. (1978), Choi et al. (1979) and Olson and Snyder (1983 and 1985). In the case of a uniform inlet flow, immediately downstream of the entry in the bend a secondary flow is set up, which is dominated by the build-up of an axial boundary layer. Further downstream, two helical vortices develop as a result of the interaction between convective, centrifugal and viscous forces. Considering laminar flow, a fully developed parabolic velocity profile is a more convenient inlet flow for several reasons. In contrast with a uniform inlet flow, fully developed inlet flow can be achieved more easily in an experimental set-up and is well defined. The importance of a well defined inlet flow is underlined by the observations made by Olson and Snyder (1985), who found a far downstream influence of the inlet condition. Furthermore, a fully developed inlet flow is more convenient for numerical analyses, since leading edge singularities are avoided. Finally, with respect to the modelling of the flow in the carotid artery, fully developed flow is more relevant because of the relatively long common carotid artery. As far as is known, the development from a parabolic entry velocity profile has only been

reported by Olson (1971), who presented the development of the axial velocity profiles in the plane of symmetry of the bend ($1/16<\delta<1/4.66$ and $45< \kappa<756$), and Bovendeerd et al. (1987), who presented both axial and secondary velocity distributions at several cross-sections ($\delta=1/6$ and $\kappa=286$). Numerical flow investigations have been carried out only for uniform inlet flows (Singh, 1974, Yao and Berger, 1975, Liu, 1976, Stewartson et al., 1980 and Soh and Berger, 1984). They used finite difference or analytical approximations, transforming the problem into toroidal co-ordinates.

In this chapter the results of a finite element approximation of the development from a parabolic entry velocity profile will be given. For one value of the Reynolds number (Re=300) the numerical results are compared with the results of laser-Doppler measurements. First, in section 5.2, the 27-noded brick element used will be dealt with. In order to make possible the extension of the numerical model to three-dimensional flow problems in bifurcation geometries, cartesian co-ordinates are used to formulate the numerical approximation. In section 5.3, the results of the calculations will be presented and compared with the results attained from the experiments. Only a global description will be given of the experimental method, for which the reader is referred to appendix 3 or Bovendeerd et al. (1987). Finally, in section 5.3, the results will be discussed and some concluding remarks will be made.

5.2. The 27-noded hexahedral (Q_2-P_1) element.

The finite element formulation as given in chapter 2 for two dimensions can readily be extended to three dimensions and yields the same set of equations when the matrix definitions given by (2.7) are extended to three dimensions. A survey of finite elements for the three-dimensional Navier-Stokes equations is given by Fortin(1981) and Fortin and Fortin ($1985^{a,b}$). Just as in the two-dimensional case, the Brezzi-Babuska condition and the applicability of a penalization formulation (i.e. a discontinuous pressure approximation) are of importance for the choice of an element. The simplest element, which is at least second order accurate and which satisfies the above mentioned conditions, is the full quadratic velocity - linear pressure ($Q_2^{(27)}$-P_1) element (see Fig. 5.2). Similar to the two-dimen-

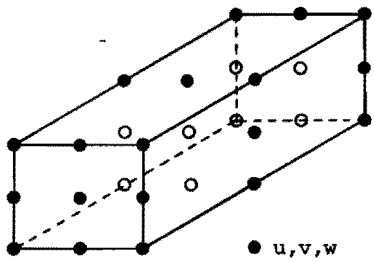

Fig. 5.2 : The 27-noded hexahedral (Q_2-P_1) element.

sional (P_2^+-P_1) element, the pressure is approximated by its value and its derivatives in the centroid of the element and thereby is discontinuous over the element boundary. The number of unknowns per element is 81 for the velocity and 4 for the pressure. Also here the velocity and the pressure derivatives in the centroid can be eliminated, reducing the number of unknowns per element from 85 to 79. This reduction is relatively less important than in the two-dimensional case. In literature only little experience with three-dimensional elements is reported. With respect to the (Q_2-P_1) element the following note can be made (Fortin and Fortin, 1985[a,b]) : since the pressure imposes only 4 constraints on the 81 degrees of freedom in velocity, the divergence-free condition can perhaps not be applied strongly enough and may lead to a too compressible element. Nevertheless, an $O(h^3)$ accuracy in the velocity approximation was found for a simple test example (Segal, 1986). Since the development of three-dimensional elements in the finite element code used (Segal and Praagman, 1985) was still in progress at the time when the study described here was performed, neither the elimination of the velocity and the pressure derivatives in the centroid nor the calculation of the pressure from the solution of the momentum equation with penalty function were available and hence here only approximations of the velocity distribution are given. In the next section the (Q_2-P_1) element will be applied to the flow in a 90-degree curved tube and the results will be compared with data obtained from laser-Doppler experiments. Although no predictions about the order of accuracy can be made, this flow configuration is thought to be complex enough for evaluation of the applicability of the element to complex three-dimensional flow problems.

5.3. Results.

The entrance flow in a curved tube with curvature ratio δ=1/6 was calculated for Re=100, 300 and 500 (κ≈41, 122 and 204). To this end a finite element mesh was generated as depicted in Fig. 5.3. Upstream of the entrance (θ=0) and downstream of the exit ($\theta=\pi/2$) of the 90^{o}-bend, an in and an outlet section with a length of twice the tube diameter were used. A parabolic velocity distribution was imposed as inflow condition, whereas stress-free outflow conditions were used.

Experiments were performed in a perspex model with an internal radius of 4mm and a curvature radius of 24mm (δ=1/6). The outer surfaces of the model were chosen in such a way that the three velocity components were measured with the optical axis of the employed laser-Doppler anemometer perpendicular to the outer surface (see appendix 3 or Bovendeerd, 1987). A long inlet section of 0.4m ensured a fully developed parabolic flow at the entrance of the bend. Also downstream the bend a long straight glass pipe was present. The Reynolds number of the flow was kept at Re=300 (κ=122). The velocity components were measured at 5 cross-sections in the bend (θ=0 (π/8) π/2) corresponding with the element boundaries in the finite element mesh (see Fig. 5.3). For a more detailed description of the measurement procedure the reader is referred to appendix 3.

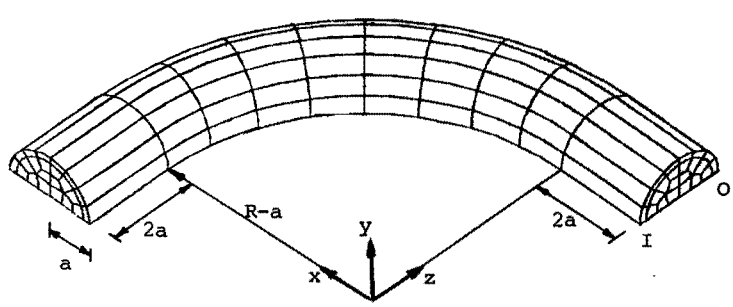

Fig. 5.3 : Geometry and finite element mesh as used in the calculations (220 elements, 2205 nodes).

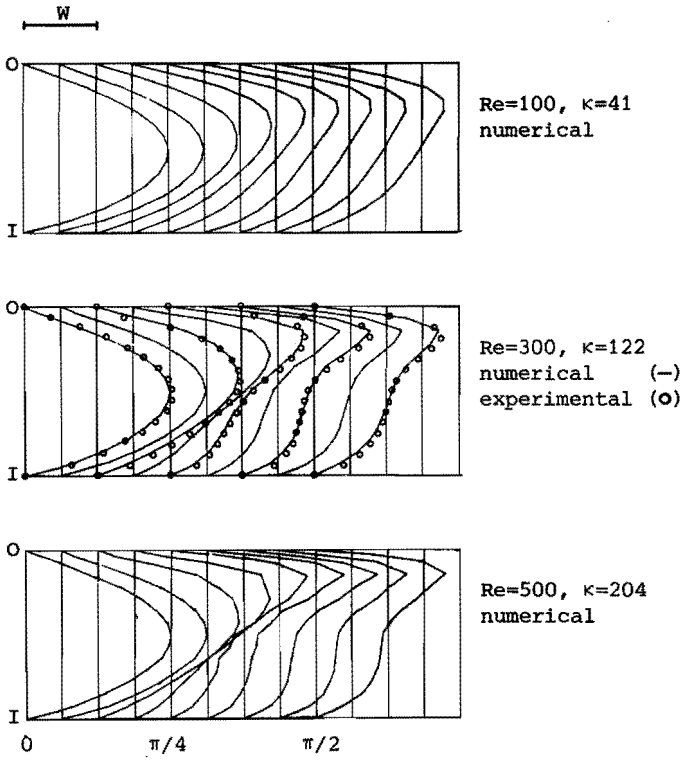

Fig. 5.4 : Axial velocity in the plane of symmetry of the curved tube (δ=1/6) as calculated for Re=100, 300 and 500 (κ=41, 122 and 204) and measured (o) for Re=300 (κ=122).

Axial velocities.

In Fig. 5.4 the development of the axial velocity in the plane of symmetry is given for Re=100, 300 and 500. Moreover the measured values of the axial velocity at Re=300 are given and indicated by circles. At the first two velocity profiles (θ=0 and θ=π/16) hardly any influence of the curvature is visible, although a slight shift towards the inner bend is observable at θ=0. Further downstream, the maximum of the axial velocity profile is shifted towards the outer bend. At higher Reynolds numbers this shift is more pronounced and a plateau in the profiles develops near the inner bend. Only at Re=100, the flow seems to be fully developed at θ=π/2. Despite an overall

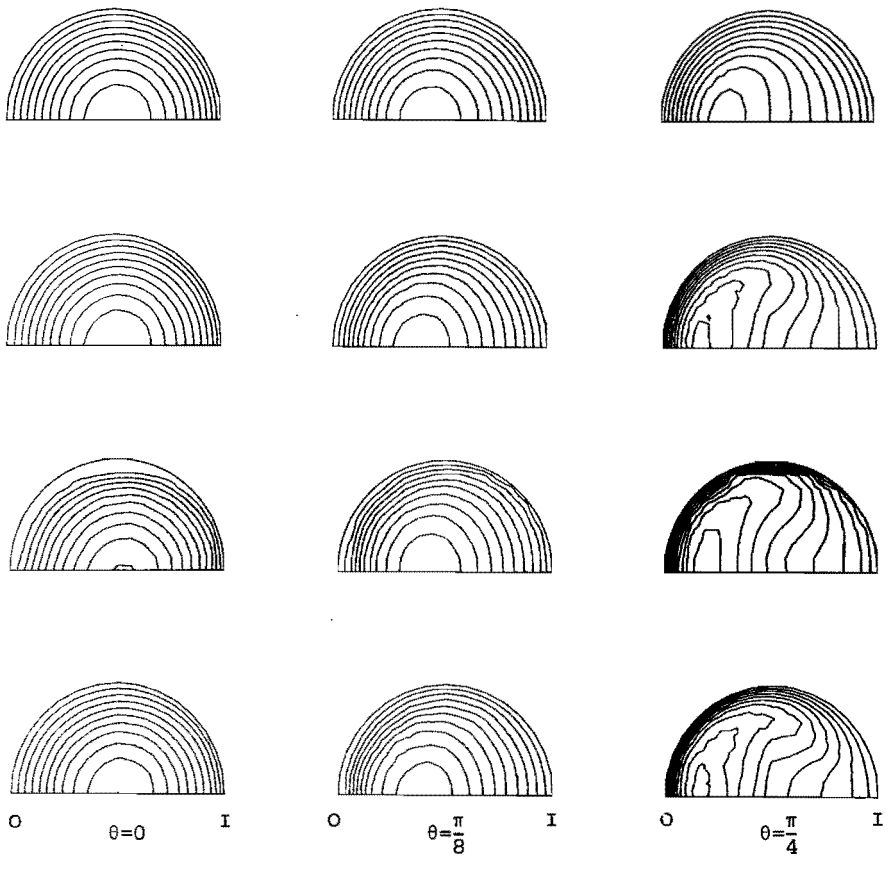

Fig. 5.5 : Isovelocity contours (level difference $\Delta w/W=0.2$) of the axial velocity in the curved tube ($\delta=1/6$) as calculated for Re=100, 300 and 500 ($\kappa=41$, 122 and 204) and measured for Re=300 ($\kappa=122$).

over-estimation of the axial velocity (probably due to a measurement inaccuracy of the imposed flow value) the calculations agree well with the experiments at all cross-sections.

In Fig. 5.5 , a more complete picture of the axial flow development is given. Here the axial velocity distribution is given by isovelocity contours at several cross-sections in the tube. An almost parabolic axial velocity distribution is observed at $\theta=0$. This paraboloid, however, is shifted slightly towards the inner bend. The experimental isovelocity contours at this axial position show a shift from the 'upper' wall, probably due to the inaccuracy in the determi-

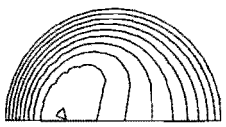

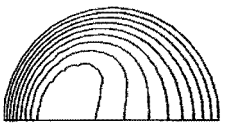

Re=100, κ=41
numerical

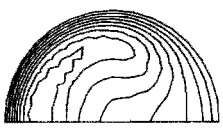

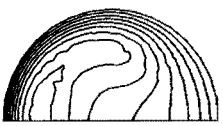

Re=300, κ=122
numerical

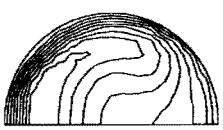

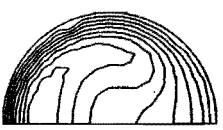

Re=300, κ=122
experimental

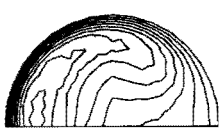

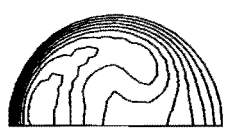

Re=500, κ=204
numerical

nation of the wall position. At $\theta=\pi/8$ the isovelocity contours shift towards the outer bend of the tube and no significant deviation is found for the different Reynolds numbers. Halfway the bend ($\theta=\pi/4$) the shift towards the outer bend has continued and large wall shear rates occur at the outer bend of the tube. At higher Reynolds number flow, a 'C-shaped' isovelocity contour is found for the high velocity region. At the cross-sections $\theta=3\pi/8$ and $\theta=\pi/2$, the 'C-shaped' contours further develop and for Re=100 at first sight an almost fully developed axial velocity distribution is found. The agreement between the experiments and the calculations at Re=300 is fair.

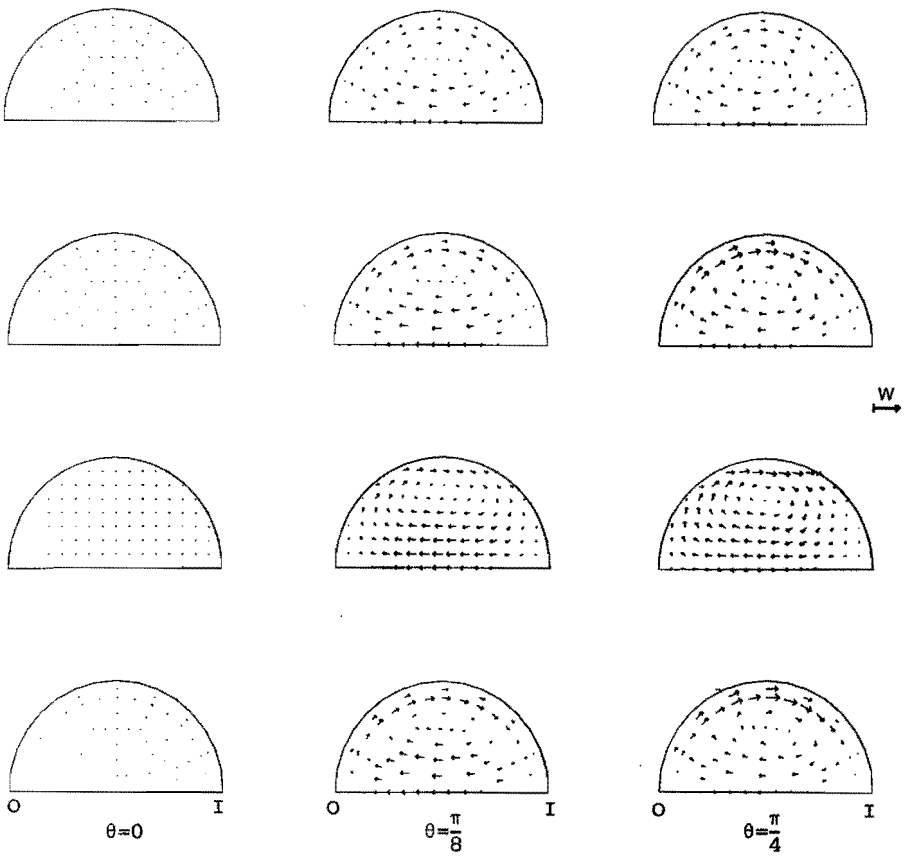

Fig. 5.6 : Normalized secondary velocity vectors in the curved tube (δ=1/6) as calculated for Re=100, 300 and 500 (κ=41, 122 and 204) and measured for Re=300 (κ=122).

Secondary velocities.

In Fig. 5.6 the development of the secondary velocity field is given for Re=100, 300 and 500, respectively. These velocities are normalized with respect to the mean axial velocity W. At the entrance (θ=0) the upstream influence of the bend is visible in a unidirectional secondary flow from the outer bend towards the inner bend, which amounts to about 5% of the mean axial flow. The same upstream influence of the bend was found in the experiments. At $\theta=\pi/8$ a vortex has developed which near the plane of symmetry is directed from the

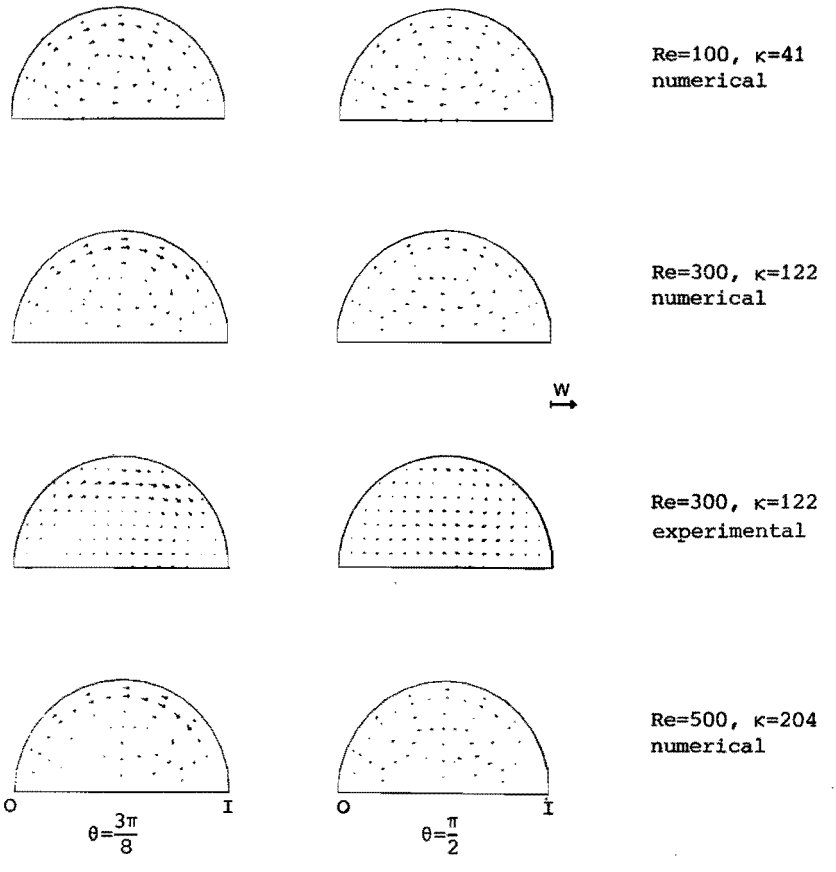

inner bend towards the outer bend and at the upper wall from the outer bend back to the inner bend. The center of this vortex is approximately located at (x/a=0, y/a=0.65). Hardly any influence of the Reynolds number on the shape of the vortex is observable at this axial location. However, the normalized secondary velocity components are larger at the higher Reynolds numbers. Although direct comparison with the experiments is difficult because of the different locations at which the velocities are determined, good agreement is found at this axial station. At θ=π/4, the layer with circumferential flow along the upper wall has intensified, especially at the higher Reynolds number flows. Near the plane of symmetry the secondary velocities are found to be slightly lower than at θ=π/8. For Re=500,

a shift of the vortex center towards the inner bend is found. Also at this axial station the experiments agree well with the calculations although in the experimental case the center of the vortex is observed to be located somewhat closer to the upper wall. Next, at $\theta=3\pi/8$, the influence of the Reynolds number on the secondary flow field is clearly visible. For the low Reynolds number case (Re=100), the vortex found has approximately the same shape and strength as those found at the two axial locations upstream. For Re=300 and Re=500, however, the secondary velocities are significantly lower, especially near the plane of symmetry. The center of the vortex has moved further in the inner bend direction while, moreover, a deformation of the shape of the vortex has taken place. A similar behaviour is found in the experiments. At $\theta=\pi/2$, the same characteristics are found but also an extra outer bend directed fluid motion is observed, superimposed on the vortex flow. The same phenomenon is found experimentally.

More quantitative but less detailed information of the secondary flow field can be obtained from the circulation Γ or the mean axial vorticity ξ_c:

$$\xi_c = \Gamma/A = \oint_S \vec{u} \cdot d\vec{s} \; / \; A \tag{5.3}$$

with S a path along the plane of symmetry and the upper tube wall, surrounding a surface A ($= \pi a^2/2$). Following Olson and Snyder's procedure (Olson and Snyder, 1985), this quantity is best used in the form:

$$\xi_c' = \frac{\xi_c a}{W} \delta^{3/2} \tag{5.4}$$

In Fig. 5.7 the dimensionless mean axial vorticity ξ_c' is plotted as a function of θ/δ. Due to the overall flow to the inner bend at $\theta=0$, the curves start at negative values. Then a large increase is found coinciding with the development of the secondary vortex. For the higher Reynolds numbers this increase is larger but also reaches its maximum at smaller angles θ. Hereafter, the circulation decreases again to a value which is smaller for larger Reynolds numbers. The upstream effect of the straight outflow tube is expressed in a sudden

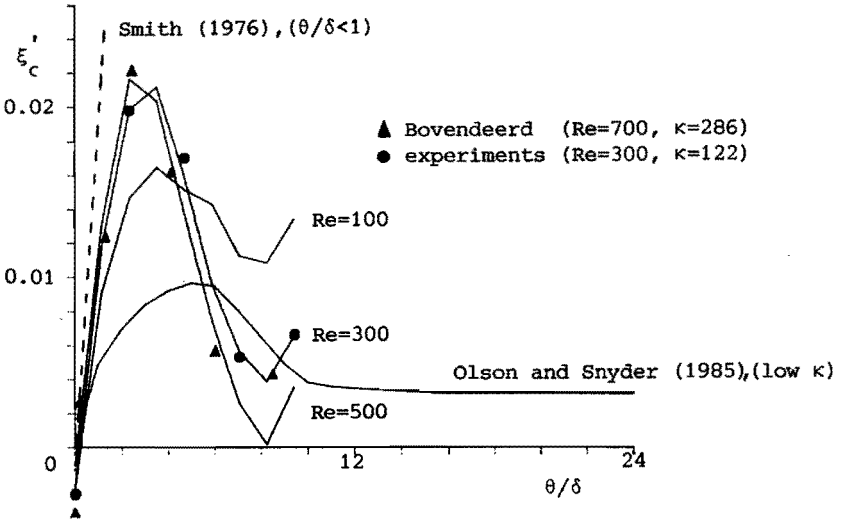

Fig. 5.7 : The dimensionless mean axial vorticity in the curved tube (δ=1/6) as a function of θ/δ as calculated for Re=100, 300 and 500 (κ=41, 122 and 204) and measured for Re=300 (κ=122) together with the results of Smith (1976), Olson and Snyder (1985) and Bovendeerd et al. (1987).

increase of the circulation. Although the axial and secondary velocity distributions suggest that the flow at Re=100 seems to be fully developed at θ=π/4, the mean axial vorticity curve in Fig. 5.7 does not reach an asymptotic value. The mean axial vorticity as calculated from the experimental data completely agrees with the numerically obtained results.

5.4. Discussion.

In the preceding section the results of calculations of the entrance flow in a curved tube have been presented by means of the axial and secondary velocity distributions. The results of the calculations for Re=300 agree well with the experimental results. Combining the information separately described in the preceding section, the following remarks are made. At θ=0 the secondary flow is directed towards the inner bend and also the maximum of the axial velocity is shifted slightly in this direction, both pointing to an upstream

influence of the bend. The same upstream influence is found in the experiments. At $\theta=\pi/8$ the flow experiences the interaction of convective inertial, viscous and centrifugal forces (cf. Berger et al., 1983). In the central core of the tube, where the axial velocities are large, the centrifugal force dominates resulting in a secondary flow towards the outer bend. Near the walls of the tube the centrifugal forces are less important and a circumferential back flow to the inner wall is found. In consequence of this phenomenon the maximum of the axial velocity shifts towards the outer bend. In accordance with the analytical approximation for $\theta/\delta<1$ made by Smith (1976), this initial behaviour is nearly independent of the Reynolds number. The initial increase of the circulation found here agrees quite well with the solution of Smith (see Fig. 5.7). At $\theta=\pi/4$, the influence of the secondary motion as described above is clearly visible in the axial velocity distribution. The maximum of the axial velocity is convected further to the outer bend. At higher Reynolds numbers, where the convective terms are more important, 'C-shaped' axial isovelocity contours are found in accordance with the observations of, for instance, Agrawal et al. (1978) and Olson and Snyder (1985). At the next axial station ($\theta=3\pi/8$) the dependence on the Reynolds number becomes even more clear. For Re=100, the velocity distribution does not differ much from the one found at the preceding axial location and an almost fully developed flow is found. For the higher Reynolds numbers (Re=300, 500) the 'C-shaped' axial velocity profiles have become more pronounced. Furthermore, the secondary fluid motion is mainly restricted to a small boundary layer along the upper wall of the bend. Similar Reynolds-dependence is reported by Soh and Berger (1984). Finally, at $\theta=\pi/2$ the velocity distribution is strongly influenced by the upstream influence of the straight outflow region of the model. Here, the secondary velocity distribution is characterized by an increase of the velocity component towards the outer bend ; a reversed effect as found at the entrance region of the bend. As seen in Fig. 5.7 this increase does not conform with the general observations ($100<\kappa<500$, $4.66<1/\delta<8$) made by Olson and Snyder (1985) for a 300-degrees bend, enabling the flow to get fully developed. The mean axial vorticity distribution found indicates that at small angles θ the increase of the axial vorticity is nearly Reynolds-independent. The initial axial vorticity values agree with

the solution of Smith (1976). With increasing Reynolds number, the maximum axial vorticity increases and, furthermore, is reached at smaller axial positions. The experiments of Bovendeerd et al. (1987) and the observations made by Olson and Snyder (1985) confirm this observation.

With respect to the applicability of the numerical model to three-dimensional flow problems, the following remarks are made. The agreement between the experimental and numerical results indicates that the finite element method applied offers an accurate tool for three-dimensional flow simulations. Although a relatively coarse mesh was used and although the amount of the pressure unknowns, and thus of the constraints for divergence freedom (4), is small compared with that of the velocity (84), the results seem to be quite accurate. At Re=500, however, the solution becomes slightly wiggling (see Fig. 5.5) and for higher Reynolds numbers (Re=700) the solution procedure failed to converge at all, so finer meshes should be applied in that case. For the finite element mesh applied here, about 25 hours CPU and about 2 days I/O were needed per Newton iteration (11 Newton iterations were needed to reach Re=500) on a mini-computer (APOLLO DSP90). Therefore, application of this solution procedure for three-dimensional bifurcation models demands more sophisticated computer capacity, like array processing or super-computers.

references.

- Agrawal Y., Talbot L. and Gong K.,'Laser anemometer study of flow development in curved circular pipes.', J. Fluid Mech., 85, p 497-518 (1978).
- Bovendeerd P.H.M., Van Steenhoven A.A., Van de Vosse F.N. and Vossers G.,'Steady entry flow in a curved pipe.', to be published in : J. Fluid Mech. (1987).
- Berger S.A., Talbot L. and Yao L.S.,'Flow in curved pipes.', Ann. Rev. Fluid Mech., 15, p 461-512 (1983).
- Fortin M.,'Old and new finite elements for incompressible flows.', Int. J. Num. Meth. Fluids., 1, p 347-364 (1981).

- Fortin M. and Fortin A.,'Newer and newer elements for incompressible flow.', in : Finite elements in Fluids vol. 6, Eds. Gallagher R.H., Caray G.F., Oden J.T. and Zienkiewicz O.C., John Wiley & Sons Ltd. (1985).
- Fortin M. and Fortin A.,'Experiments with several elements for viscous incompressible flows.', Int. J. Num. Meth. Fluids., 5, p 911-928 (1985).
- Liu N.S.,'Developing flow in a curved pipe.', INSERM-Euromech 92, 71, p 53-64 (1977).
- Olson D.E.,'Fluid mechanics relevant to respiration: flow within curved or elliptical tubes and bifurcating systems.', Ph.D. Thesis, University of London (1971).
- Olson D.E. and Snyder B.,'The growth of swirl in curved circular pipes.', Phys. Fluids, 56, p 347-349 (1983).
- Olson D.E. and Snyder B.,'The upstream scale of flow development in curved circular pipes.', J. Fluid Mech., 150, p 139-158 (1985).
- Segal A.,'Test problem for the ($Q_2^{(27)}$-P_1) element.' (personal communication) (1986).
- Singh M.P.,'Entry flow in a curved pipe.', J. Fluid Mech. , 65, p 517-539 (1974).
- Smith F.T.,'Fluid flow into a curved pipe.', Proc. R. Soc. London Ser. A 351, p 71-87 (1976).
- Soh W.Y. and Berger S.A.,'Laminar entrance flow in a curved tube.', J. Fluid Mech. , 148, p 109-135 (1984).
- Stewartson K., Cebeci T. and Chang K.C.,'A boundary-layer collision in a curved duct.', Q. J. Mech. Appl. Math., 33, p 59-75 (1980).
- Yao L.S. and Berger S.A.,'Entry flow in a curved pipe.', J. Fluid Mech., 67, p 177-196 (1975).
- Ward-Smith A.J.,'Internal fluid flow.', Clarendon Press Oxford (1982).

CHAPTER 6: SUMMARY AND CONCLUSIONS.

In the present study a finite element model for incompressible Newtonian flow and its application to the modelling of carotid artery flow is analyzed. Moreover, the numerical model has been validated experimentally for several flow configurations.

The penalty function finite element method employed, proved to be well suitable for spatial discretization of the two-dimensional steady and unsteady Navier-Stokes equations. The $(P_2^+-P_1)$ Crouzeix-Raviart element used has a third order accuracy for the velocity and second order of accuracy for the pressure. Next, a second order modified Crank-Nicolson time integration scheme has been derived. This scheme is found to be free of numerically generated oscillations, as may occur in a standard Crank-Nicolson time integration. Moreover, this scheme is to be preferred above the first order Euler implicit scheme, which may lead to an incorrect damping of flow oscillations which may occur in flows with dominating convective properties. The theoretical results mentioned above have been confirmed by computations of oscillatory flow between two flat plates and Von Karman vortex shedding behind a circular cylinder.

From the analysis of the steady flow over a square step it is found that stress-free outflow conditions exhibit less upstream influence than fully developed outflow conditions and therefore make possible a significant reduction of the computational domain at outflow sites. Similar to the flow over backward-facing steps, a recirculation zone downstream of the step is found with a length almost proportional to the Reynolds number of the flow. The axial velocity profiles, as calculated for the steady flow over a square step, agree with those obtained from laser-Doppler experiments. The flow instabilities observed in the experiments, however, could not be simulated satisfactorily by solving the time-dependent Navier-Stokes equations. It is not clear yet whether further mesh refinement and smaller timesteps are needed, or that the three-dimensional effects in the experiments have to be taken into account to simulate the flow instabilities numerically.

The unsteady flow over a square step completely differs from the steady flow situation. Reversed flow regions, strongly depending on the instantaneous flow rate, have been found at both the step-side wall and the non-step-side wall of the channel. Quasi static modelling is only valuable at the end of the diastolic phase of the cardiac cycle. With respect to the comparison with the experimental data, the influence of the three-dimensionality and instabilities in the experiments is even more confusing than in the steady flow analysis, and only qualitative agreement between the experiments and the calculations has been found.

From the experimental validation of the computation of the pulsatile flow in a two-dimensional bifurcation model, it is concluded that the numerical model used provides an accurate approximation of the spatial and temporal velocity distributions. In general the pulsatile flow in two-dimensional bifurcation models can be characterized as follows. Reversed flow regions are observed at the non-divider-side walls of both the internal and external carotid arteries. Due to the larger flow rate and the presence of the sinus, the axial and cross-sectional extents of the reversed flow region in the internal carotid artery are larger than in the external carotid artery. The unsteadiness of the flow is accompanied by rather complex spatial and temporal velocity distributions and leads to temporal variations of the location and length of the reversed flow regions. In consequence, strong spatial and temporal variations of the wall shear stress are found. At the non-divider-side walls the wall shear stress is relatively low and exhibits an oscillatory behaviour in space and time. At the divider-side walls the wall shear stress is relatively large and approximately follows the flow rate distribution in time.

Comparing the calculated two-dimensional velocity profiles with those from three-dimensional experiments, it is observed that in the common carotid artery and in the proximal parts of the internal and external carotid arteries the two-dimensional numerical model provides valuable information with respect to the three-dimensional configuration. In the more distal part of especially the internal carotid artery, deviations are found between the results of the two-dimensional numerical model and those of the three-dimensional experimental model. These deviations can mainly be attributed to the

neglect of the secondary velocity distribution in the two-dimensional model. Besides, a relatively good qualitative agreement is found between the calculated axial wall shear stress distribution and experimental data obtained from a three-dimensional experimental model (Ku, 1983). In the two-dimensional numerical model the influence of a minor stenosis in the internal carotid artery is hardly distinguishable from a minor geometry variation. Fully three-dimensional analyses of the influence of minor stenoses are needed to prove numerically that in-vivo measurements of the axial velocity distribution are useful in the detection of minor stenoses.

Finally, as a first step towards fully three-dimensional calculation of carotid artery flow, the steady entrance flow in a curved tube has been analyzed (δ=1/6, 100<Re<500, 41<κ<204). The calculations of both the axial and secondary velocity distributions for Re=300 (κ=122) agree well with the experimental results obtained from laser-Doppler anemometry and indicate that the finite element model applied offers an accurate tool for three-dimensional flow analyses. For higher Reynolds numbers (Re=700), however, the solution procedure failed to converge, and less coarse finite element meshes should be applied. Also the application of the solution procedure to three-dimensional bifurcation models would require finer mesh distributions and would take the calculations beyond the reach of mini-computers used until now. More sohisticated computer capacity like array processing or super-computers are needed here. For further development of the numerical method, reformulation of the numerical problem into a form to which iterative solution procedures, like the (pre-conditioned) conjugated gradient methods (Axelsson and Barker, 1984 and Meijerink and Van der Vorst, 1977), can be applied, can offer some advantages with respect to this aspect. Because of the small penalty parameter introduced, these iterative solution procedures are expected to converge too slowly for the penalization formulation used in the present study. Pressure-correction schemes, as successfully applied in finite difference approximations (Chorin, 1968, Van Kan, 1985), seem to be quite suitable, but in the formulations developed until now for finite element methods (Donea et al., 1982 and Mizukami and Tsuchiya, 1984), difficulties are encountered in correctly incorporating the inverse of the mass-matrix.

references.

- Axelsson O. and Barker V.A.,'Finite element solution of boundary value problems.', Academic Press inc., New York (1984).
- Chorin A.J.,'Numerical solution of the Navier-Stokes equations.', Math. Comp., 22, p 745-762 (1968).
- Donea J., Giuliani S., Laval H. and Quartapelle L.,'Finite element solution of the unsteady Navier-Stokes equations by a fractional step method.', Comp. Meth. Appl. Mech. Eng., 30, p 53-73 (1982).
- Van Kan J.,'A second-order pressure correction method for viscous incompressible flow.', SIAM J. Sci. Stat. Comp., 7, p 870-891 (1986).
- Ku D.N.,'Hemodynamics and atherogenesis at the human carotid bifurcation.', Ph.D. Thesis, Georgia Inst. Techn. (1983).
- Meijerink J.A. and Van de Vorst H.A.,'An iterative solution method for systems of which the coefficient matrix is a symmetric M-matrix.', Math. Comp., 31, p 148-162 (1977).
- Mizukami A. and Tsuchiya M.,'A finite element method for the three-dimensional non-steady Navier-Stokes equations.', Int. J. Num. Meth. Fluids, 4, p 349-357 (1984).

APPENDIX 1: Finite element formulation of the (Navier)-Stokes equations.

A1.1 : Variational formulation of the Navier-Stokes equations.

For completeness, in this appendix a brief description of the variational formulation of the Navier-Stokes equations is given. Consider the unsteady Navier-Stokes equations in D dimensions (D=2,3) in cartesian coordinates (see chapter 2):

$$\left|\begin{array}{ll} \varrho\dfrac{\partial u_i}{\partial t} + \varrho \sum_j u_j \dfrac{\partial u_i}{\partial x_j} = \varrho f_i + \sum_j \dfrac{\partial \sigma_{ij}}{\partial x_j} & \text{on } \Omega \\ \sum_j \dfrac{\partial u_j}{\partial x_j} = 0 & \text{on } \Omega \end{array}\right.$$

with boundary conditions :

$$u_i = 0 \qquad \text{on } \Gamma \qquad 1 \leq i \leq D$$

and initial condition :

$$u_i(0) = u_{i0} \qquad \text{on } \Omega \qquad 1 \leq i \leq D \qquad \text{(A1.1)}$$

where $\vec{f}$ and $\vec{u}_0$ are prescribed functions, and Ω denotes a bounded domain in $\mathbb{R}^D$ with a Lipschitz continuous boundary Γ.

To formulate a weak form of (A1.1) the Hilbert space $L^2(\Omega)$ and the first order Sobolev space $H^1(\Omega)$ are introduced and defined as :

$$L^2(\Omega) = \{ v \mid \int_\Omega v^2 d\Omega < \infty \}$$

with inner product : $(u,v) = \int_\Omega u\, v\, d\Omega$

and norm : $\|v\|_{L^2} = (v,v)^{1/2}$

$$H^1(\Omega) = \{ v \mid v \in L^2(\Omega),\ \frac{\partial v}{\partial x_i} \in L^2(\Omega),\ i=1,\ldots,D\}$$

with inner product : $(u,v)_{H^1} = (u,v) + \sum_i (\frac{\partial u}{\partial x_i}, \frac{\partial v}{\partial x_i})$

and norm : $$||v||_{H^1} = (v,v)_{H^1}^{1/2} \qquad \text{(A1.2)}$$

Let the space V be a Sobolev space of functions satisfying the homogeneous boundary conditions ,i.e. $V=(H_0^1(\Omega))^D$, with $H_0^1(\Omega)=\{v \mid v \in H^1(\Omega), v|_\Gamma = 0\}$. Furthermore let Q be the space of square integrable functions $Q=\{q \mid q \in L^2(\Omega)\}$. The weak form of (A1.1) is obtained by taking the inner product of the momentum equation with a function $\vec{v} \in V$ and the inner product of the continuity equation with a function $q \in Q$. After applying Green's formula this yields :

Find a pair $(\vec{u},p) \in V \times Q$ satisfying the initial condition such that :

$$\left|\begin{array}{ll}
\int_\Omega \rho \frac{\partial u_i}{\partial t} v_i d\Omega + \int_\Omega \sum_j \eta \left(\frac{\partial u_i}{\partial x_j} + \frac{\partial u_j}{\partial x_i} \right) \frac{\partial v_i}{\partial x_j} d\Omega - \int_\Omega p \frac{\partial v_i}{\partial x_i} d\Omega + & \\
\quad + \int_\Omega \rho \sum_j u_j \frac{\partial u_i}{\partial x_j} v_i d\Omega = \int_\Omega \rho f_i v_i d\Omega & \forall v_i \in H_0^1(\Omega) \\
- \int_\Omega \sum_j \frac{\partial u_j}{\partial x_j} q d\Omega = 0 & \forall q \in L^2(\Omega) \\
u_i(t=t_0) = u_{i0} \quad \text{on } \Omega & 1 \le i \le D\ , \\
& 1 \le j \le D \qquad \text{(A1.3)}
\end{array}\right.$$

Together with the definitions :

$$\langle \rho \frac{\partial \vec{u}}{\partial t}, \vec{v} \rangle = \sum_i \int_\Omega \rho \frac{\partial u_i}{\partial t} v_i d\Omega$$

$$a(\vec{u},\vec{v}) = \sum_{i,j} \int_{\Omega} \eta \left(\frac{\partial u_i}{\partial x_j} + \frac{\partial u_j}{\partial x_i} \right) \frac{\partial v_i}{\partial x_j} \, d\Omega$$

$$b(\vec{v},q) = - \int_{\Omega} \sum_{j} \frac{\partial v_j}{\partial x_j} \, q \, d\Omega$$

$$c(\vec{w},\vec{u},\vec{v}) = \sum_{i,j} \int_{\Omega} \varrho w_j \frac{\partial u_i}{\partial x_j} v_i \, d\Omega$$

$$\langle \vec{I},\vec{v} \rangle = \sum_{i} \int_{\Omega} \varrho f_i v_i \, d\Omega \qquad \text{(A1.4)}$$

this leads to :

Find a pair $(\vec{u},p) \in V \times Q$ such that :

$$\left| \begin{array}{l} \left\langle \varrho \dfrac{\partial \vec{u}}{\partial t}, \vec{v} \right\rangle + a(\vec{u},\vec{v}) + b(\vec{v},p) + c(\vec{u},\vec{u},\vec{v}) = \langle \vec{I},\vec{v} \rangle \\ \\ b(\vec{u},q) = 0 \end{array} \right. \qquad \text{(A1.5)}$$

Boundary conditions different from homogeneous Dirichlet boundary conditions as imposed in (A1.1) give variational problems which are similar to (A1.5). Inhomogeneous Dirichlet boundary conditions lead to an extension of the right hand side $\langle \vec{I},\vec{v} \rangle$ and a continuity equation given as $b(\vec{u},q)=\langle \vec{\gamma},q \rangle$ in which $\vec{\gamma}$ is a given function. Prescription of normal and/or tangential stresses give rise to an extension of the right hand side $\langle \vec{I},\vec{v} \rangle$ which incorporates the boundary integrals resulting from the application of Green's formula. A more extended treatment of the incorporation of boundary conditions is given in Cuvelier et al. (1986).

In the next section, variational problems as given by (A1.5) are treated and conditions for existence and uniqueness of its solution are given.

A1.2. Existence and uniqueness of solutions of the (Navier)-Stokes equations.

This section is a short summary of the existence and uniqueness results for saddle-point problems in general. Proofs of these results are to be found in the studies of Brezzi (1974) and Girault and Raviart (1979). The results are well adapted to study the solution of the steady Stokes equations and form an important framework for the construction of finite elements for these equations. From (A1.5) it is seen that they can be written in the following variational formulation :

Find a pair $(\vec{u},p)\in V\times Q$ such that :

$$\left|\begin{array}{lll} a(\vec{u},\vec{v}) + b(\vec{v},p) = \langle \vec{l},\vec{v}\rangle & & \forall \vec{v}\in V \\ b(\vec{u},q) = \langle \gamma,q\rangle & & \forall q\in Q \end{array}\right. \qquad \text{(A1.6)}$$

In order to find necessary and sufficient conditions for the problem to be well posed, a new space $V_\gamma \subset V$ is introduced as :

$$V_\gamma = \{\vec{v}\in V \mid b(\vec{v},q)=\langle \gamma,q\rangle, \forall q\in Q\} \qquad \text{(A1.7)}$$

Furthermore V_0 is defined as :

$$V_0 = \{\vec{v}\in V \mid b(\vec{v},q)=0, \forall q\in Q\} \qquad \text{(A1.8)}$$

Now with problem (A1.6) the following problem can be associated :

Find $\vec{u}\in V_\gamma$ such that :

$$a(\vec{u},\vec{v}) = \langle \vec{l},\vec{v}\rangle \qquad \forall \vec{v}\in V_0 \qquad \text{(A1.9)}$$

If the following hypotheses are assumed :

i) a is V_0-coercive, i.e. :

$$\exists_{\alpha>0} \; \forall_{\vec{v}\in V_0} \; a(\vec{v},\vec{v}) \geq \alpha \|\vec{v}\|_V^2 \qquad \text{(A1.10)}$$

ii) b satisfies the inf-sup condition :

$$\exists_{\beta>0} \; \inf_{q\in Q} \sup_{\vec{v}\in V} \frac{b(\vec{v},q)}{\|v\|_V \|q\|_Q} \geq \beta \qquad \text{(A1.11)}$$

then problem (A1.6) has a unique solution $(\vec{u},p)\in V\times Q$ (Girault and Raviart, 1979). The V_0-coerciveness is needed to ensure that problem (A1.9) has a unique solution $\vec{u}\in V_\gamma$ provided that $V_\gamma \neq \emptyset$. The inf-sup condition (or Brezzi-Babuska condition, Brezzi, 1974) implies that $V_\gamma \neq \emptyset$ and ensures that a solution $\vec{u}\in V_\gamma$ of (A1.9) leads to a unique solution $p\in Q$ of :

$$b(\vec{v},p) = \langle \vec{l},\vec{v}\rangle - a(\vec{u},\vec{v}) \qquad \forall \vec{v}\in V \qquad \text{(A1.12)}$$

In case of the Stokes equations (i.e. a and b are given as in (A1.4)) it can be proved (Temam, 1974, Girault and Raviart, 1979) that the V_0-coerciveness of a as well as the inf-sup condition hold and that therefore the Stokes problem as formulated in the previous section is well posed.

For non-linear problems (Navier-Stokes equations) an analysis as given in this section is much more complicated and the reader is referred to the studies of Temam (1974) or Girault and Raviart (1979). In general the uniqueness of a solution of the Navier-Stokes problem can only be proved for viscosities which are 'sufficient' large and body forces which are 'sufficient' small. However, the inf-sup condition still must hold to ensure a unique solution $p\in Q$ for each solution $\vec{u}\in V_\gamma$.

A1.3. Existence and uniqueness of the approximated solutions of (Navier-)Stokes equations.

In order to approximate the solution of the variational problem (A1.6), two finite dimensional spaces $V^h\subset V$ and $Q^h\subset Q$ are defined. Problem (A1.6) then can be approximated by :

Find a pair $(\vec{u}^h,p^h)\epsilon V^h x Q^h$ such that :

$$\left|\begin{array}{ll} a(\vec{u}^h,\vec{v}^h) + b(\vec{v}^h,p^h) = \langle \vec{f},\vec{v}^h\rangle & \forall \vec{v}^h\epsilon V^h \\ b(\vec{u}^h,q^h) = \langle \gamma,q^h\rangle & \forall q^h\epsilon Q^h \end{array}\right. \qquad \text{(A1.13)}$$

in which h is a discretisation parameter tending to zero.

Similar to the continuous case, the spaces $V^h_\gamma \subset V^h$ and $V^h_0 \subset V^h$ are defined as :

$$V^h_\gamma = \{\vec{v}^h\epsilon V^h \mid b(\vec{v}^h,q^h)=\langle \gamma,q^h\rangle, \forall q^h\epsilon Q^h\} \qquad \text{(A1.14)}$$

$$V^h_0 = \{\vec{v}^h\epsilon V^h \mid b(\vec{v}^h,q^h)=0, \forall q^h\epsilon Q^h\} \qquad \text{(A1.15)}$$

Since $Q^h \subset Q \neq \emptyset$ in general, $V^h_\gamma \not\subset V$ and $V^h_0 \not\subset V$ in general.

The discrete analogue of (A1.10) and (A1.11) can be stated as follows.

Under the assumptions that:

$$\text{i) } \exists_{\alpha^*>0} \ \forall_{\vec{v}^h\epsilon V^h_0} \ a(\vec{v}^h,\vec{v}^h) \geq \alpha^* ||\vec{v}^h||^2_V \qquad \text{(A1.16)}$$

$$\text{ii) } \exists_{\beta^*>0} \ \inf_{q^h\epsilon Q^h} \sup_{\vec{v}^h\epsilon V^h} \frac{b(\vec{v}^h,q^h)}{||\vec{v}^h||_V ||q^h||_Q} \geq \beta^* \qquad \text{(A1.17)}$$

problem (A1.13) has a unique solution $(\vec{u}^h,p^h)\epsilon V^h x Q^h$ and :

$$||\vec{u}^h-\vec{u}||_V + ||p^h-p||_Q \leq C_1\{ \inf_{\vec{v}^h\epsilon V^h} ||\vec{u}-\vec{v}^h||_V + \inf_{q^h\epsilon Q^h} ||p-q^h||_Q \} \qquad \text{(A1.18)}$$

(Girault and Raviart, 1979), in which $C_1>0$,and only depends upon $\alpha^*,\beta^*,||a||$ and $||b||$ and independent of h.

If the finite dimensional spaces V^h and Q^h are chosen such that :

$$\lim_{h\to 0} \inf_{\vec{v}^h\epsilon V^h} ||\vec{u}-\vec{v}^h||_V = 0 \qquad \text{(A1.19)}$$

$$\lim_{h\to 0} \inf_{q^h \in Q^h} ||p-q^h||_Q = 0 \qquad \text{(A1.20)}$$

the approximation converges to the exact solution i.e. :

$$\lim_{h\to 0} (||\vec{u}^h-\vec{u}||_V + ||p^h-p||_Q) = 0 \qquad \text{(A1.23)}$$

In conclusion it is stated that two important conditions must hold for the construction of finite dimensional approximations for the Navier-Stokes equations. In the first place, the approximation must be such that the V_0-coerciveness of $a(\vec{u},\vec{v})$ carries over to a V_0^h-coerciveness of $a(\vec{u}^h,\vec{v}^h)$, i.e. leads to a positive definite matrix. In the second place, the approximations of the velocity and pressure must be such that the discrete inf-sup condition (A1.17) holds i.e. V^h and Q^h can not be chosen arbitrarily. In general this inf sup condition is not always easy to check from (A1.17). Owing to the property that each $q\epsilon L_0^2(\Omega)$ can be associated with a $\vec{v}\epsilon H_0^1(\Omega)^D$ with :

$$\text{div } \vec{v} = q \qquad \text{in } \Omega$$

$$||\vec{v}||_{H^1(\Omega)^D} \leq c||q||_{L^2(\Omega)} \qquad \text{(A1.22)}$$

(see Girault and Raviart, 1979), it is possible to construct the following condition which implies the discrete inf-sup condition for the Stokes equations (Fortin, 1977) :

If there exists a linear continuous operator $\Pi_h : H_0^1(\Omega)^D \to V^h$ and a constant $c^*>0$ independent of h such that for all $\vec{v}\epsilon H_0^1(\Omega)^D$:

$$\int_\Omega q_h \text{div}(\vec{v}-\Pi_h\vec{v})d\Omega = 0 \qquad \forall q_h \epsilon Q^h \qquad \text{(A1.23a)}$$

$$||\Pi_h\vec{v}||_{H^1(\Omega)^D} \leq c^*||\vec{v}||_{H^1(\Omega)^D} \qquad \text{(A1.23b)}$$

Then the discrete inf-sup condition holds with $\beta^*>0$ independent of h. Using this condition, it can be proved (Cuvelier et al., 1986 and

Raviart, 1984) that the $(P_2^+-P_1)$ element used in this study, satisfies the Brezzi-Babuska condition.

The remarks made in the last paragraph of the preceding section, concerning the analysis of the non-linear Navier-Stokes equations, also apply here. For further details the reader is referred to the studies of Temam (1974) and Girault and Raviart (1979).

references.

- Brezzi F.,'On the existence, uniqueness and approximation of saddle point problems arising from Lagrangian multipliers.', RAIRO Anal. Numer., 8-R2, p 129-151 (1974).
- Cuvelier C., Segal A. and Van Steenhoven A.A.,'Finite element methods and Navier-Stokes equations.', D.Reidel Publishing comp. Dordrecht/Boston/Lancaster/Tokyo (1986).
- Fortin M.,'An analysis of the convergence of mixed finite element methods.', RAIRO Anal. Numer., 11, p 341-354 (1977).
- Girault V. and Raviart P.-A.,'Finite element approximation of the Navier-Stokes equations.', Springer-Verlag, Berlin,Heidelberg, New York (1979).
- Raviart P.-A.,'Mixed finite element methods'., In : The mathematical basis of finite element methods., Ed. Griffiths D.F.,Clarendon Press,Oxford (1984).
- Temam R.,'Navier-Stokes equations.', North-Holland,Amsterdam (1977).

APPENDIX 2: The penalty method for the (Navier-)Stokes Equations.

To obtain a simpler problem to solve, a penalty method to eliminate the pressure p can be used. Therefore the continuity equation is perturbed with a continuous bilinear form (p,q) multiplied by a penalty parameter ε which will tend to zero. The following problem will be considered :

Find a pair $(\vec{u}_\varepsilon, p_\varepsilon)$ in VxQ such that :

$$\begin{cases} a(\vec{u}_\varepsilon,\vec{v}) + b(\vec{u}_\varepsilon,p_\varepsilon) = \langle \vec{f},\vec{v}\rangle & \forall \vec{v}\in V \\ -\varepsilon(p_\varepsilon,q) + b(\vec{u}_\varepsilon,q) = \langle \gamma,q\rangle & \forall q\in Q \end{cases} \qquad (A2.1)$$

If the linear operator $B\in L(V,Q)$ is defined as :

$$(B\vec{v},q) = b(\vec{v},q) \qquad \forall v\in V\ ,\ \forall q\in Q \qquad (A2.2)$$

the variational problem (A2.1) then can be written as :

Find $\vec{u}_\varepsilon\in V$ and $p_\varepsilon\in Q$ such that :

$$a(\vec{u}_\varepsilon,\vec{v}) + \frac{1}{\varepsilon}(B\vec{u}_\varepsilon,B\vec{v}) = \langle \vec{f},\vec{v}\rangle + \frac{1}{\varepsilon}(\gamma,B\vec{v}) \qquad \forall \vec{v}\in V \qquad (A2.3)$$

$$p_\varepsilon = \frac{1}{\varepsilon}(B\vec{u}_\varepsilon-\gamma) \qquad (A2.4)$$

Under the assumptions that :

$$\exists_{\alpha>0}\ a(\vec{v},\vec{v}) + (B\vec{v},B\vec{v}) \geq \alpha||\vec{x}||_V^2 \qquad \forall \vec{v}\in V \qquad (A2.5)$$

and that the inf-sup condition (A1.11) holds, it can be proved (Bercovier, 1978) that (A2.3) has a unique solution and :

$$||\vec{u}_\varepsilon-\vec{u}||_V + ||p_\varepsilon-p||_Q \leq C\varepsilon \qquad (A2.6)$$

with C independent of ε.

Deriving the discrete variational form, the following approximate problem is obtained :

Find a pair $(\vec{u}_\varepsilon^h, p_\varepsilon^h) \in V^h \times Q^h$ such that :

$$a(\vec{u}_\varepsilon^h, \vec{v}^h) + b(\vec{v}^h, p_\varepsilon^h) = \langle \vec{f}, \vec{v}^h \rangle \qquad \forall \vec{v}^h \in V^h$$

$$-\varepsilon(p_\varepsilon^h, q^h) + b(\vec{u}_\varepsilon^h, q_h) = \langle \gamma, q_h \rangle \qquad \forall q^h \in Q^h \qquad \text{(A2.7)}$$

Since Q^h is a proper subspace of Q, the second equation of (A2.7) becomes :

$$p_\varepsilon^h = \frac{1}{\varepsilon} \varrho_h (B\vec{u}_\varepsilon^h - \gamma) \qquad \text{(A2.8)}$$

with ϱ_h the orthogonal projection operator from Q onto Q_h. Problem (A2.6) then can be written as :

Find $\vec{u}_\varepsilon^h \in V^h$ and $p_\varepsilon^h \in Q^h$ such that :

$$a(\vec{u}_\varepsilon^h, \vec{v}^h) + \frac{1}{\varepsilon}(\varrho_h B\vec{u}_\varepsilon^h, \varrho_h B\vec{v}_\varepsilon^h) = \langle \vec{f}, \vec{v}^h \rangle + \frac{1}{\varepsilon}(\varrho_h \gamma, \varrho_h B\vec{v}^h) \qquad \forall \vec{v}^h \in V^h$$

$$p_\varepsilon^h = \frac{1}{\varepsilon} \varrho_h (B\vec{u}_\varepsilon^h - \gamma) \qquad \text{(A2.9)}$$

In a similar way as in the continuous formulation it can be proved that under the assumptions that :

$$\exists_{\alpha^* > 0} \; a(\vec{v}^h, \vec{v}^h) + (\varrho_h B\vec{v}^h, \varrho_h B\vec{v}^h) \geq \alpha^* ||\vec{v}^h||_V^2 \qquad \forall \vec{v}^h \in V^h \qquad \text{(A2.10)}$$

and that the discrete inf-sup condition (1.17) holds, problem (A2.9) has a unique solution and :

$$||\vec{u}_\varepsilon^h - \vec{u}^h||_V + ||p_\varepsilon^h - p^h||_Q \leq C^* \varepsilon \qquad \text{(A2.11)}$$

Error bound (A2.11) does not hold if p_ε^h is written as :

$$p_\varepsilon^h = \frac{1}{\varepsilon}(B\vec{u}_\varepsilon^h - \gamma) \qquad \text{(A2.12)}$$

(i.e. a direct discretisation of (A2.2)), which is a wrong way of using the penalty formulation. However, in some cases equation (A2.12) can be used in combination with a suitable reduced integration technique for which the wrong penalty formulation is equivalent to the good one (Raviart, 1984, Bercovier, 1978). In fact then the numerical integration rule must be such that :

$$\frac{1}{\varepsilon}\int_T \varrho_h B\vec{u}^h_\varepsilon \bullet \varrho_h B\vec{v}^h_\varepsilon dT = \frac{1}{\varepsilon}\int_T B\vec{u}^h_\varepsilon \bullet B\vec{v}^h_\varepsilon dT \qquad \text{(A2.13)}$$

In literature $\varrho_h B$ is often referred to as B_h (Engelman et al., 1982, Fortin and Fortin, 1985).

Also for the, non-linear , Navier-Stokes equations error bounds as given in (A2.6) and (A2.11) can be given (Reddy, 1982, Carey and Krishnan, 1984). The element used in this study (see chapter 2) is based on the penalized formulation as given in (A2.9). The projection operator ϱ_h corresponds with the matrix M_p in equation (2.9).

references.

- Bercovier M.,'Perturbation of mixed variational problems. Application to mixed finite element methods.', RAIRO Anal. Numer., 12, p 211-236 (1978).
- Caray G.F. and Krishnan R.,'Penalty finite element method for the Navier-Stokes equations.', Comp. Meth. Appl. Mech. Eng., 47, p 183-224 (1984).
- Engelman M.S., Sani R.L., Gresho P.M. and Bercovier M.,'Consistent vs. reduced integration penalty methods for incompressible media using several old and new elements.', Int. J. Num. Meth. Fluids', 2, p 25-42 (1982).
- Fortin M. and Fortin A.,'Newer and newer elements for incompressible Flow.', In : Finite elements in fluids, Eds. Gallagher R.H., Caray G.F., Oden J.T. and Zienkiewicz O.C., John Wiley & Sons Ltd (1985).
- Raviart P.-A.,'Mixed finite element methods.', In : The mathematical basis of finite element methods., Ed. Griffiths D.F.,Clarendon Press,Oxford (1984).

- Reddy J.N.,'On penalty function methods in finite element analysis of flow problems.', Int. J. Num. Meth. Fluids., 2, p 151-171 (1982).

APPENDIX 3: Laser-Doppler experiments : material and methods.

As a supplement to the sections 3.2.3, 3.3.4, 4.3 and 5.3, in this appendix the measurement methods and experimental set-ups used in the two-dimensional (square step and bifurcation) and three-dimensional (bifurcation and curved tube) experiments will be described. Since for all these measurements quite similar methods are used, they are not described separately.

Laser-Doppler anemometry.

In the last two decades laser-Doppler anemometry has become an accurate method to measure fluid velocity without disturbing the flow. An extensive description of the physical aspects of this method and the different measurement configurations are given by Drain (1980). In the measurements described here, a forward scattering reference beam configuration (see Fig. A3.1) was used. This configuration is composed of a fixed source emitting laser light with a frequency ω_0. This light is scattered by moving particles with a velocity $\vec{u}$ inducing a Doppler shift $\omega_d=2k\sin(\gamma/2)u<<\omega_0$ (with k the wave number and $\gamma/2$ the angle between the main beam and the direction of the scattered light). Additionally, a second laser beam with frequency $\omega_0+\omega_s$ is used as a reference beam ($\omega_s<<\omega_0$). At the photo detector only the difference in frequency $\omega_s-\omega_d$ is detected. The

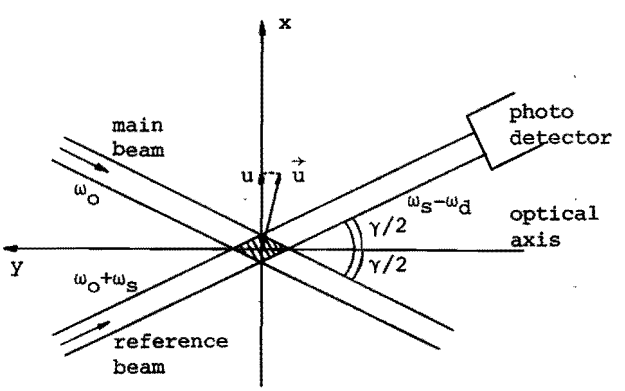

Fig. A3.1 : The reference beam forward scattering configuration in laser-Doppler anemometry.

photo detector output signal then has the following form :

$$V(t) = V_0 + \hat{V}\cos\{(\omega_s-\omega_d)t\},$$

from which the velocity component u can be derived as :

$$u = (\omega_s-\omega_d)\frac{\lambda}{2\sin(\gamma/2)}$$

with λ the wave length of the laser light.

Laser Doppler equipment.

Although a different (more advanced) laser-Doppler equipment was used for the three-dimensional experiments than for the two-dimensional ones, the essence of both equipments was the same. In Fig. A3.2 the configuration of laser-Doppler equipments as used in the experiments is shown schematically. A 5mW He-Ne laser was used producing a laser beam with a frequency $\omega_0 \approx 5\ 10^{14}$Hz. This beam was split by means of a beam splitter device which was different for the two equipments used. In the first equipment this beam splitter consisted of a rotating grating which induced a zeroth order beam, two first order beams and higher order beams. Optical lenses are used to converge the zeroth order beam and one of the first order beams in the measurement volume. Due to the rotating of the grating, the first order beams were shifted in frequency with about 820kHz. In the second equipment the beam was split by means of several prisms, whereas the frequency shift (40MHz) was induced by a Bragg cell.

The resulting measurement volume (an ellipsoid) had a length of about 0.5mm and a diameter of about 0.05mm for both equipments. The photo detector signal was fed to a frequency tracker converting the signal to a direct voltage proportional to the velocity component perpendicular to the optical axis. Using a 12-bit analog to digital converter and a microcomputer, taking on-line samples, finally the signal was fed into a minicomputer for further processing.

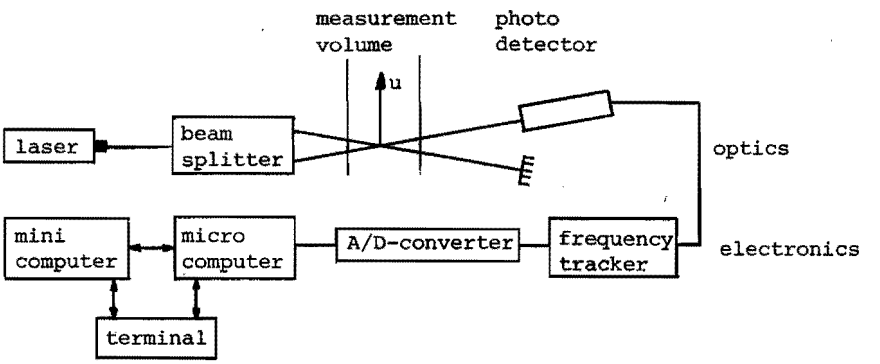

Fig. A3.2 : Laser-Doppler equipment as used in the experiments.

Fluid circuits.

In Fig. A3.3 the fluid circuit and measurement sections as used in the two-dimensional flow experiments are shown schematically. The fluid used was water in which some milk was dissolved to make possible appropriate scattering of the laser light. Before entering the flow channel, the water was passed through a buffer vessel (B) to break up any vortices present. A three- and a two-dimensional contractor (C3 and C2) at the end of the vessel ensured the velocity profile to be flat at the entrance of the flow channel. The length of the flow channel upstream of the measurement section was chosen such that the flow was fully developed before entering the measurement section. Downstream , the length was taken to be so large that no upstream influence of the outflow of the channel was expected. With a stop-cock SC1 the mean flow was adjusted. A pulsating volume-flow was created with regulator R and stop-cock SC2. The measurements were performed in the centerplane marked in the figures. By traversing the laser-Doppler equipment, mounted on a three-dimensional traversing system with an accuracy of about 0.01mm, the measurement volume was located at any desired location in the fluid.

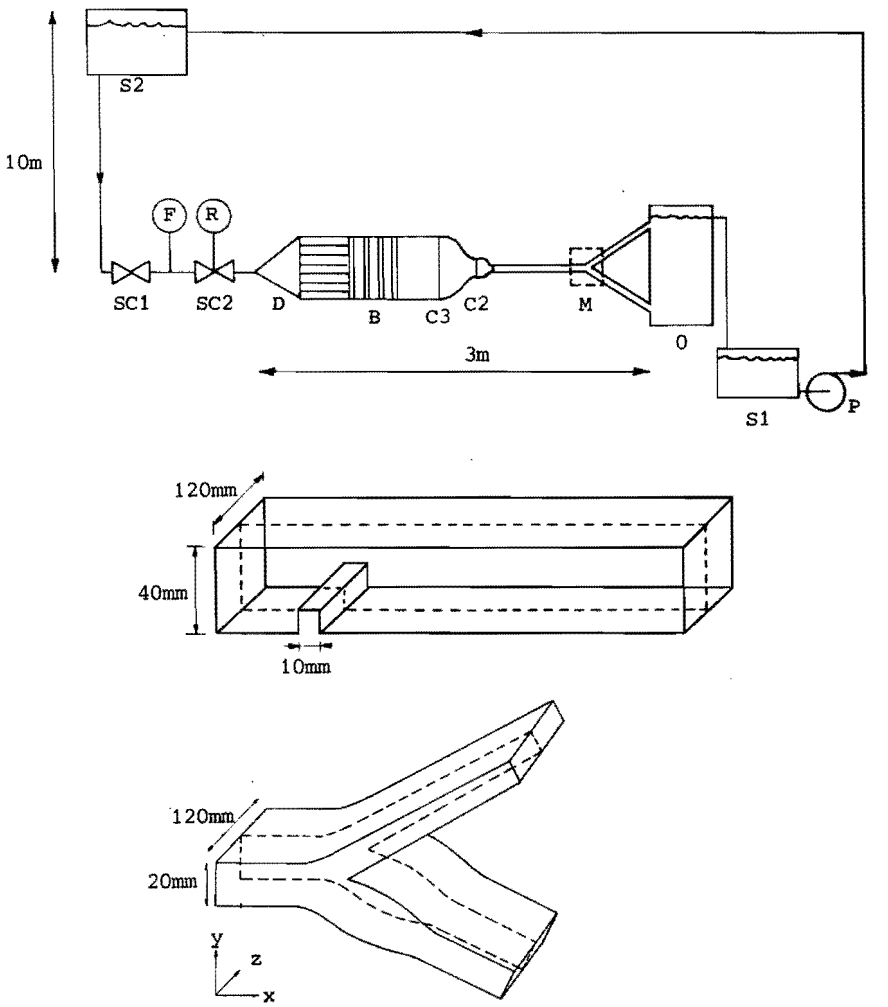

Fig. A3.3 : **Fluid circuit as used in the two-dimensional flow experiments together with the measurement section of the square step configuration and the two-dimensional bifurcation model.**

In Fig. A3.4 the fluid circuit and measurement sections as used in the three-dimensional flow experiments are given schematically. In the square step and bifurcation flow experiments water with a seeding of milk was used, whereas in the curved duct flow experiments a mixture of oil and kerosine was used as circulating fluid. The latter fluid makes possible exact matching of the index of refraction to

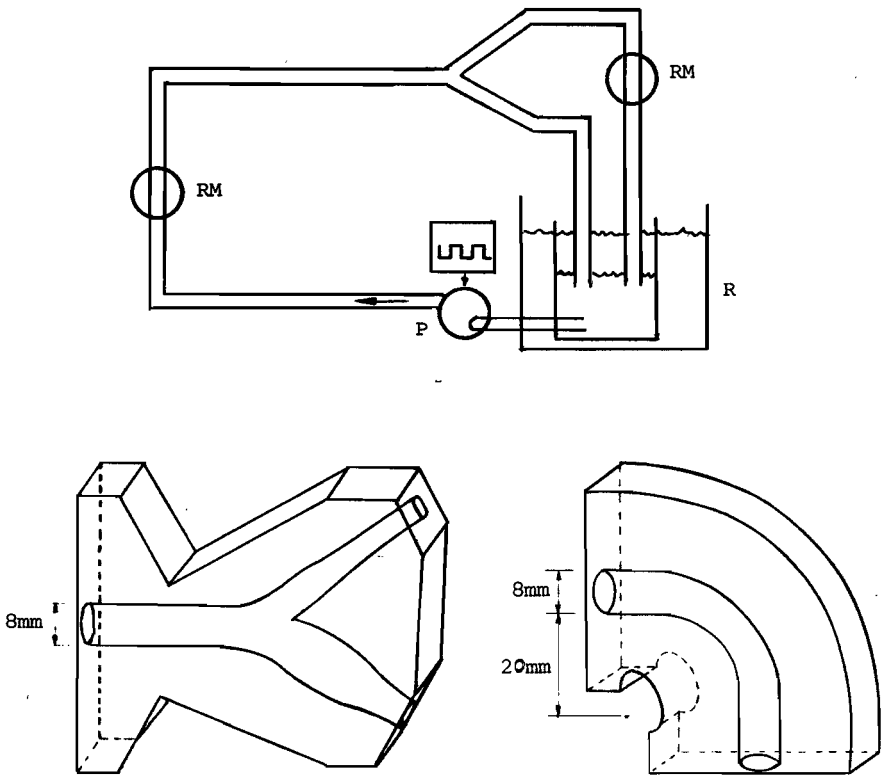

Fig. A3.4 : **Fluid circuit as used in the three-dimensional flow experiments together with the measurement sections of the three-dimensional bifurcation model and the curved tube.**

that of the perspex model. The oil mixture was seeded with silicagel. By means of a voltage controlled gear pump the fluid was pumped from the reservoir R into an inlet section consisting of a long circular pipe to ensure a fully developed flow at the entrance of the measurement section. With the aid of a three-dimensional stepper-motors device with an accuracy of about 0.03mm, the model was traversed in the desired position.

Data acquisition.

The data acquisition was controlled by a micro-computer. First a measurement cycle is initiated by a trigger pulse originated from

the terminal (steady flow measurements), the stop-cock (two-dimensional unsteady flow measurements) or the pump (three-dimensional unsteady flow measurements). Next, from the digitized signal, a number of samples were taken with timesteps equal to a multiple of 250μs and a maximum of 3000 per measurement cycle. When the intake from one measurement cycle was completed, the data were transported to the minicomputer and stored on disk. Hereafter, the micro-computer stands by for a new trigger pulse. In a post-processor program on the mini-computer averaging over the measurement cycles and calculation of the 95%-confidence intervals from a Student-t distribution were performed and the data were displayed in several formats.

References.

-Drain L.E.,'The laser-Doppler technique.', John Wiley & Sons (1980).

Samenvatting.

De numerieke analyse van bloedstroming in de halsslagader (vertakking) speelt naast in-vitro en in-vivo experimentele analyses een belangrijke rol in studies naar diagnostiek en onstaan van atherosclerose. Om meer inzicht te verkrijgen in deze stroming, is onderzoek vericht naar de numerieke analyse van Newtonse incompressibele stromingen in halsslagadermodellen met starre wanden.

Een Galerkin eindige elementen formulering van de instationaire Navier-Stokes vergelijkingen is geformuleerd en getest aan de hand van twee-dimensionale oscillerende stroming tussen twee vlakke platen en de von Karman wervelafschudding achter een cylinder. Vervolgens is de stationaire en instationaire stroming over een rechthoekige stap in een twee-dimensionaal kanaal geanalyseerd. Hierbij is speciale aandacht uitgegaan naar de optimalisering van de rekenprocedure. Tevens kunnen bovengenoemde berekeningen gezien worden als een eenvoudige twee-dimensionale modellering van een vernauwing in de halsslagader. De ontwikkeling en vorm van terugstroom gebieden achter de stap, die sterk tijdsafhankelijk blijken te zijn, worden hierbij gebruikt om de stroming te karakteriseren. Vervolgens is de stroming in twee-dimensionale vertakkingsmodellen voor zowel normale als vernauwde geometrieën geanaliseerd. Naast de distributie van de wandschuifspanning is ook hier speciale aandacht uitgegaan naar de analyse van de terugstroom gebieden. Zowel voor het (blokvormig) vernauwings model als voor het vertakkings model zijn de berekende snelheids verdelingen gevalideerd aan de hand van de resultaten van laser-Doppler snelheidsmetingen in analoge in-vitro modellen. Tot slot is een eerste stap naar volledige drie-dimensionale anlyse van de stroming in de halsslagader vertakking verricht. Hiertoe is de stationaire inlaatstroming in een bocht-vormige pijp geanalyseerd. De resultaten van de berekeningen van axiale maar ook secundaire snelheidsverdelingen zijn vergeleken met experimentele gegevens.

Uit de studie volgt dat de numerieke analyse een gedetailleerde en nauwkeurige beschrijving geeft van snelheids en wandschuifspannings verdelingen in vereenvoudigde modellen van de halsslagader vertakking. Voor complete drie-dimensionale analyses is verdere uitbreiding van computer capiciteit en vervolgonderzoek naar meer

efficienter numerieke oplosprocedures voor de Navier-Stokes vergelijkingen noodzakelijk.

Nawoord.

Het onderzoek zoals hier beschreven is uitgevoerd binnen het interafdelingsproject 'Atherosclerose' van de Technische Universiteit Eindhoven (TUE). Deelnemers van dit project zijn de vakgroepen Fundamentele Werktuigbouwkunde (WFW) van de faculteit Werktuigbouwkunde en Transportfysica (NT) van de faculteit Technische Natuurkunde, alsmede de capaciteits groep Fysiologie van de Rijkuniversiteit Limburg (RL) en de vakgroep Toegepaste Analyse van de faculteit Wiskunde en Informatica aan de Technische Universiteit in Delft (TUD). Het zal duidelijk zijn dat de steun van bovengenoemde onderzoeksgroepen van essentieel belang is geweest bij de totstandkoming van dit proefschrift. Met name denk ik hierbij aan de volgende personen.

Anton van Steenhoven (WFW) ben ik grote dank verschuldigd voor zijn stimulerende en deskundige begeleiding bij het onderzoek en de inhoudelijke suggesties bij het schrijven van het proefschrift.

Guus Segal (TUD) heeft, als auteur van het eindige elementen methode paket dat is gebruikt voor de numerieke analyse, het basismateriaal aangedragen dat nodig was voor de berekeningen en heeft bovendien een essentiele rol gespeeld bij de ontwikkeling en implementatie van de programmatuur die nodig was voor het uitvoeren van de tijdsafhankelijke berekeningen.

In het onderzoek staat de experimentele validatie van de numerieke berekeningen centraal. Het experimetele werk van Frank Vial, Camilo Rindt, Peter Bovendeerd , Joost Versteijlen en Huib de Heus uitgevoerd tijdens hun stage en/of afstudeer periode ligt hieraan ten grondslag. Bovendien is hierbij de technische ondersteuning van Theo van Duppen en Jacques Cauwenberg en het werk van Jos Corver van betekenis.

De assistentie van Jos Banens, Hans Leijsen en Cor van Rooij op respectivelijk soft- and hardware gebied hebben mij veel tijd bespaard en een vlotte voortgang van het ondezoek mogelijk gemaakt.

Roel van de Brink wil ik danken voor de verzorging van de figuren.

Dhr. J.L.M. Dietvorst dank ik voor de wijze waarop hij op de valreep de tekst heeft gecorrigeerd op het gebezigde engels.

Bovendien dank ik Claire voor haar steun, begrip en geduld op allerlei gebied en de tijd die ze mij gegund heeft.

Tot slot, maar niet in de laatste plaats, wil ik mijn ouders bedanken voor hun stimulerende maar ook relativerende opstelling die ik in alle voorafgaande jaren heb mogen ondervinden.

Levensbericht.

12- 2- 1958	Geboren te Maastricht
1970 - 1976	Atheneum-b gevolgd aan het Henric van Veldeke College te Maastricht.
1976 - 1982	Technische Natuurkunde gestudeerd aan de Technische Universiteit Eindhoven.
1983 - 1986	Wetenschappelijk assistent aan de Technische Universiteit Eindhoven afdeling der Werktuigbouwkunde (WFW).
1- 9- 1986	In dienst getreden als universitair docent aan de Technische Universiteit Eindhoven (WFW).

STELLINGEN

Behorende bij het proefschrift

NUMERICAL ANALYSIS OF CAROTID ARTERY FLOW

1. Bij een quantitatieve analyse van de stroming in de halsslagader vertakking is een drie-dimensionale modelvorming essentieel.

   Hoofdstuk 4 van dit proefschrift

2. De druk-correctie methode voor de discretisatie van de tijdsafhankelijke Navier-Stokes vergelijkingen zoals voorgesteld door Chorin (1968) is alleen efficient toepasbaar in eindige elementen formuleringen indien de massamatrix diagonaliseerbaar is binnen de orde van nauwkeurigheid.

   Chorin A.J.,'Numerical solution of the Navier-Stokes equations.', Math. Comp., 22, p 745-762 (1968).

3. Het gebruik van toroidale coordinaten systemen voor berekeningen van de inlaatstroming in een gebogen pijp (Soh en Berger, 1984) maakt het opleggen van fysisch correcte randvoorwaarden uiterst moeilijk.

   Soh W.Y. and Berger S.A.,'Laminar entrance flow in a curved pipe'., J. Fluid Mech., 148, p 109-135 (1984).
   Bovendeerd P.H.M., van Steenhoven A.A., van de Vosse F.N. and Vossers G.,'Steady entrance flow in a curved pipe.', J. Fluid Mech. ,in press (1987).

4. Toepassing van de 'karakteristieke' methode in combinatie met een eindige elementen formulering van de Navier-Stokes vergelijkingen (Pironneau, 1982) is niet toepasbaar bij problemen met Neumann randvoorwaarden.

   Pironneau O.,'On the transport-diffusion algorithm and its application to the Navier-Stokes equations.', Num. Math., 38, p 309-332 (1982).

5. De motivering van Brooks en Hughes (1982) om streamline-upwind/ Petrov-Galerkin formuleringen voor de discretisatie van de Navier-Stokes vergelijkingen te gebruiken, is gebaseerd op berekeningen met een te grove meshverdeling en hierdoor niet overtuigend.

   Brooks A.N. and Hughes T.J.R.,'Streamline upwind/Petrov-Galerkin formulations for convection dominated flows with particular emphasis on the incompressible Navier-Stokes equations.', Comp. Meth. Appl. Mech. Eng., 32, p 199-259 (1982).

6. Eliminatie van de snelheden en drukafgeleiden zoals voorgesteld voor het twee-dimensionale P_2^+-P_1 element (Griffiths, 1979) en tevens mogelijk voor het drie-dimensionale Q_2-P_1 element heeft voor het laatst genoemde element nauwelijks zin.

   Griffiths D.F.,'Finite elements for incompressible flow.', Math. Meth. Appl. Sci., 1, p 16-31 (1979).

7. Een kunstwerk is nooit abstract, kunst altijd.

8. De dwang waarmee vele promovendi stellingen moeten formuleren draagt niet bij tot hun methodologische ontwikkeling.

9. Het hoge geluidsvolume van de muziek in cafe's en discotheken is wellicht een belangrijke aanleiding tot het dragen van kledij met opschriften.

Eindhoven, januari 1987 Frans van de Vosse